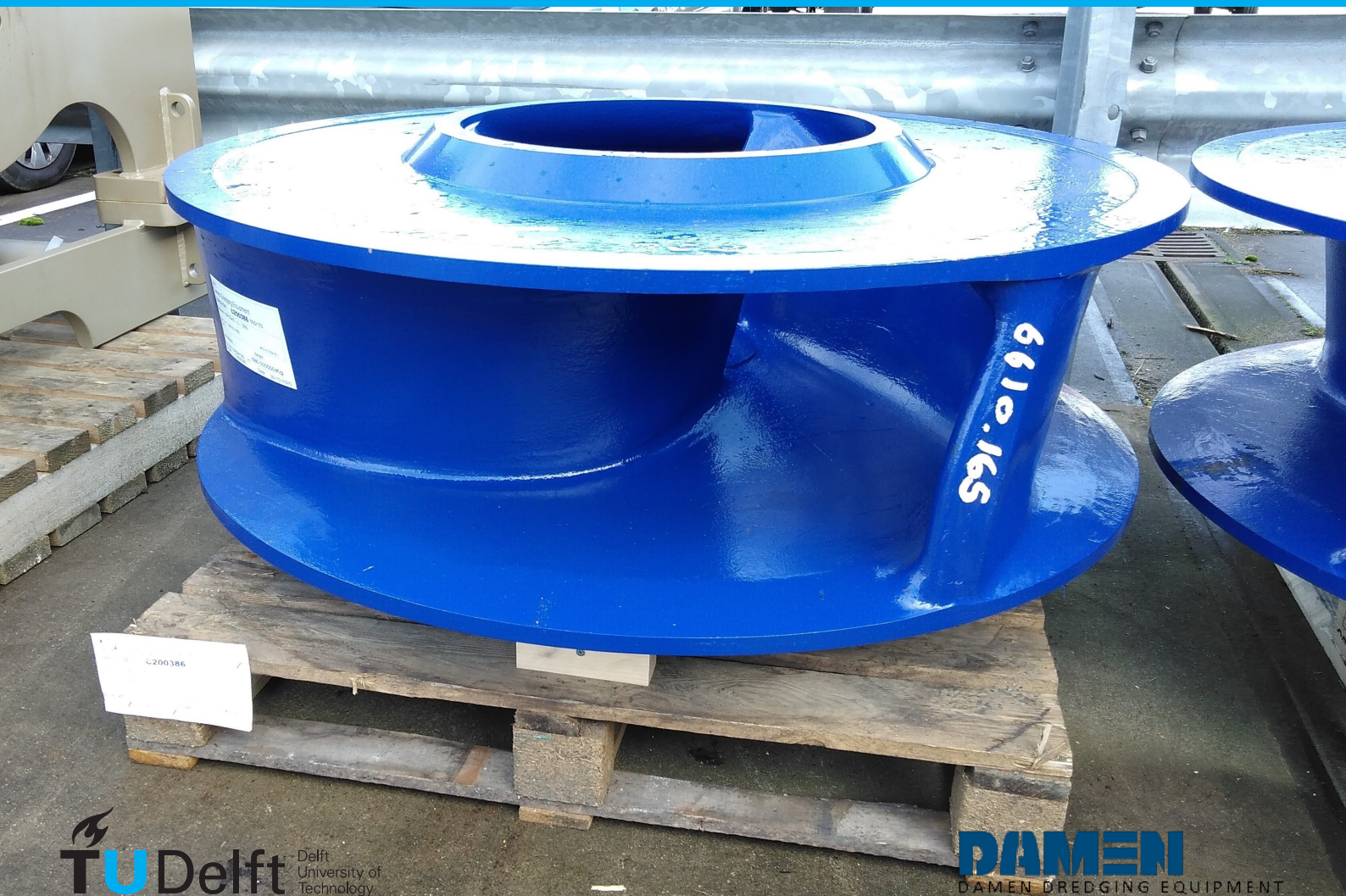


Erosion Estimation for the Impeller Blades of Centrifugal Dredge Pumps

W. Kleermaker

Master of Science Thesis
Aerodynamics
Faculty of Aerospace Engineering
Delft University of Technology

In collaboration with Damen Dredging Equipment



Erosion Estimation for the Impeller Blades of Centrifugal Dredge Pumps

by

W. Kleermaker

in partial fulfillment of the requirements for the degree of

Master of Science
in Aerospace Engineering

at the Delft University of Technology,
to be defended publicly on Tuesday August 31, 2021 at 14:00.

Student number: 4972678
Project duration: August 31, 2020 – August 31, 2021
Thesis committee: Dr. ir. A. H. van Zuijlen, TU Delft, supervisor
Prof. dr. ir. R. A. W. M. Henkes, TU Delft, supervisor
Dr. ir. M. I. Gerritsma, TU Delft
S. Sapkota MSc, Damen Dredging Equipment, supervisor

An electronic version of this thesis is available at <http://repository.tudelft.nl/>.

Acknowledgements

During the past twelve months, I had the privilege to work on this Master's Thesis project within the company Damen Dredging Equipment. I would like to thank Frank Bosman and Mark Winkelman for granting me the opportunity to work on the interesting topic of erosion modeling in centrifugal dredge pumps. Although we could not meet in person many times due to the measures that were taken for the Covid-19 pandemic, I enjoyed being part of the Research, Development & Innovation team. Our morning coffee sessions via Microsoft Teams were a good way to keep in touch with the members of the team.

I would like to thank my company supervisor Suman Sapkota, with whom I had numerous discussions and conversations. This really brought my work to a higher level. In addition, I received a lot of help and feedback from my university supervisors Ruud Henkes and Alexander van Zuijlen, for which I am very thankful.

The experimental part of this project proved to be a great challenge due to a number of mechanical problems. I would not have been able to finish the experiments without the help of the mechanics Jerry Wezendonk, Syb Mossink, Nando Bree and Arjan de Vries who were always willing to perform the needed repairs on the test circuit. In addition, I would like to thank Pieter van der Kooi for arranging all the required supplies and tools.

Finally, I want to thank my girlfriend Femmy and my parents for their never ending support during the years that I have been studying.

*W. Kleermaker
Veenendaal, August 2021*

Abstract

The constant impingement of sand particles on the wetted surfaces of a centrifugal dredge pump causes the performance of the pump to deteriorate. Therefore, components or complete pumps have to be replaced after some time. The use of numerical models to estimate the erosion wear in centrifugal dredge pumps can give insight into the principal erosion zones and the magnitude of the erosion in those zones. This information can be used to increase the erosion resistance of pump components. In addition, instructions for the maintenance of the pump can be composed based on the expected erosion wear. In that way, the efficiency of dredge processes can be increased considerably.

This Master's Thesis project is carried out by the author during a 12-month period at Damen Dredging Equipment in Nijkerk, The Netherlands. The focus of the project is on developing, validating and demonstrating a numerical model capable of estimating the erosion wear due to slurry flow on the impeller blades of a centrifugal dredge pump by using Computational Fluid Dynamics (CFD).

Within the CFD framework, it is found that the appropriate model for calculating the flow of the slurry (water with sand particles) is the Eulerian-Lagrangian method. The numerical computations are performed using the commercial software ANSYS Fluent. For the turbulence of the water, the $k-\omega$ SST turbulence model is used. The collisions of the particles with the wall are modeled using the Grant-Tabakoff model, whereas the linear soft sphere model is used for the inter-particle collisions.

Using the aforementioned combination of models several studies are conducted, starting with a validation study using a submerged impinging jet benchmark. From that study, it is found that the fluid and particle velocity fields can be calculated with reasonable accuracy. For the same type of problem, the numerical erosion profile is compared to experimental values. It appeared that there is a considerable dependency of the erosion profile on the material hardness. In addition, the result of the four-way coupled method is influenced to a large extent by the values of the collision model parameters. By comparing the resulting erosion profile from the two-way coupled model with the experimental erosion, a good qualitative agreement is found. However, the magnitude of the erosion is overpredicted by this model.

In addition, a verification and validation study was performed for the impeller. For the latter, new experiments were conducted in a facility that is available within the company Damen Dredging Equipment. By measuring a number of points before and after a 56 hour experiment, the resulting erosion could be determined. The four-way coupled computation for the impeller could not be fully completed within this project. However, the two-way coupled numerical model showed good correspondence with the experimental results.

The currently available model is capable of predicting the maximum erosion zones on the impeller blades. This information could for example be used to improve the design of the impeller or to get a first order estimation of the lifetime of an impeller. The applicability of the numerical model that is developed during the current project can be extended by for instance including the pump volute.

Contents

Abstract	v
List of Figures	ix
List of Tables	xiii
List of Symbols	xv
List of Abbreviations	xix
1 Introduction	1
2 Theoretical Background	3
2.1 Centrifugal dredge pumps	3
2.1.1 Flow through the pump	4
2.1.2 Pump performance	5
2.1.3 Specific speed	6
2.1.4 Influence of solid particles	7
2.2 Slurry flow	8
2.2.1 Flow parameters	8
2.2.2 Sand parameters	9
2.3 Erosion wear	10
2.3.1 Erosion wear mechanism	10
2.3.2 Parameters influencing erosion wear	12
2.3.3 Erosion wear in centrifugal pump impellers	12
2.4 Previous studies	13
2.4.1 Numerical	13
2.4.2 Experimental	14
2.4.3 Added value current project	14
3 Numerical Model	17
3.1 Computational Fluid Dynamics	17
3.1.1 Governing equations	17
3.1.2 Turbulence	18
3.1.3 Discretization	24
3.1.4 Solver	24
3.1.5 Verification and validation	24
3.1.6 Commercial CFD-codes	25
3.2 Slurry flow modeling	25
3.2.1 Force balance	26
3.2.2 Turbulent dispersion	28
3.2.3 Particle-fluid interaction	28
3.2.4 Particle-particle interaction	28
3.2.5 Particle-wall rebound	29
3.3 Erosion modeling	29
3.4 Conclusion	31
4 Experimental Setup	33
4.1 Facility	33
4.1.1 Installed sensors	34
4.1.2 Dredge pump	34

4.2	Experimental conditions	35
4.3	Duration of the experiment	37
4.4	Erosion measurement.	37
4.5	Post-processing	38
4.6	Results	40
5	Numerical Results	43
5.1	Benchmark study: Impinging jet	43
5.1.1	Flow field validation	44
5.1.2	Erosion validation	54
5.2	Verification impeller model	60
5.3	Validation impeller model	65
6	Conclusions and Recommendations	69
6.1	Conclusions.	69
6.2	Recommendations	70
	Bibliography	73
A	Governing Equations	77
B	Fluent Settings	79

List of Figures

1.1	Example of a severely eroded impeller	1
2.1	Cross-section of a typical centrifugal dredge pump (figure adapted from Vlasblom [2004])	3
2.2	Illustration of the slip phenomenon between the impeller blades of a centrifugal pump (figure adapted from Gülich [2020])	4
2.3	Recirculation in a centrifugal pump (Fraser [1981])	5
2.4	Pump characteristics (figure adapted from Gülich [2020])	6
2.5	Efficiency of different pump types as function of the specific speed (Çengel and Cimbala [2006])	7
2.6	Effect of the presence of sand particles on the performance of a centrifugal pump (Wilson et al. [2006]). It is assumed that both the mixture and the water have the same density to show the isolated effect of particle addition.	8
2.7	Sliding wear mechanisms (Stachiwak and Batchelor [2014])	11
2.8	Impact wear mechanisms (Stachiwak and Batchelor [2014])	11
2.9	Parameters that have an influence on erosion wear	12
2.10	Typical erosion patterns in centrifugal dredge pump impellers	12
3.1	Classification of CFD methods based on the way that turbulence is treated (Andersson et al. [2012])	19
3.2	Comparison of CFD methods for a fluctuating velocity signal (Andersson et al. [2012])	19
3.3	Reynolds decomposition for a statistically steady (left) and statistically unsteady (right) situation (Ferziger and Perić [2002]). The horizontal axes represent time whereas the velocity is displayed on the y-axis.	20
3.4	Non-dimensional velocity profile within a turbulent boundary layer (ANSYS, Inc. [2020a])	23
3.5	Effect of the particle diameter being greater than the first cell height in the mesh (Wang et al. [2021])	26
3.6	Impact angle dependence function for the Oka erosion model (Oka et al. [2005a]). This function is composed of a cutting term and a term that accounts for the repeated deformation. The combination of the two gives the actual function that is used in the Oka model (equation 3.43). In this figure, the function is named $g(\alpha)$, instead of $f(\alpha)$	30
3.7	Schematic overview of the numerical model that is used to calculate the erosion pattern due to solid particles impacting a target surface. The dashed part of the figure is only included for the two-way coupled and four-way coupled methods. In addition, the right-hand side represents the steps that are taken to compute the water flow field.	31
4.1	The "Testloop" facility that is available within the company Damen Dredging Equipment (figure adapted from Visscher [2012]). The for this project relevant components are mentioned in this figure.	33
4.2	3D-model of the BP2525MD centrifugal dredge pump	34
4.3	Cross-section of the BP2525MD centrifugal dredge pump impeller	35
4.4	Particle Size Distributions for the two different sand types that are used during the experiment. The d_{50} diameters for both types are shown in orange.	36
4.5	CRYSTA-Apex S121210 Coordinate Measurement Machine (Mitutoyo [n.d.])	38
4.6	Measured points before and after the experiment near the Trailing Edge of one of the impeller blades	38
4.7	Relation between the change in roughness profiles (quantified in terms of the arithmetical mean roughness, Ra) and the thickness loss. On the right-hand side, the definition of the curve length is explained.	39
4.8	Contour of the experimental thickness loss averaged over the three blades. The erosion at the grey parts of the blade is not measured.	40

5.1	Experimental setup for the submerged impinging jet as used in the study of Miska [2008]. The mixture flows (from left to right) out of the round nozzle, after which it impinges on the target wall.	44
5.2	Cross-section of the computational domain for the flow field benchmark	44
5.3	The grids used for validating the flow field, zoomed in at the nozzle exit region	46
5.4	Relative error (based on the pressure averaged over the target surface) for the flow field benchmark as a function of the typical cell size of the grid. The triangle indicates the slope of the curve, which is equal to the observed order of accuracy for the three finest grids.	46
5.5	Comparison of the numerical results, as computed using different grids, with the experimental fluid velocity field for different profiles (experiments from Miska [2008]). The locations of the velocity profiles are indicated with the red lines.	47
5.6	Fluid streamlines (grey) which exit the nozzle and impinge against the target surface. In this figure, the flow is from left to right. The black lines indicate the flow domain and the red lines represent the profiles at which the velocity is shown in the different figures in this section.	48
5.7	Comparison of the velocity profiles for different turbulence models (including the experiments from Miska [2008]). The locations of the velocity profiles are indicated with the red lines.	48
5.8	Comparison of the numerical results while using wall functions and resolving the boundary layer (including the results of the experiments by Miska [2008]). The locations of the velocity profiles are indicated with the red lines.	49
5.9	Wall shear stress as a function of the streamwise coordinate. The nozzle inlet is located at $x = 0 \text{ mm}$, whereas the nozzle outlet can be found at $x = 238 \text{ mm}$	50
5.10	Comparison of the numerical results for two different nozzle lengths (including the results of the experiments by Miska [2008]). The locations of the velocity profiles are indicated with the red lines.	50
5.11	Comparison of the two-way coupled numerical results, as computed using different grids, with the experimental particle velocity field for different profiles (experiments from Miska [2008]). The locations of the velocity profiles are indicated with the red lines.	51
5.12	Comparison of the numerical results for the different coupling methods (including the results of the experiments by Miska [2008]). The locations of the velocity profiles are indicated with the red lines.	52
5.13	Contour plot of the difference in water velocity magnitude with and without sand particles in the flow. For the former, the two-way coupled method is used. In this figure, the flow is from left to right.	53
5.14	Contour plot of the slip velocity, which is defined as the difference between the velocity of the mixture and the velocity of the particles. For the latter, the two-way coupled method is used. In this figure, the flow is from left to right.	53
5.15	Experimental setup for the submerged impinging jet as used in the study of Wang et al. [2021]. The mixture flows (from top to bottom) out of the round nozzle, after which it impinges on the target wall.	54
5.16	Relative error (based on the pressure averaged over the target surface) for the erosion benchmark as a function of the typical cell size of the grid. The triangle indicates the slope of the curve, which is equal to the observed order of accuracy for the three finest grids.	55
5.17	Comparison of the erosion profile, as computed using the two-way coupled method for different grids, with the experimental erosion profile at the target surface (experiments from Miska [2008]). The middle of the domain is located at $x/r_{nozzle} = 0$	56
5.18	Contour of the volume fraction around the nozzle exit, computed with the two-way coupled numerical method. In this figure, the flow is from top to bottom.	56
5.19	Comparison of the erosion results, as computed using the two-way coupled method for different values for the hardness (including the results of the experiments by Miska [2008]). The middle of the domain is located at $x/r_{nozzle} = 0$	57
5.20	Comparison of the erosion results using the different coupling methods (including the results of the experiments by Miska [2008]). The middle of the domain is located at $x/r_{nozzle} = 0$	58
5.21	Contour of the volume fraction around the nozzle exit for a one-way coupled (left) and a two-way coupled (right) computation. In this figure, the flow is from top to bottom.	58

5.22 Comparison of the erosion results, as computed using the two-way coupled method in combination with different erosion models (including the results of the experiments by Miska [2008]). The middle of the domain is located at $x/r_{nozzle} = 0$	59
5.23 Numerical domain for the impeller computations. In this figure, the pipe is shortened to ensure a good visibility.	60
5.24 Cross-section of the different grids that are used for the impeller grid convergence study	61
5.25 Relative error (based on the head) for the impeller computation as a function of the typical cell size of the grid. The triangle indicates the slope of the curve, which is equal to the observed order of accuracy.	62
5.26 Comparison of the pressure distribution along the impeller blade for the different grids	62
5.27 Comparison between the one-way coupled and two-way coupled erosion patterns on the Suction Side (a) and the Pressure Side (b) of the blade	63
5.28 Recirculation zone at the Pressure Side near the hub and the Leading Edge of the blade for the one-way coupled (left) and two-way coupled solvers (right). In these figures, the contours of the velocity magnitude are shown in combination with the streamlines of the flow.	64
5.29 Erosion profile along the blade for different erosion models (including the results of the experiment). On the right-hand side of the figure, the definition of the curve length s is shown.	64
5.30 Normalized erosion as function of the impingement angle	65
5.31 Erosion pattern on the Suction Side and the Trailing Edge of the blade for the two-way coupled numerical model (left) and the experiment (right)	66
5.32 Erosion pattern on the Pressure Side of the blade for the two-way coupled numerical model (left) and the experiment (right)	66

List of Tables

2.1	Classification of types of sand based on particle diameters (Matoušek [2004])	9
3.1	Different constants for the Oka erosion model (Oka et al. [2005a]; Oka et al. [2005b])	31
4.1	Best efficiency conditions for the BP2525MD centrifugal dredge pump	35
4.2	Experimental conditions averaged over the experimental time	36
4.3	Conditions used in the computations by Sellgren et al. [2005]	37
5.1	Grid parameters used in the grid convergence study for the flow field benchmark	45
5.2	Grid parameters used in the grid convergence study for the erosion benchmark	55
5.3	Physical parameters used for the impeller simulations	60
5.4	Grid parameters used in the grid convergence study for the impeller	61
B.1	Settings for solving the water flow field	80
B.2	Settings for solving the particle flow field (valid for all coupling methods)	80
B.3	Additional settings for solving the one-way coupled particle flow field	81
B.4	Additional settings for solving the two-way coupled particle flow field	81
B.5	Additional settings for solving the four-way coupled particle flow field	81

List of Symbols

Latin symbols

Symbol	Description	Unit
A, a	Cross-sectional area	$[m^2]$
A	Sieve aperture	$[m]$
$a, b, K, k_1,$ $k_2, k_3, n_1,$ $n_2, q_1, q_2,$ s_1, s_2	Empirical constants Oka erosion model	$[-]$
a_1	Constant $k-\omega$ SST turbulence model	$[-]$
B	Constant law of the wall	$[-]$
C_{drag}	Drag coefficient	$[-]$
C_{VM}	Virtual mass constant	$[-]$
C_{vs}	Spatial volumetric concentration	$[-]$
C_{vt}	Transport volumetric concentration	$[-]$
c	Absolute flow velocity	$[m/s]$
D_{parc}	Parcel diameter	$[m]$
d	Diameter	$[m]$
d^*	Reference diameter Oka erosion model	$[m]$
d_{50}	Mass-median particle diameter	$[m]$
d_{85}	Characteristic diameter particle distribution	$[m]$
d_a	Diameter of a circle with an area equal to that of the particle area	$[m]$
d_{mf}	Decisive particle diameter	$[m]$
d_{per}	Diameter of a circle with a perimeter equal to that of the particle	$[m]$
d_s	Diameter of a sphere with a surface area equal to that of the particle	$[m]$
d_v	Diameter of a sphere with a volume equal to that of the particle	$[m]$
E_v	Volume loss due to erosion	$[m^3]$
ER_v	Erosion ratio in terms of volume	$[m^3/kg]$
$ER_{v,90}$	Erosion ratio in terms of volume for normal impingement	$[m^3/kg]$
\hat{e}_{12}	Unit vector between the colliding particles	$[-]$
e_N	Normal restitution coefficient	$[-]$
e_T	Tangential restitution coefficient	$[-]$
F	Force	$[N]$
$F_{friction}$	Frictional collision force	$[N]$
F_{normal}	Normal collision force	$[N]$
Fr	Froude number	$[-]$
f	Specific body force	$[N/kg]$
g	Gravitational acceleration	$[m/s^2]$
H	Head available	$[m]$
H_R	Head required	$[m]$
Hv	Vickers hardness	$[N/m^2]$
H_{va}	Moh's hardness object	$[-]$
H_{vm}	Moh's hardness particles	$[-]$
i_m	Hydraulic gradient	$[m]$
K_0, K_1, K_2	Drag coefficient constant	$[-]$
K_s	Spring constant	$[N/m]$
K_T	Hardness ratio	$[-]$
k	Turbulent kinetic energy	$[m^2/s^2]$
k	Proportionality constant erosion models	$[-]$
L	Length scale	$[m]$

Symbol	Description	Unit
L, W	Particle dimensions	[m]
\mathcal{L}	Turbulent length scale	[m]
m	Mass	[kg]
\dot{m}_p	Particle mass flow rate	[kg/s]
N_{sp}	Specific speed, non-dimensional	[–]
n	Rotational rate	[1/s]
n	Empirical exponent erosion models	[–]
\hat{n}	Surface unit vector	[–]
n_s	Specific speed, dimensional	[$(m/s^2)^{3/4}$]
P	Input power	[W]
P	Particle perimeter	[m]
P_u	Useful power	[W]
p, p_{stat}	Static pressure	[N/m^2]
p_{exact}	Computed pressure without discretization error	[N/m^2]
p_{tot}	Total pressure	[N/m^2]
Q	Flow rate	[m^3/s]
R	Residual	[–]
Ra	Arithmetic mean roughness	[m]
Re	Reynolds number	[–]
Re_p	Particle Reynolds number	[–]
r	Position vector	[m]
S	Strain rate magnitude	[1/s]
S	Surface	[m^2]
St	Stokes number	[–]
s	Curve length	[m]
T	Averaging time	[s]
T_{shaft}	Torque applied to the pump shaft	[Nm]
t	Time	[s]
U	Velocity	[m/s]
\mathcal{U}	Turbulent velocity scale	[m/s]
U^*	Reference velocity Oka erosion model	[m/s]
U_{dl}	Deposit-limit velocity	[m/s]
U_{glide}	Gliding velocity (constant for the DEM-collision model)	[m/s]
U_{imp}	Impact velocity	[m/s]
U_{in}	Inlet velocity	[m/s]
U_{limit}	Limit velocity (constant for the DEM-collision model)	[m/s]
U_{min}	Minimum resistance velocity	[m/s]
U_N	Normal velocity	[m/s]
U_r	Relative tangential velocity magnitude	[m/s]
U_T	Tangential velocity	[m/s]
U_{tt}	Terminal settling velocity	[m/s]
u	Rotational velocity	[m/s]
u^+	Non-dimensional velocity	[–]
u_*, u_τ	Wall friction velocity	[m/s]
V	Volume	[m^3]
w	Relative velocity (with respect to the impeller blade)	[m/s]
x	Spatial coordinate	[m]
Y	Specific work	[m^2/s^2]
y	Wall distance	[m]
y	Thickness	[m]
y^+	Non-dimensional wall distance	[–]
z	Height	[m]

Greek symbols

Symbol	Description	Unit
α	Impingement angle	[rad], [°]
α_{limit}	Slope limit (constant for the DEM-collision model)	[-]
$\beta, \beta^*, \gamma, \sigma_k$	Constants k - ω SST turbulence model	[-]
$\sigma_\omega, \sigma_{\omega 2}$		
$\beta_1, \gamma_1, \sigma_{k1}$	Constants k - ω turbulence model	[-]
$\sigma_{\omega 1}$		
$\beta_2, \gamma_2, \sigma_{k2}$	Constants k - ε turbulence model	[-]
$\sigma_{\omega 2}$		
γ	Damping coefficient	[-]
Δ	Difference	[-]
Δx	Average cell edge length	[m]
δ	Particle overlap	[m]
δ_{ij}	Kronecker delta (1 if $i = j$, 0 if $i \neq j$)	[-]
ε	Turbulence dissipation rate	[m ² /s ³]
ε_D	Diameter fraction allowed to overlap	[-]
ε_{ijk}	Levi-Civita symbol (1 for an even permutation, -1 for an odd permutation, 0 for repeated indices)	[-]
ε_{rel}	Relative error	[-]
η	Efficiency	[-]
η_{coll}	Collision efficiency	[-]
κ	Von Karman constant	[-]
μ	Dynamic viscosity	[Ns/m ²]
μ_{coll}	Friction coefficient	[-]
μ_{glide}	Gliding friction coefficient (constant for the DEM-collision model)	[-]
μ_{limit}	High velocity limit friction coefficient (constant for the DEM-collision model)	[-]
μ_s	Static friction coefficient	[-]
μ_{stick}	Sticking friction coefficient (constant for the DEM-collision model)	[-]
μ_t	Turbulent dynamic viscosity	[Ns/m ²]
ν	Kinematic viscosity	[m ² /s]
ν_t	Turbulent kinematic viscosity	[m ² /s]
ξ	Lag, slip or transport factor	[-]
ρ	Density	[kg/m ³]
$\bar{\rho}$	Density ratio of the solid and liquid phases	[-]
τ	Stress	[N/m ²]
τ	Typical time scale	[s]
τ_{wall}	Wall shear stress	[N/m ²]
ϕ	General quantity	[-]
Ω	Angular velocity	[rad/s]
ω	Specific turbulence dissipation rate	[1/s]

Subscripts

Symbol	Description
0	Pump inlet
2	Impeller blade trailing edge
3	Discharge exit
f	Fluid
m	Mixture
p	Particle
w	Water

Superscripts

Symbol	Description
\rightarrow	Vector
\leftrightarrow	Second order tensor
$-$	Average
$/$	Fluctuations

List of Abbreviations

Abbreviation	Description
BBO	Basset, Boussinesq and Oseen
BEP	Best Efficiency Point
BP	Baggerpomp (dredge pump)
CFD	Computational Fluid Dynamics
CMM	Coordinate Measurement Machine
CV	Control Volume
DEM	Discrete Element Method
DGV	Dredge Gate Valve
DNS	Direct Numerical Simulation
DPM	Discrete Parcel Method
DRW	Discrete Random Walk
E/CRC	Erosion-Corrosion Research Center
ESP	Electrical Submersible Pump
FDM	Finite Differences Method
FEM	Finite Element Method
FVM	Finite Volume Method
LDV	Laser Doppler Velocimetry
LES	Large Eddy Simulation
MD	Medium Discharge
MSDM	Micro Scale Dynamic Model
PS	Pressure Side
PSD	Particle Size Distribution
RMS	Root Mean Square
RNG	Renormalization Group
RSM	Reynolds Stress Model
SPQ	Spike Parameter Quadratic-fit
SS	Suction Side
SST	Shear Stress Transport
(U)RANS	(Unsteady) Reynolds Averaged Navier-Stokes equations

Introduction

There are various methods to transport a mixture of sand and water (also known as a slurry), such as by using conveyor belts or transportation trucks. According to [Huang et al. \[2015\]](#), using a centrifugal pump is the most efficient and cost-effective procedure for this. Therefore, these pumps are widely used in dredging applications. The transportation of slurry flow may lead to certain mechanical problems such as erosion that comes from the contact of solid particles with the wetted surfaces of the pump (see figure 1.1). The damage that comes from this is also known as erosion wear and has a negative influence on the performance of the pump ([Huang et al. \[2019\]](#)). After some time, pump components or even the entire pump has to be replaced in order to continue the dredging operation.



Figure 1.1: Example of a severely eroded impeller

When the erosion rate of the pump components can be estimated in advance, i.e. during the design phase, the design of the components can be altered such that the pump is more resistant to erosion wear ([Krüger et al. \[2010\]](#)). This would allow the company Damen Dredging Equipment to reduce the maintenance costs of its centrifugal dredge pumps. Another advantage of a reliable estimation method is the possibility to setup maintenance plans which show in detail when certain components have to be replaced. This will help to increase the efficiency of the dredging process.

The main research objective of this Master's Thesis is to develop, validate and demonstrate a numerical model

capable of estimating the erosion wear due to slurry flow on the impeller blades of a centrifugal dredge pump by using Computational Fluid Dynamics (CFD). In order to achieve this research objective, three different research questions are considered:

1. What is the best way to model slurry flow using Computational Fluid Dynamics?
2. What is the best way to model erosion wear using Computational Fluid Dynamics?
3. How can the numerical model for erosion wear due to slurry flow on the impeller blades of a centrifugal dredge pump be verified and validated?

To start with, in *chapter 2*, the indispensable theoretical background for this project is treated. This comprises a discussion of the, for this project, most relevant and most important aspects of centrifugal dredge pumps. In addition, the flow of slurries and the phenomenon of erosion wear is included here. The chapter ends with an overview of the research that has been conducted on the subject of erosion wear in centrifugal dredge pumps.

Chapter 3 discusses the numerical model used in the project. Specifically, the general theory of CFD for single-phase as well as for multiphase flows is discussed. The modelling of erosion wear is also something that can be included in CFD, for which the modeling is explained in chapter 3.

Thereafter, in *chapter 4*, the setup of the experiment that is used for the validation of the numerical model is described, starting with the facility and experimental conditions that are used for this. This is followed by an explanation on how the duration of the experiment is determined. Then, the method that is used for measuring the erosion on the impeller blades is discussed. Finally, the post-processing procedure and the results are provided.

Chapter 5 is dedicated to the numerical results obtained in the project. This includes a benchmark validation study using a submerged impinging jet. Afterwards, the numerical model applied to the impeller is verified by studying several parameters and models. The chapter ends with a detailed validation of the numerical model for the impeller against the new experimental results.

In the final chapter of this report, *chapter 6*, the conclusions and recommendations of this project are listed and discussed.

2

Theoretical Background

Before setting up the numerical model, it is important to have a basic knowledge on certain theoretical aspects that play a role in the erosion wear of centrifugal dredge pump impellers. Therefore, this chapter discusses the theoretical background of the project. In the first section, different topics related to centrifugal dredge pumps are discussed. This is followed by a description of slurry flow. In the third section, the phenomenon of erosion wear is treated. This chapter ends with a discussion of the studies that have already been conducted on this topic.

2.1. Centrifugal dredge pumps

As mentioned before in the introduction, centrifugal pumps are widely used in the dredging industry, due to their efficient and cost-effective way of transporting slurries (Huang et al. [2015]). The main components of a centrifugal pump are the volute casing, the impeller, the bearing house and the pump shaft. For these components, there are many variations depending on the application. In figure 2.1, a typical cross section of the volute casing and the impeller of a centrifugal dredge pump is shown. The sections of the impeller that are not shown in this figure are the hub and shroud. These are the top and bottom plates which close off the impeller in the direction perpendicular to the cross-section that is shown in figure 2.1.

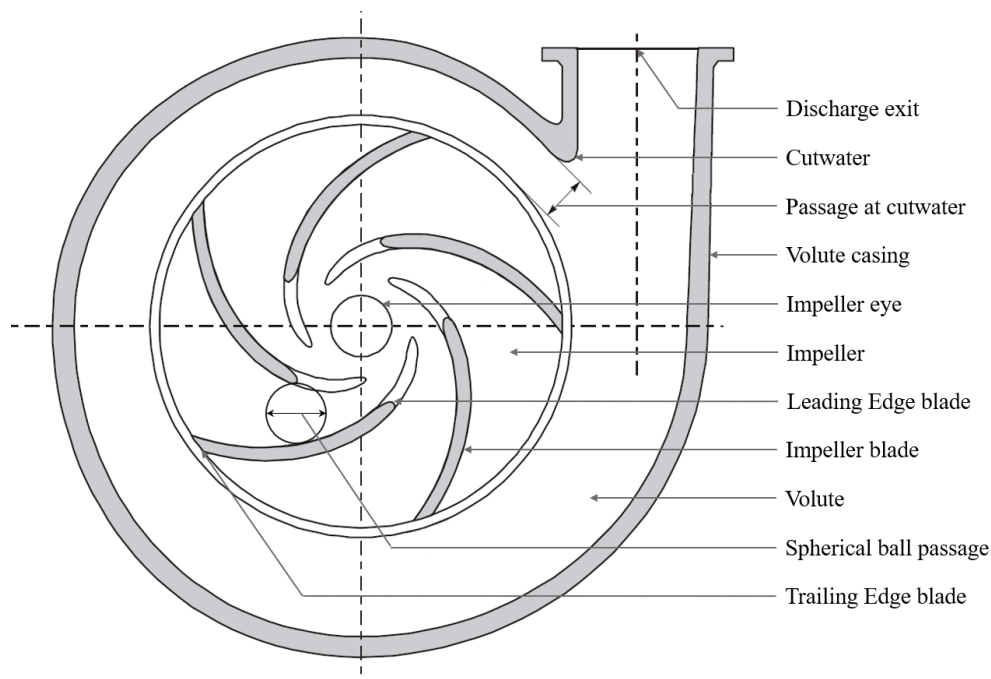


Figure 2.1: Cross-section of a typical centrifugal dredge pump (figure adapted from Vlasblom [2004])

The main function of the pump is to increase the total pressure of the flow by using the law of conservation of angular momentum. This is achieved by rotating the impeller (in anti-clockwise direction for the pump that is shown in figure 2.1). Due to this rotation, the pressure of the fluid in the volute is increased, having its maximum at the discharge exit (Gülich [2020]; Çengel and Cimbala [2006]).

In the following subsection, the flow pattern through the pump is explained. This is followed by an explanation of the pump performance parameters and the concept of specific speed. This section ends with a discussion on the influence of the presence of solid particles on certain aspects of centrifugal pumps.

2.1.1. Flow through the pump

The fluid enters the pump through the impeller eye. Çengel and Cimbala [2006] showed that, due to momentum exchange with the rotating impeller blades, the tangential and radial velocities of the fluid increase. An additional radial acceleration is caused by the centrifugal forces induced by the rotation. Therefore, the fluid exits the impeller while having gained both absolute velocity and static pressure. Then, the fluid enters the volute and is decelerated due to the geometry of the volute (Gülich [2020]). This deceleration causes the static pressure of the fluid to increase until it reaches its maximum at the discharge exit.

Within the impeller, the velocity can either be defined relative to the rotating impeller or in absolute terms. For the former, the letter w is usually used, whereas c is used for the latter velocity. The two velocity definitions can be related to each other in the following way:

$$\vec{c} = \vec{u} + \vec{w} = \vec{\Omega} \times \vec{r} + \vec{w} \quad (2.1)$$

Here, \vec{u} refers to the velocity that is due to the rotation of the impeller, $\vec{\Omega}$ is the angular velocity of the impeller and \vec{r} is the distance to the centre of the impeller.

In the two following paragraphs, two flow phenomena are discussed that can occur within the impeller, namely slip and recirculation. Both these phenomena are deviations from the ideal case where the flow exactly follows the curvature of the blades.

Slip

The deviation of the streamlines from the blades is known as slip and is caused by the non-uniform velocity distribution between the impeller blades (Gülich [2020]; Vlasblom [2004]). This is illustrated in figure 2.2.

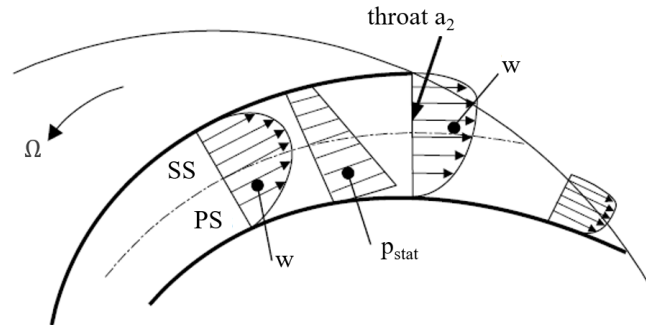


Figure 2.2: Illustration of the slip phenomenon between the impeller blades of a centrifugal pump (figure adapted from Gülich [2020])

Due to the shape of the impeller blades, the fluid at the concave side has a relatively low static pressure p_{stat} . Therefore, this side is named the Suction Side (SS). Similarly, the fluid on the convex side has a relatively high static pressure, which is the reason that this region is referred to as the Pressure Side (PS). This pressure distribution results in a velocity distribution relative to the impeller blade with a higher velocity near the Suction Side and a lower velocity near the Pressure Side. In addition, according to Gülich [2020], there is the Coriolis acceleration that forces the fluid to flow towards the pressure surface. Finally, in the region behind the throat (a_2 in figure 2.2), the flow curves towards the pressure surface to prevent a pressure discontinuity to occur behind the Trailing Edge of the blade. These three effects ensure that there is a nonzero angle between the flow and the impeller blade near the Trailing Edge (Gülich [2020]).

The effect of slip is that the total pressure difference between the pump inlet and outlet is reduced (Gülich [2020]; Vlasblom [2004]). Therefore, the pump becomes less efficient due to this phenomenon.

Recirculation

When the flow around an object encounters an adverse (positive) pressure gradient, the flow in the boundary layer decelerates. At some point, this loss of inertia becomes too large, causing the flow in the boundary layer to reverse direction or separate from the object (Çengel and Cimbala [2006]). Gülich [2020] stated that, in some cases, separation of the flow from the impeller blades leads to recirculation of the flow. This implies that, at a certain region, the fluid does not directly flow towards the volute. Instead, it returns to an upstream region and flows back again.

In the impeller of a centrifugal (slurry) pump, two different types of recirculation can occur (Fraser [1981]; Gülich [2020]). These types are illustrated in figure 2.3.

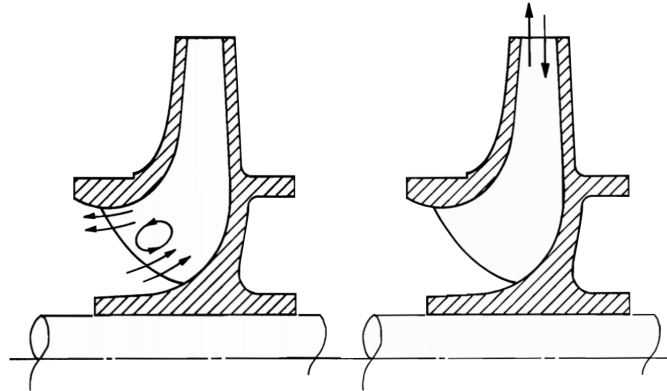


Figure 2.3: Recirculation in a centrifugal pump (Fraser [1981])

The first type occurs at the inlet of the impeller (Gülich [2020]). For this to happen, the flow has to separate locally from the Pressure Side of the blade. In addition there has to be a strong pressure gradient perpendicular to the flow direction. When these two requirements are met, a vortex is formed at the impeller inlet. This vortex forces the fluid near the impeller blade to flow back into the impeller eye, from where it re-enters the blade region. The second type of recirculation happens at the Trailing Edge of the impeller blades (Gülich [2020]). Here, the fluid first separates from the Suction Side of the blade. Due to this, the fluid flows back from the volute into the impeller, after which it flows back again into the volute. In addition to these two types, it might also be that flow separation and recirculation occur in the blade channel (Gülich [2020]).

Gülich [2020] explained that the amount of recirculation that occurs depends on the flow conditions. At the design conditions (the Best Efficiency Point, which is treated in section 2.1.2), no separation and therefore no recirculation occurs. However, when the flow rate is decreased, the flow starts to separate from the impeller blades, leading to recirculation. At these conditions, the pump is said to operate at partload. The recirculation regions become larger with decreasing flow rate, until full recirculation occurs at a flow rate equal to zero. For flow rates higher than the best efficiency flow rate, local separation regions may occur. However, Gülich [2020] noted that these do not lead to recirculation.

According to Gülich [2020], recirculation in a pump leads to an increase of the head (see section 2.1.2). However, the power consumption of the pump also increases. These effects are more pronounced for increasing specific speeds (see section 2.1.3). Besides the effects on the performance of the pump, recirculation may also damage the pump (Fraser [1981]; Gülich [2020]). The large eddies at the impeller outlet generate fluctuating pressures, which results in fluctuating loads on the pump components and an increase in noise level produced by the pump. In addition, the low pressure that occurs in the core of the vortices increases the chance that cavitation occurs. A final effect of recirculation is that it enhances the erosion wear.

2.1.2. Pump performance

According to Gülich [2020], the performance of centrifugal pumps can be described using the following quantities:

1. The flow rate Q
2. The head H
3. The efficiency η

Flow rate

The flow rate is defined as the useful volume flow through the discharge nozzle (Gülich [2020]). Usually, it is measured in $[m^3/s]$. For a discharge cross-sectional area A_3 and an outlet velocity c_3 , the flow rate can be calculated in the following way:

$$Q = c_3 A_3 \quad (2.2)$$

Head

The second important quantity for pump performance is the head H , which is defined in the following way (Gülich [2020]):

$$H = \frac{Y}{g} = \frac{\Delta p_{tot}}{\rho g} = \frac{p_3 - p_0}{\rho g} + (z_3 - z_0) + \frac{\|\vec{c}_3\|^2 - \|\vec{c}_0\|^2}{2g} \quad (2.3)$$

In this equation, Y is the specific work, which is the specific total useful energy that is transferred to the fluid. Furthermore, Δp_{tot} is the total pressure difference, g is the gravitational acceleration, p is the static pressure and z is the height. As can be seen, the head consists of a static pressure difference, a height difference and a velocity difference between the pump outlet (subscript 3) and the impeller inlet (subscript 0). Therefore, it is a measure for the total pressure that the pump adds to the fluid, scaled to the dimension $[m]$.

Efficiency

The efficiency of a centrifugal pump is defined as the ratio of the output or useful power and the input power (Wilson et al. [2006]). This results in the following equation for the efficiency:

$$\eta = \frac{P_u}{P} = \frac{\rho g H Q}{\Omega T_{shaft}} \quad (2.4)$$

Here, P_u is the useful power, whereas P is the input power and T_{shaft} is the torque applied to the impeller shaft. At a certain flow rate, the pump experiences its maximum efficiency. This condition is called the Best Efficiency Point, for which the abbreviation BEP is used (Gülich [2020]).

Pump characteristics

The performance of a specific pump is visualized using the pump characteristics (Gülich [2020]; Wilson et al. [2006]). Such a graph (or set of graphs) shows the head, the efficiency and the power of the pump for a certain rotational speed as a function of the flow rate. In addition, a curve is shown with the required head H_R , representing the head that is needed to overcome the resistance in a certain pipe system. The point where the required head crosses the head curve of the pump is called the working point. An example of such a characteristic is shown in figure 2.4.

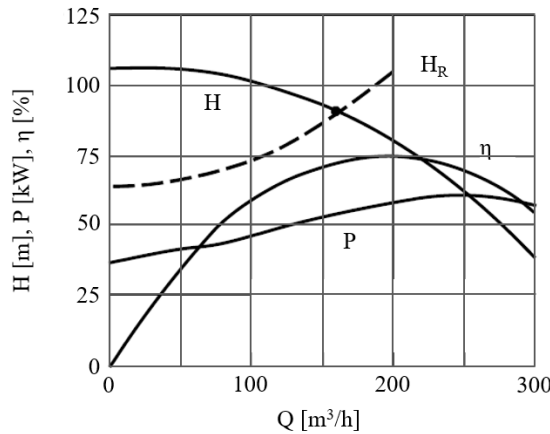


Figure 2.4: Pump characteristics (figure adapted from Gülich [2020])

2.1.3. Specific speed

A common parameter when talking about pumps is the specific speed N_{sp} . This parameter can be used to compare impellers that are geometrically not similar (Gülich [2020]). Therefore, according to Çengel and

Cimbala [2006], it is often used for the preliminary pump selection. Formally, the non-dimensional definition is given by (Vlasblom [2004]; Çengel and Cimbala [2006]):

$$N_{sp} = \frac{\Omega \sqrt{Q_{BEP}}}{(g H_{BEP})^{3/4}} \quad (2.5)$$

Here, the performance parameters are measured at the Best Efficiency Point for a certain angular velocity of the impeller. Figure 2.5 shows a clear overview of the pump types that perform the best for certain values of the specific speed. In this figure, the specific speed is displayed for different unit systems. The lower axis uses the non-dimensional specific speed of equation 2.5.

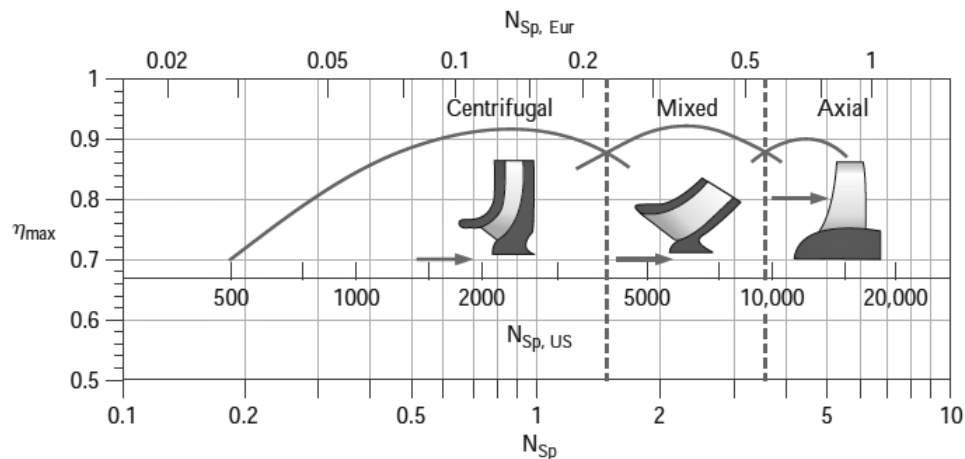


Figure 2.5: Efficiency of different pump types as function of the specific speed (Çengel and Cimbala [2006])

As can be seen, centrifugal pumps perform well for relatively low specific speeds. In engineering practice, often a dimensional version of the specific speed is used, indicated with n_s (Vlasblom [2004]; Wilson et al. [2006]):

$$n_s = \frac{n \sqrt{Q_{BEP}}}{H_{BEP}^{3/4}} \quad (2.6)$$

In this equation, the rotational rate n is used instead of the angular velocity. In addition, the gravitational acceleration is not included.

2.1.4. Influence of solid particles

The centrifugal pumps that are used in the dredging industry are different from those that are used to transport liquids. This is due to the presence of solid particles in the flow. In geometrical sense, the following differences can be identified (VBKO [1998a]; Vlasblom [2004]):

- The number of blades is smaller (usually 3-5). This accommodates a larger spherical ball passage, needed for the passage of (relatively large) solid particles.
- The cutwater passage and the eye of the impeller are relatively large. Therefore, the particles can flow through those regions more easily, which reduces the changes of blockage. The eye of the impeller can be accessed with less effort than the cutwater passage. Therefore, this component is made smaller than the cutwater passage to ensure that the largest particles get stuck there.
- The slurry pump consists of easily accessible and replaceable wear parts. In addition, the materials that are used in slurry pumps are more wear-resistant than the materials that are used for pumps that transport liquids. This is needed to account for the erosive nature of the slurry that flows through the pump.
- The volute is larger, which yields a larger deceleration of the flow in that region of the pump. This reduces the erosion wear in the pump casing. In addition, the wear in the pump casing is spread out more evenly.

Besides the geometrical differences, there are also changes in the performance when solid particles are added to the flow. VBKO [1998a] stated that the acceleration of the solid particles requires energy from the fluid. On the other hand, the energy of the particles results mostly in turbulence of the carrier fluid, which is eventually converted into heat. Therefore, provided that the density remains the same, the presence of solid particles reduces the head that can be achieved by the pump. The effect of the presence of sand particles on the performance of a centrifugal pump is shown in figure 2.6.

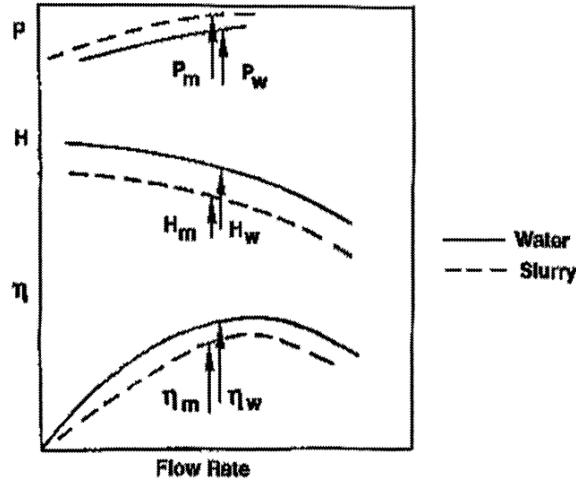


Figure 2.6: Effect of the presence of sand particles on the performance of a centrifugal pump (Wilson et al. [2006]). It is assumed that both the mixture and the water have the same density to show the isolated effect of particle addition.

As can be seen in this figure, the head drops due to the presence of the sand particles (as compared to water flow with the same density as the slurry). At the same time, the power requirement increases. Therefore, the overall efficiency is lower for slurry pumps than for normal pumps. These effects are more pronounced for larger particle sizes and larger concentrations (VBKO [1998a]). In addition to the presence of solid particles, the geometrical differences within the pump also reduce the efficiency of the pump (Sapkota [2018]; VBKO [1998a]).

2.2. Slurry flow

In dredging applications, the fluid is not homogeneous. In fact, it is a multiphase fluid, since it contains both a liquid (water) and a solid material (sand particles). Due to its nature, slurry flow behaves differently as compared to homogeneous flows (Wilson et al. [2006]). In this section, the different characteristic parameters that are of importance for modeling slurry flow are explained, starting with the flow parameters. This is followed by a discussion of the sand parameters.

2.2.1. Flow parameters

For liquid-solid flows, Oliemans [2001] identified four different dimensionless numbers that are of importance. The first of these is the Reynolds number, which is also a common parameter in single-phase fluid dynamics. This dimensionless number is defined as the ratio of the inertial and viscous forces:

$$Re = \frac{\rho UL}{\mu} \quad (2.7)$$

In this definition, U is a certain characteristic velocity (usually in pipe flow, the average velocity is used for this) and L is a certain characteristic length (for instance the pipe diameter in pipe flow). Furthermore, μ is the dynamic viscosity of the fluid. The Reynolds number is often used to differentiate between the laminar and turbulent flow regimes. The flow in a pipe becomes turbulent for Reynolds numbers above about 2300. The second parameter is the densimetric Froude number, which shows the relative importance of the inertial

and gravitational forces (Oliemans [2001]):

$$Fr = \frac{\rho_f U^2}{(\rho_p - \rho_f) g L} \quad (2.8)$$

The subscript f refers here to the fluid, whereas the subscript p is used for the solid particles. For Froude numbers that are much larger than 1, the inertial force is dominant over the gravitational force. This means that, in that case, the gravitational force can be neglected. On the other hand, for Froude numbers much smaller than 1, the gravitational force is larger than the inertial force.

In order to relate the behaviour of the solid particles to that of the fluid, the Stokes number is often used. According to Oliemans [2001] this number is the ratio of the particle relaxation time τ_p and a typical time scale of the flow τ_f . ANSYS, Inc. [2020a] showed that this results in the following definition for the Stokes number (where d_p is the particle diameter):

$$St = \frac{\tau_p}{\tau_f} = \frac{\rho_p d_p^2 U}{18\mu L} \quad (2.9)$$

When the Stokes number is much smaller than 1, the particles will adjust rapidly to changes in the fluid velocity field. On the other hand, for Stokes numbers much larger than 1, the particles are hardly affected by large velocity gradients in the flow.

Finally, there is the density ratio of the solid and liquid phases:

$$\tilde{\rho} = \frac{\rho_p}{\rho_f} \quad (2.10)$$

2.2.2. Sand parameters

Sand can be found in many different variants. For instance, there is a wide range of diameters for sand particles. Therefore, a division of soil types can be made based on this. This division is shown in table 2.1.

Table 2.1: Classification of types of sand based on particle diameters (Matoušek [2004])

Main type of soil		Particle size	
		Identification	size in [mm]
Boulders	Granular Non-cohesive	-	> 200
Cobbles		-	200 – 60
Gravel		Coarse	60 – 20
		Medium	20 – 6
		Fine	6 – 2
Sand		Coarse	2 – 0.6
		Medium	0.6 – 0.2
		Fine	0.2 – 0.06
Silt	Cohesive	Coarse	0.06 – 0.02
		Medium	0.02 – 0.006
		Fine	0.006 – 0.002
Clay		-	< 0.002

In practice, the particle diameter in a slurry flow is never constant. Therefore, a Particle Size Distribution (PSD) is used to describe the size of the particles (Matoušek [2004]); this gives the distribution of different particle diameters occurring in the slurry flow as a function of the accumulated mass fraction. Such a PSD can be characterized with three different parameters (Matoušek [2004]; VBKO [1998a]). The first is the mass-median diameter d_{50} . This is the diameter for which 50% of the particles (in terms of weight) is finer. The second characteristic diameter is referred to as d_{85} . This parameter gives the diameter for which 85% of the particles (in terms of weight) is finer. Finally, there is the decisive particle diameter d_{mf} , which is the average diameter as defined in equation 2.11. According to VBKO [1998a], this decisive particle diameter is used for the classification of the soil type according to table 2.1 .

$$d_{mf} = \frac{d_{10} + d_{20} + \dots + d_{80} + d_{90}}{9} \quad (2.11)$$

In this equation, the subscripts indicate the weight percentage of the particles that are finer. Besides the diameter of the particles, the particle concentration is important for the characteristics of the mixture. This concentration can be defined by considering the spatial volumetric concentration C_{vs} and the delivered or transport volumetric concentration C_{vt} (Miedema and Ramsdell [2019]; VBKO [1998a]):

$$\begin{aligned} C_{vs} &= \frac{V_p}{V_m} \\ C_{vt} &= \frac{Q_p}{Q_m} \end{aligned} \quad (2.12)$$

Here, the subscript m is used for the mixture. The spatial volumetric concentration is the concentration in terms of the volume V , whereas the transport volumetric concentration is the ratio of flow rates Q . Both concentrations can be related to each other through using the slip factor ξ , which is also known as the lag or transport factor (Miedema and Ramsdell [2019]; Wilson et al. [2006]). This factor is defined as the ratio of the slip velocity (the difference between the velocity of the mixture and the velocity of the solid particles) and the mixture velocity:

$$C_{vt} = (1 - \xi) C_{vs} = \left(1 - \frac{U_m - U_p}{U_m}\right) C_{vs} \quad (2.13)$$

In this equation U refers to the velocity. The volumetric concentration can be used to calculate the density of the mixture. Miedema and Ramsdell [2019] showed that this density is a combination of the densities of the fluid and the solid particles:

$$\rho_m = C_{vs}\rho_s + (1 - C_{vs})\rho_f \quad (2.14)$$

The final parameter used for slurry flows is the ratio of the particle size and a typical length scale of the flow (Oliemans [2001]):

$$\frac{d_p}{L} \quad (2.15)$$

2.3. Erosion wear

According to Wilson et al. [2006], an important limiting factor in the lifetime of a centrifugal dredge pump is erosion wear. Contact of the solid particles with the wetted surfaces of the pump induces the removal of material from those surfaces. After some time, components or even complete pumps have to be replaced in order to continue the dredging process. Bitter [1962] and Karelin et al. [2002] showed that erosion wear is a purely mechanical phenomenon. This is different from wear caused by water where also corrosive effects play a role.

In the first subsection, the underlying mechanisms of erosion are explained. This is followed by a list of the parameters that have an influence on erosion wear. Finally, in the last subsection, the phenomenon of erosion is applied to the specific case of centrifugal dredge pumps.

2.3.1. Erosion wear mechanism

In general, it can be said that there are two mechanisms for erosion wear due to solid particle impingement (Karelin et al. [2002]; Wilson et al. [2006]). The first is caused by particles that slide over a surface, which is therefore called sliding abrasion. The material removal happens in this case through small scale scratching of the surface. The second mechanism is caused by individual particles that impact the wearing surface at an angle with a certain velocity. This type is called impact erosion. Sometimes, these two types are also referred to as abrasive and erosive wear, respectively (Stachiowak and Batchelor [2014]).

Sliding wear

As indicated before, sliding wear is also known as abrasive wear. Stachiowak and Batchelor [2014] showed that there are four mechanisms for a sliding particle to remove material from the wear surface.

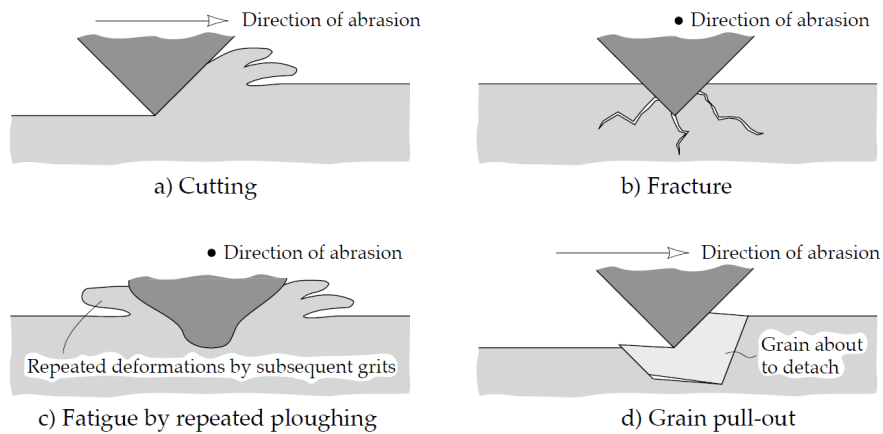


Figure 2.7: Sliding wear mechanisms (Stachiowak and Batchelor [2014])

Cutting wear typically occurs when sharp particles slide over a softer surface (Stachiowak and Batchelor [2014]). For brittle materials (e.g. ceramics), fracture is likely to occur (figure 2.7b). On the other hand, ductile materials often encounter repeated deformation when a rounded particle slides over it. This often leads to fatigue wear (figure 2.7c). Finally, grain pull-out occurs mainly in ceramics where the boundary between the different grains is relatively weak.

Impact wear

Contrary to sliding wear, impact wear is caused by particles impacting a surface. Depending on the speed of the particle, the angle of impact and the material of the surface, different failure mechanisms can occur (see figure 2.8).

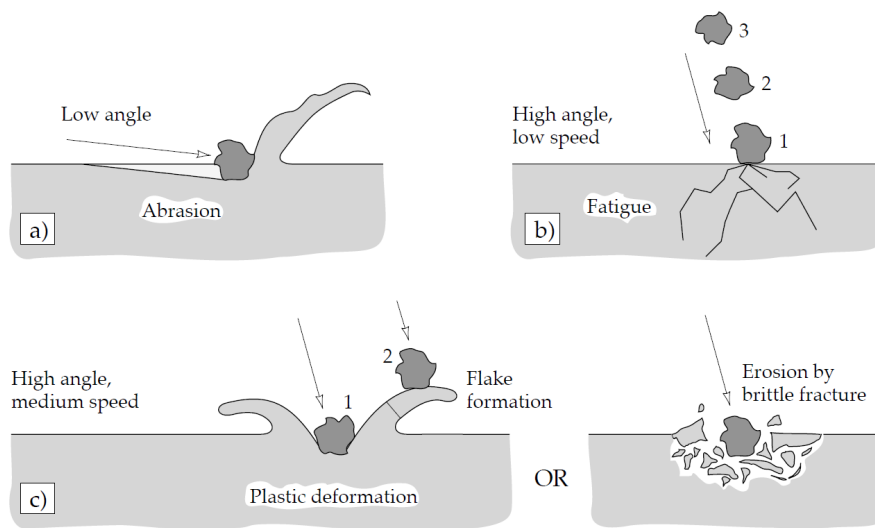


Figure 2.8: Impact wear mechanisms (Stachiowak and Batchelor [2014])

For an impingement angle close to 0° , there is almost no wear, since the particle does not impact the surface, nor does it exert a notable force on the surface (Stachiowak and Batchelor [2014]). When the impact angle is slightly larger than that, a wear pattern is formed that is similar to the cutting mechanism of sliding wear (figure 2.8a). This is no longer the case for high angles of impact. When the impact speed is low, the energy of the particles is not enough to deform the material plastically. However, due to repeated impacts, the surface fails due to fatigue (figure 2.8b).

For higher particle velocities, plastic deformation of the surface can be expected. When the material is ductile, flakes are formed around the impact point. According to Neopane [2010], repeated impacts cause these flakes

to detach from the wearing surface (left part of figure 2.8c). On the other hand, for brittle materials, erosion fracture takes place. Due to subsurface cracks, material is removed from the object that is hit (right part of figure 2.8c).

In addition to the wear mechanisms shown in figure 2.8, Bitter [1962] showed that there are particle impacts with high velocities where large heat effects play a role. Since these effect will not occur in the current study, these mechanisms are not discussed here.

2.3.2. Parameters influencing erosion wear

Erosion wear is a difficult phenomenon to understand. This is due to the fact that there are many factors that influence erosion wear. These parameters can be divided into three categories: flow parameters, particle parameters and surface parameters. In figure 2.9, (a selection of) these parameters is shown.

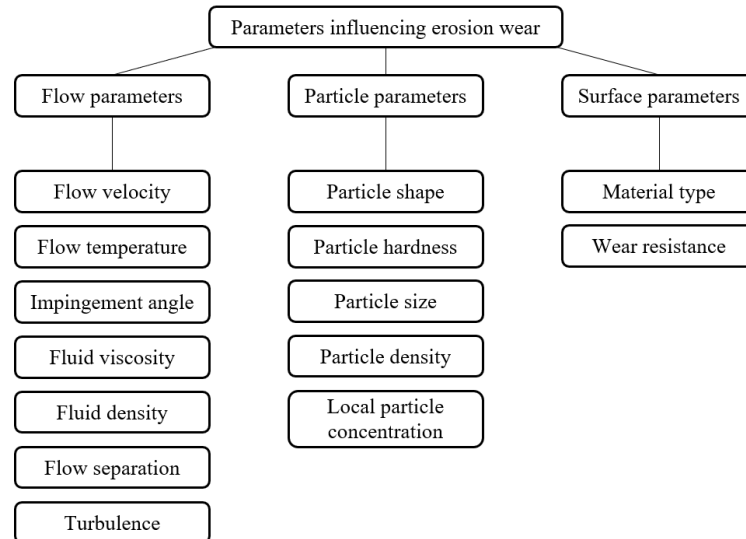


Figure 2.9: Parameters that have an influence on erosion wear

In the next chapter, it is explained how these influencing parameters can be taken into account in the numerical modeling of erosion wear.

2.3.3. Erosion wear in centrifugal pump impellers

There are two mechanisms responsible for the wear that comes from solid particles being in contact with a surface: sliding wear and impact wear (also referred to as abrasive wear and erosive wear). According to Pagalthivarthi and Gupta [2009] and Krüger et al. [2010], both these mechanisms occur in centrifugal dredge pumps.

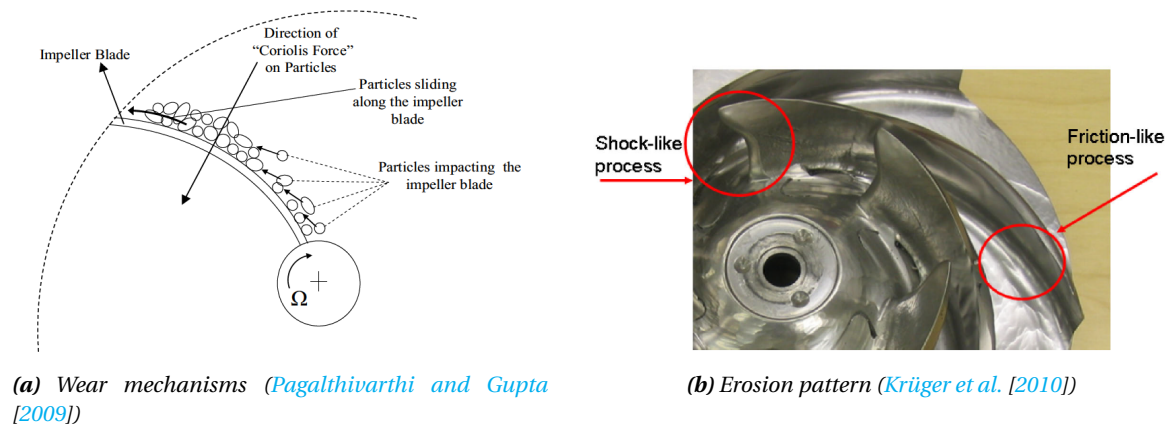


Figure 2.10: Typical erosion patterns in centrifugal dredge pump impellers

Near the Leading Edge of the impeller blade, impact erosion (shock-like process) occurs. When moving towards the Trailing Edge, sliding wear (friction-like process) becomes dominant due to the Coriolis effect (Palgathivarthi and Gupta [2009]). Increasing the rotational speed of the impeller also increases this effect. In that case, a larger portion of the impeller blade encounters sliding wear.

According to Gülich [2020], the highest erosion rate is observed at the leading edge of the impeller blades, in the corners between the blades and the hub and shroud and on the pressure surface of the blades near the Trailing Edge. Since operating at partload leads to an incidence angle at the Leading Edge of the blade and flow separation from the blade, this kind of operation increases the wear in the impeller.

2.4. Previous studies

In the past, there have already been a number of studies conducted on the topic of erosion in centrifugal dredge pump impellers. These studies can be divided into two categories, numerical (either with or without experimental validation) and purely experimental studies. The results of these studies are discussed in this section. From these results, the added value of the current project can be extracted.

2.4.1. Numerical

The early numerical models for predicting erosion wear in centrifugal slurry pumps were based on potential flow theory. The flow field obtained from this theory was used to calculate the particle velocities from a force or momentum balance.

Roco et al. [1985] and Roco and Addie [1987] included an iterative loop in their models, which ensured a two-way coupling between the solid particles and the fluid. In addition, they used an energetic approach which related the particle flow field to the erosion wear. Although the method was limited to two-dimensional pump casings and inviscid flows, it showed reasonable agreement with experimental results. A suggestion was done for the method to be used in the design of centrifugal pumps by for instance adopting a variable thickness in the casing based on the results for the erosion wear.

A different approach was suggested by Ahmad et al. [1986], who managed to setup a three-dimensional model which included all slurry pump components. In their study, it was assumed that the solid particles do not influence the flow field of the water (one-way coupling). In addition, a different erosion model was used which included the fact that the erosion wear is maximum when the particles leave the surface with zero tangential velocity. A validation study with experimental results showed that the model was able to estimate the location of maximum wear reasonably well. However, the actual level of erosion was underestimated. For low particle concentrations, they found that the maximum wear regions were located on the Pressure Side of the blade near the Leading Edge and on the back shroud in the impeller eye.

More recently, Computational Fluid Dynamics entered the scene. This opened the doors for more sophisticated methods. Using an unsteady Eulerian-Eulerian model (see chapter 3 for an explanation of slurry flow modeling), Krüger et al. [2010] found that the Leading Edge suffers from erosive wear, with the maximum erosion in the middle of the Leading Edge. This was found to be due to the high turbulent kinetic energy close hub and shroud plates, which pushes the particles to the centre. Along the blade, at the Trailing Edge and the side plate, abrasive wear dominates (as described in section 2.3.3). In order to predict these phenomena accurately, it was found to be important to accurately capture vortices and secondary flow structures in the impeller.

The occurrence of erosive wear at the Leading Edge and abrasive wear along the blade and near the Trailing Edge was confirmed by Sapkota [2018]. In addition, in this study, based on a one-way coupled Eulerian-Lagrangian method in combination with Finnie's erosion model, it was found that the maximum erosion occurs at the Leading Edge and on the Pressure Side near the Trailing Edge. When the flow rate is increased, the erosion on the blades also increases. Moreover, recirculation zones were found for the three flow cases that were investigated. These recirculation zones lead to an increased probability of particle impact. For further studies, Sapkota [2018] recommended to improve the model by using four-way coupled simulations.

In the study conducted by Lai et al. [2018], it was found that an increase in concentration increases the erosion rate, due to an increased particle impact frequency. On the other hand, it was shown that the particle diameter does not influence the particle trajectory and the impact frequency. These results came from computations with a transient two-way coupled Eulerian-Lagrangian model in combination with the E/CRC erosion model. The transient nature of this model enabled it to show that the erosion rate first rises until a constant value is reached after about 0.5 seconds.

Using a similar model except for the erosion model, [Huang et al. \[2019\]](#) confirmed the occurrence of the steady state erosion rate. However, they showed that the time after which it is reached depends on the flow rate through the pump: for lower flow rates, the steady state rate is reached later. For the total wear volume E_v , the following dependency on the flow rate was found:

$$E_v \propto Q^{1.0318} \quad (2.16)$$

According to [Huang et al. \[2019\]](#), the volute casing accounts for about 70% of the total wear in the centrifugal pump.

Although [Lai et al. \[2018\]](#) showed that the particle diameter does not influence the particle trajectories, [Tarodiya and Gandhi \[2019\]](#) (using a two-way coupled Eulerian-Lagrangian model) found that it does have an influence on the erosion wear. Since bigger particles have more kinetic energy, the erosion wear due to these particles is also higher. In addition, they found that increasing the concentration of the sand particles increases the wear. The third parameter they investigated was the pump speed. From the results of the study, they concluded that lowering this speed leads to a reduction in wear.

The change in geometry of the blade profiles due to wear was taken into account in the study conducted by [Xiao et al. \[2019\]](#), using a two-way coupled Eulerian-Lagrangian model. Qualitatively, the results of this model agreed with experiments, which were part of the study. By taking the geometrical changes into account, the unsteady behaviour of the problem could be studied. This showed that the impeller blade degrades first, which enhances recirculation. Due to a combination of this recirculation and increased clearances, the wear at the impeller outlet, the bottom of the impeller blade and at the volute casing decreases. Therefore, they concluded that small geometrical changes (for instance due to erosion wear) changes the later erosion patterns.

2.4.2. Experimental

In addition to numerical studies, also purely experimental studies have been conducted on the erosion of centrifugal dredge pumps. [Rayan and Shawky \[1989\]](#) performed an experimental study using two different concentrations, while measuring the mass loss. Here, they found a dependency of the erosive wear on the transport concentration. In addition, for medium and low concentrations, it was found that the weight loss rate due to erosion wear as a function of time shows similarities with the same curve for cavitation wear. This relation was monitored by measuring the mass of the impeller every hour or every five hours for the high and the low concentration, respectively.

Another study on the erosion of a centrifugal pump casing was conducted by [Gandhi et al. \[2001\]](#). Here, wear pieces were fixed at different locations to the casing of the pump. By measuring the weight loss of these pieces, the wear was monitored. Although it can be expected that the particles degrade over time, during the two hours of the experiment, the PSD did not change significantly. In addition, it was found that the wear is minimum for conditions near the BEP, suggesting that the life of the pump casing is maximum at these conditions.

[Khalid and Sapuan \[2007\]](#) studied the erosion wear on centrifugal pump impellers due to long-term operation. The total duration of the experiment was 480 hours with measurements every 24 hours. They showed that, from their measured quantities, the height loss of the outer end of the blade was the highest. The following linear relation between this parameter and time was found:

$$y = 1.506t - 5.077 \quad (2.17)$$

This equation was proposed to be used as an indication for the lifetime of the impeller based on a maximum allowable height loss of the blade ends.

2.4.3. Added value current project

As explained in the previous sections, a number of studies have already been conducted on the subject of erosion modeling for centrifugal slurry pumps. It was found that CFD can be used to compute the erosion pattern in a qualitative way ([Krüger et al. \[2010\]](#); [Tarodiya and Gandhi \[2017\]](#)), whereas the existing methods lack accuracy on a quantitative level. The exact setup of the numerical models used in the studies that are described before is not publicly available. This includes for instance details on the setup of the mesh and the values of certain parameters. Therefore, the purpose of the current project is to develop a numerical model that can be used by the company Damen Dredging Equipment. The starting point of this model is given

by the work of Sapkota [2018], who developed a steady one-way coupled Eulerian-Lagrangian method for predicting the erosion wear on centrifugal dredge pump impeller blades. The extension of the method to a four-way coupled model was recommended in this study to make it applicable to cases with higher volume fractions. A second recommendation was the validation of the numerical results with experimental data. Due to the large number of influencing parameters as well as the fact that the experimental studies on this subject lack information (e.g. the exact shape of the impeller), the experiment is included in the scope of the current project.

3

Numerical Model

The erosion occurring in centrifugal dredge pump impellers is modeled using the CFD package ANSYS Fluent version 2020 R2. In this chapter, the complete numerical model as implemented in Fluent is explained. This starts with an explanation of CFD for general purposes such as single-phase flows. After that, the theory is extended to include multiphase flows. The last subsection is dedicated to the modeling of erosion within CFD.

3.1. Computational Fluid Dynamics

Mathematically, fluid flow can be described using conservation laws. This leads to a system of coupled partial differential equations. Since it is not possible to solve these equations analytically, numerical methods are indispensable. In this section, the theoretical background of these numerical methods is discussed. First, the governing equations are shown, which is followed by a discussion of the topic of turbulence. Afterwards, the discretization of the equations and the solver used in this study are explained. This section is finished with an explanation of verification and validation of the results and a brief discussion on the commercial CFD-code that is used in the current study.

3.1.1. Governing equations

The specific conservation laws that are used for modeling fluids are the conservation of mass and momentum. For compressible fluids (when the density is dependent on the pressure), the conservation of energy also needs to be included. However, since liquids can be considered as almost incompressible (Kundu and Cohen [2008]; Versteeg and Malalasekera [2007]), this equation is not included in the current discussion. The equations that can be derived from the conservation principles are also known as the Navier-Stokes equations. The derivations of the equations, together with the structure of the energy equation can be found in sources such as Ferziger and Perić [2002] and Kundu and Cohen [2008].

Conservation of mass

The conservation of mass is based on the principle that mass can neither be created or destroyed. According to Çengel and Cimbala [2006], this premise is valid for all practical cases, except when nuclear reactions take place. When applying the principle to a fixed control volume V which is enclosed by a surface S , the integral form of this conservation law (also known as the continuity equation) can be obtained (Kundu and Cohen [2008]):

$$\frac{\partial}{\partial t} \iiint_V \rho dV + \iint_S \rho \vec{U} \cdot \vec{n} dS = 0 \quad (3.1)$$

The vector \vec{n} in this equation is the normal vector of the surface. Equation 3.1 can be converted to a differential form using Gauss' divergence theorem (Ferziger and Perić [2002]). This leads to the following partial differential equation:

$$\frac{\partial \rho}{\partial t} + \frac{\partial (\rho U_j)}{\partial x_j} = 0 \quad j = 1, 2, 3 \quad (3.2)$$

This equation uses the Einstein convention where a summation has to be performed when the same index appears twice in a certain term. For incompressible flows, which is the case in the current project, the continuity equation reduces to the condition that the velocity field is divergence-free:

$$\frac{\partial U_j}{\partial x_j} = 0 \quad j = 1, 2, 3 \quad (3.3)$$

Conservation of momentum

The second conservation law is that of momentum. This equation is based on Newton's second law, which states that a change in momentum of a certain object is balanced by the forces acting on it. Since the momentum is a vector quantity, this equation is a vector equation, essentially consisting of three different sub-equations. In integral form, the momentum equation is given by (Ferziger and Perić [2002]):

$$\frac{\partial}{\partial t} \iiint_V \rho \vec{U} dV + \iint_S \rho \vec{U} \vec{U} \cdot \vec{n} dS = \iint_S \vec{\tau} \cdot \vec{n} dS + \iiint_V \rho \vec{f} dV \quad (3.4)$$

In this equation, which is sometimes referred to as Cauchy's equation of motion, the right-hand side represents the sum of all (surface and body) forces acting on the control volume. These forces are described using the sum of the specific body forces \vec{f} and the stress tensor $\vec{\tau}$ which accounts for the surface forces. The left-hand side consists of the terms that describe the time rate of change and convection of momentum. Also this equation can be rewritten into a partial differential equation (Ferziger and Perić [2002]):

$$\frac{\partial(\rho U_i)}{\partial t} + \frac{\partial(\rho U_i U_j)}{\partial x_j} = \frac{\partial \tau_{ij}}{\partial x_j} + \rho f_i \quad i, j = 1, 2, 3 \quad (3.5)$$

For Newtonian fluids, the stress tensor τ_{ij} is linearly dependent on the rate of strain (Kundu and Cohen [2008]). In addition, the tensor can be split into an isotropic part, the pressure, and an anisotropic part, also known as the deviatoric stress tensor. For a general Newtonian fluid, the stress tensor is equal to:

$$\tau_{ij} = -\left(p + \frac{2}{3}\mu \frac{\partial U_k}{\partial x_k}\right) \delta_{ij} + \mu \left(\frac{\partial U_i}{\partial x_j} + \frac{\partial U_j}{\partial x_i}\right) \quad i, j, k = 1, 2, 3 \quad (3.6)$$

Here, δ_{ij} is the Kronecker delta which is zero unless the indices i and j are equal. In that case, this parameter is equal to 1. When the fluid can be considered incompressible, the momentum equation reduces to (Kundu and Cohen [2008]):

$$\rho \left(\frac{\partial U_i}{\partial t} + U_j \frac{\partial U_i}{\partial x_j}\right) = -\frac{\partial p}{\partial x_i} + \rho f_i + \mu \frac{\partial^2 U_i}{\partial x_j \partial x_j} \quad i, j = 1, 2, 3 \quad (3.7)$$

3.1.2. Turbulence

In general, a problem is said to be well-posed when a unique and stable solution exists (Nieuwstadt et al. [2016]). This latter condition means that a small disturbance in the initial or boundary conditions only leads to a small deviation of the solution. The Navier-Stokes equations only comply with these conditions for very special circumstances. Under these conditions, the flow is said to be laminar. However, in all other cases, the flow is unstable, meaning that the solution becomes unpredictable. This is also known as turbulent flow. The chaotic behaviour of this flow is associated with the nonlinear (convection) terms in the momentum equation. Besides chaotic, turbulent flows are also inherently unsteady, rotational, viscous and three-dimensional (Hickel [2019]).

In turbulent flows, rotational structures are present with a large range of time and length scales. These structures are called eddies (Versteeg and Malalasekera [2007]). Turbulence is produced at the larger scales. The energy of these scales is transferred to the smaller scales through the process of vortex stretching. This phenomenon is called the energy cascade. Eventually, the turbulent energy is dissipated and converted into thermal energy by the smallest eddies. The length and time scales of these small eddies depend on the Reynolds number: the smallest eddies become smaller with increasing Reynolds number.

As mentioned before, for practical applications, the Navier-Stokes equations can only be solved numerically. Based on the way how the turbulence is calculated, different numerical methods can be distinguished. These methods with their relative accuracy and relative computational costs are shown in figure 3.1.

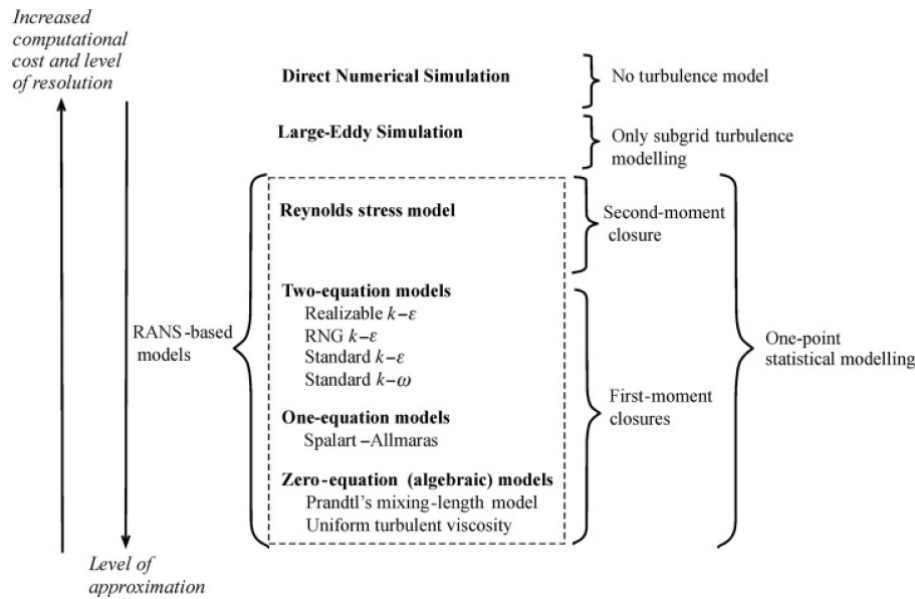


Figure 3.1: Classification of CFD methods based on the way that turbulence is treated (Andersson et al. [2012])

The most accurate CFD-method solves the equations for all length and time scales that occur in the flow. This method is called Direct Numerical Simulation (DNS) (Hickel [2019]). When this approach is adopted, no simplifying assumptions are used to solve the equations. This implies that the computational costs of the method are very high. Moreover, the simulation becomes computationally more expensive with increasing Reynolds number. Since engineering problems often involve large Reynolds numbers and complex geometries, DNS is in general not useful for these applications.

A second method that is common for solving fluid dynamical problems is called Large Eddy Simulation (LES). Nieuwstadt et al. [2016] showed that this method makes use of the observation that the small turbulent scales are isotropic and therefore relatively easy to model. The large scales on the other hand are dependent on the boundary conditions and the geometry (Hickel [2019]). By solving the large scales and modeling the small scales, the computational costs are reduced considerably as compared to the computational costs of DNS. However, this also implies that the method is less accurate than DNS.

In the third method, the entire turbulent spectrum is being modeled. This is done by making use of the Reynolds decomposition (equation 3.8). This decomposition separates the mean flow from the turbulent fluctuations. The equations for the mean flow are called the (Unsteady) Reynolds Averaged Navier-Stokes equations. Therefore, the method is named (U)RANS. Due to the complete modeling of turbulence, (U)RANS is the least accurate and computationally the cheapest of the three main methods. In engineering, highly detailed behaviour of the turbulent flow is often not needed. Therefore, (U)RANS is most often used for these applications (Andersson et al. [2012]). It is for the same reason that also for this study, the (U)RANS approach is adopted.

A clear overview of the resulting flow fields for the different methods is given in figure 3.2.

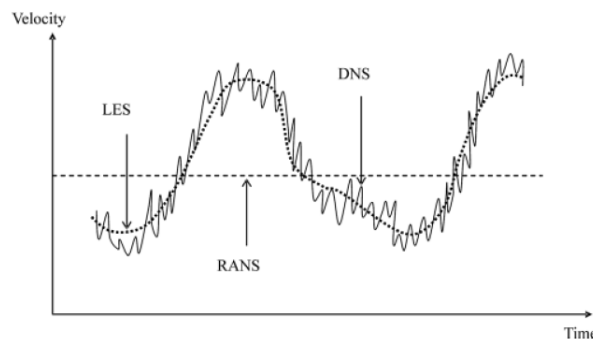


Figure 3.2: Comparison of CFD methods for a fluctuating velocity signal (Andersson et al. [2012])

As can be seen, DNS computes all velocity fluctuations, also those with the highest frequencies. In the signal obtained by LES, the higher frequencies are not resolved, while the lower frequencies are. Finally, (U)RANS does not show the turbulent fluctuations at all and only calculates the mean velocity.

Since the current study focuses on the use of (U)RANS for a practical problem, this method is explained in more depth in the following subsections, starting with the general equations for this method. Afterwards, the turbulence modeling involved in (U)RANS is explained. Finally, the treatment of flows in the vicinity of solid walls is discussed.

Reynolds equations

As mentioned before, (U)RANS solves the Reynolds Averaged Navier-Stokes equations. These can be obtained from equations 3.3 and 3.7 by using the Reynolds decomposition. This decomposition is defined in the following way (Hickel [2019]; Nieuwstadt et al. [2016]):

$$U_i = \bar{U}_i + U'_i \quad (3.8)$$

Here, U'_i is the fluctuating part of the velocity. In addition, \bar{U}_i is the ensemble average of the velocity signal. For statistically stationary processes, the ensemble average is equal to the time average over a period T (Nieuwstadt et al. [2016]):

$$\bar{U}_i = \lim_{K \rightarrow \infty} \frac{1}{K} \sum_{k=1}^K U_i^{(k)} = \lim_{T \rightarrow \infty} \frac{1}{T} \int_{-T/2}^{T/2} U_i(t + t^*) dt^* \quad (3.9)$$

The principle of the Reynolds decomposition for a statistically steady and unsteady case is illustrated in figure 3.3.

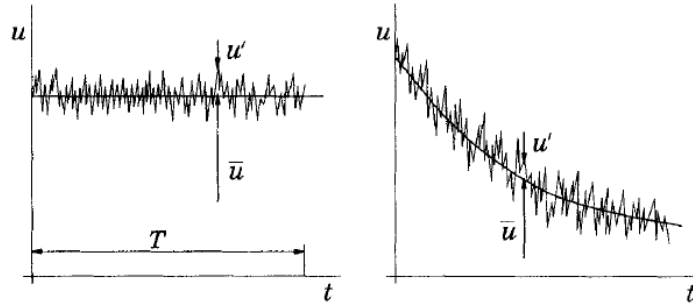


Figure 3.3: Reynolds decomposition for a statistically steady (left) and statistically unsteady (right) situation (Ferziger and Perić [2002]). The horizontal axes represent time whereas the velocity is displayed on the y-axis.

When the Reynolds decomposition is applied to the Navier-Stokes equations for an incompressible fluid, the resulting continuity and momentum equations are (Nieuwstadt et al. [2016]):

$$\begin{aligned} \frac{\partial \bar{U}_j}{\partial x_j} &= 0 \quad j = 1, 2, 3 \\ \rho \left[\frac{\partial \bar{U}_i}{\partial t} + \frac{\partial (\bar{U}_i \bar{U}_j)}{\partial x_j} \right] &= -\frac{\partial \bar{p}}{\partial x_i} + \rho \bar{f}_i + \mu \frac{\partial^2 \bar{U}_i}{\partial x_j \partial x_j} - \rho \frac{\partial \overline{U'_i U'_j}}{\partial x_j} \quad i, j = 1, 2, 3 \end{aligned} \quad (3.10)$$

It can be seen that there are more unknowns than equations, yielding a closure problem (Nieuwstadt et al. [2016]). This is due to the appearance of the Reynolds stress tensor $(-\rho \overline{U'_i U'_j})$. Therefore, additional equations are needed in order to be able to solve the system. These additional equations are obtained from a model for the Reynolds stress.

Turbulence models

Within (U)RANS, there are two groups of methods that are usually used for modeling the turbulence (Hickel [2019]). The first group consists of models that solve a transport equation for each of the independent terms

of the Reynolds stress tensor. These models are called Reynolds Stress Models (RSM) and increase the set of equations with six additional transport equations. This implies that the accuracy, but also the computational costs are increased considerably.

Therefore, for most practical applications, the second approach is used, which is based on the Boussinesq or eddy viscosity closure hypothesis (Nieuwstadt et al. [2016]). These are the methods that are named "First-moment closures" in figure 3.1.

Eddy viscosity models

The Boussinesq hypothesis makes use of the similarity between molecular and turbulent stresses. Since the molecular stresses are proportional to the molecular viscosity, an eddy viscosity is introduced as an equivalent quantity for the turbulence stresses. Nieuwstadt et al. [2016] showed that this leads to the following equation for the Reynolds stress:

$$-\rho \overline{U'_i U'_j} = \mu_t \left(\frac{\partial \overline{U}_i}{\partial x_j} + \frac{\partial \overline{U}_j}{\partial x_i} \right) - \frac{1}{3} \overline{U'_k U'_k} \rho \delta_{ij} \quad i, j, k = 1, 2, 3 \quad (3.11)$$

This hypothesis reduces the number of new unknowns due to the Reynolds stress from six to only one, the eddy or turbulent viscosity μ_t . The turbulent viscosity is a field quantity rather than a fluid quantity such as the molecular viscosity. From dimensional analysis, it follows that it is proportional to the density, a length scale \mathcal{L} and a velocity scale \mathcal{U} (Ferziger and Perić [2002]; Nieuwstadt et al. [2016]):

$$\mu_t \propto \rho \mathcal{U} \mathcal{L} \quad (3.12)$$

There are several ways to model the eddy viscosity. However, all of these methods assume that an eddy behaves in a similar fashion as molecules. In addition, isotropic turbulence and a local equilibrium between the stress and the strain are assumed (Andersson et al. [2012]). In the case that the shear flows are dominated by only one of the turbulent shear stresses, these assumptions are justified (ANSYS, Inc. [2020a]; Hickel [2019]). This is for instance the case for boundary layer flows, mixing layers and jets.

Eddy viscosity models are usually categorized based on the number of transport equations that they require, since this is a measure for the accuracy and the computational costs. Although also zero- and one-equation models have been developed, for general purpose simulations, often two-equation models are used (Andersson et al. [2012]). This is due to the fact that these models calculate the length and velocity scales, necessary for the eddy viscosity, directly from transport equations.

There are two models with two equations that form the basis for most of the other models in this category. The first of these is the k - ϵ model, which was introduced by Jones and Launder in 1972 (Hickel [2019]). This model uses transport equations to calculate the turbulent kinetic energy k and the turbulent dissipation ϵ . The second basic two-equation model is the k - ω model, by Wilcox in 1988 (Hickel [2019]). This model uses the specific turbulence dissipation rate ω , as well as the turbulent kinetic energy to calculate the eddy viscosity.

Comparison of turbulence models

In their study, Wang and Wang [2012] compared the different versions of the k - ϵ and k - ω turbulence models applied to a centrifugal pump. They found, after validating the results with an experiment, that the Renormalization Group (RNG) k - ϵ and the k - ω Shear Stress Transport (SST) models yield the highest accuracy. In addition, Ilker and Sorgun [2020] compared different turbulence models for the flow of slurry through a pipe. While comparing the numerical results with the results of an experiment, they found that most turbulence models (including the RNG k - ϵ and the k - ω SST models) showed accurate results.

Based on this discussion, and the fact that it is a commonly used model, it is decided to use the k - ω SST model in the current study.

k - ω SST turbulence model

Hickel [2019] explained that the k - ω model performs well for boundary layer flows and flows with pressure gradients and separation. However, this model is found to be very sensitive on inflow and freestream boundary conditions. On the other hand, the k - ϵ model gives good results for external aerodynamics, but does not perform well for flows with strong pressure gradients, streamline curvature or flow separation.

Therefore, Menter [1994] proposed a new turbulence model that combines the advantages of the k - ω and k - ϵ

turbulence models. The resulting k - ω SST model uses the following two transport equations for the turbulent kinetic energy and the specific turbulence dissipation rate:

$$\frac{D\rho k}{Dt} = -\rho \overline{U'_i U'_j} \frac{\partial u_i}{\partial x_j} - \beta^* \rho \omega k + \frac{\partial}{\partial x_j} \left\{ \left\{ \mu + \sigma_k \mu_t \right\} \frac{\partial k}{\partial x_j} \right\} \quad i, j = 1, 2, 3 \quad (3.13)$$

$$\frac{D\rho \omega}{Dt} = -\frac{\gamma}{\nu_t} \rho \overline{U'_i U'_j} \frac{\partial u_i}{\partial x_j} - \beta \rho \omega^2 + \frac{\partial}{\partial x_j} \left[\left(\mu + \sigma_\omega \mu_t \right) \frac{\partial \omega}{\partial x_j} \right] + 2(1 - F_1) \rho \sigma_{\omega 2} \frac{1}{\omega} \frac{\partial k}{\partial x_j} \frac{\partial \omega}{\partial x_j} \quad i, j = 1, 2, 3 \quad (3.14)$$

In these equations, the constants σ_k , γ , β and σ_ω are calculated from the constants of the standard k - ω and k - ϵ models, blended via equation 3.15. In addition, ν_t is the kinematic eddy viscosity which, just like its molecular counterpart, can be calculated by dividing the dynamic eddy viscosity by the density.

$$\phi = F_1 \phi_1 + (1 - F_1) \phi_2 \quad (3.15)$$

The blending function F_1 is constructed such that it is equal to 1 near the wall. On the other hand, this function goes to 0 while moving away from the wall. Therefore, essentially, the k - ω model is used for near wall flows, whereas the k - ϵ model is adopted in the freestream. Mathematically, this blending is achieved by using equation 3.16 for the blending function.

$$F_1 = \tanh \left\{ \min \left[\max \left(\frac{\sqrt{k}}{0.09\omega y}; \frac{500\nu}{y^2\omega} \right); \frac{4\rho\sigma_{\omega 2}k}{CD_{k\omega}y^2} \right] \right\} \quad (3.16)$$

Here, the term $CD_{k\omega}$ is equal to:

$$CD_{k\omega} = \max \left(2\rho\sigma_{\omega 2} \frac{1}{\omega} \frac{\partial k}{\partial x_j} \frac{\partial \omega}{\partial x_j}; 10^{-20} \right) \quad j = 1, 2, 3 \quad (3.17)$$

In addition to the blending between the k - ω and k - ϵ models, the k - ω SST model also takes into account the transport of the principal turbulent shear stress (hence the name Shear Stress Transport). This is done by defining the eddy viscosity in the following way:

$$\mu_t = \frac{\rho a_1 k}{\max(a_1 \omega; SF_2)} \quad (3.18)$$

In this equation, S is the magnitude of the strain rate. In addition, a second blending function is included which is equal to 1 near the wall, while it reduces to 0 for free shear layers:

$$F_2 = \tanh \left[\max \left(2 \frac{\sqrt{k}}{0.09\omega y} \right); \frac{500\nu}{y^2\omega} \right] \quad (3.19)$$

In the k - ω SST turbulence model, there is a large number of constants. These constants can be divided into constants that come from the k - ω model (set 1), constants from the k - ϵ model (set 2) and general constants (see equation 3.20). As mentioned before, the constants of sets 1 and 2 are used to calculate the constants of the k - ω SST model with the blending defined in equation 3.15.

Set 1:	$\sigma_{k1} = 0.85$	$\sigma_{\omega 1} = 0.5$	$\beta_1 = 0.075$	$\gamma_1 = 0.553$	(3.20)
Set 2:	$\sigma_{k2} = 1.0$	$\sigma_{\omega 2} = 0.856$	$\beta_2 = 0.0828$	$\gamma_2 = 0.44$	
General:		$a_1 = 0.31$	$\beta^* = 0.09$		

Near wall modeling

A special type of turbulent flow is that near a solid wall. In that case, a boundary layer is formed due to the no-slip condition at the wall itself (zero velocity at the wall). The flow near the wall is dominated by viscous forces. Therefore, the velocity gradient at the wall is related to the wall shear stress τ_{wall} in the following way (Andersson et al. [2012]):

$$\tau_{wall} = \mu \left. \frac{\partial \overline{U}_x}{\partial y} \right|_{y=0} \quad (3.21)$$

Here, the x-axis is aligned with the wall and the y-axis is taken normal to the wall. It is useful to describe the boundary layer flow in terms of non-dimensional parameters. For this transformation, the following characteristic wall friction velocity u_* (or u_τ) is used (Andersson et al. [2012]):

$$u_* = \sqrt{\frac{\tau_{wall}}{\rho}} \quad (3.22)$$

The velocity and distance from the wall can now be described using the non-dimensional parameters u^+ and y^+ , respectively (Nieuwstadt et al. [2016]).

$$u^+ = \frac{\bar{U}}{u_*} \quad y^+ = \frac{\rho u_* y}{\mu} \quad (3.23)$$

Here, y is the normal distance from the wall. These non-dimensional parameters can be used to define certain layers and sublayers in the boundary layer, as shown in figure 3.4.

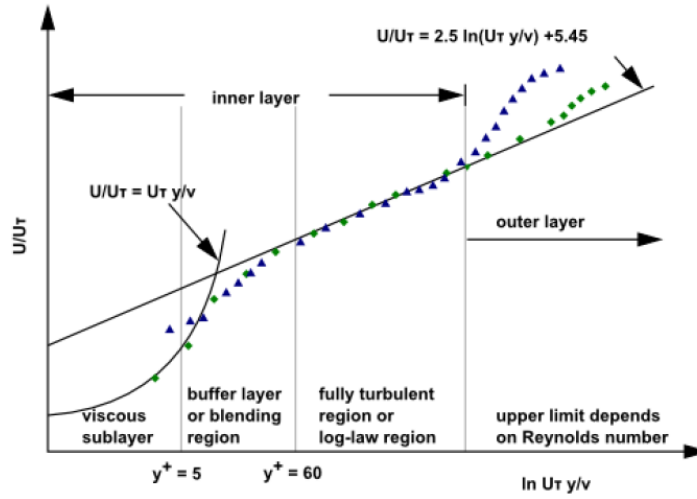


Figure 3.4: Non-dimensional velocity profile within a turbulent boundary layer (ANSYS, Inc. [2020a])

The sublayer that is closest to the wall is called the viscous sublayer. Here, Reynolds stresses are absent and, according to Andersson et al. [2012], the flow is almost laminar. The next layer is called the buffer layer, where the turbulent and viscous stresses are balanced. The part of the inner layer with the largest distance to the wall is called the log-law region. In this region, the viscous stresses are absent and the stresses in the flow are only due to turbulence. At the end of the inner layer, the outer layer starts. The exact y^+ value where this transition takes place is dependent on the Reynolds number: a higher Reynolds number increases the size of the log-law region in terms of y^+ units (ANSYS, Inc. [2020a]).

Essentially, for near-wall modeling of turbulent flows, there are two approaches (Andersson et al. [2012]; ANSYS, Inc. [2020a]). The first approach uses modified turbulence models to resolve the flow in the boundary layer. Due to the large gradients present in this region, this requires a fine mesh near the wall (so-called prism layers). More specifically, the first grid point as measured from the wall should be located around $y^+ \approx 1$ (ANSYS, Inc. [2020a]; Versteeg and Malalasekera [2007]).

The second approach uses wall functions as a bridge for the flow variables between the wall and the first cell (ANSYS, Inc. [2020a]). This approach requires the first grid point to be located within the log-law region. For this, ANSYS, Inc. [2020b] and Andersson et al. [2012] showed that the recommended y^+ -value for the first grid point is between 30 and 300. Within the log-law region, the dimensionless velocity can be described using the law of the wall (Andersson et al. [2012]; Ferziger and Perić [2002]):

$$u^+ = \frac{1}{\kappa} \ln(y^+) + B \quad (3.24)$$

In this equation, κ is the Von Karman constant (approximately equal to 0.4, Nieuwstadt et al. [2016]) and B is a constant that depends on the type of flow. In addition, wall functions are available for the turbulence

quantities. The applicability of wall functions can be extended to situations with pressure gradients by using non-equilibrium wall functions (ANSYS, Inc. [2020a]).

The advantage of wall functions is that the required grid is much coarser than when the boundary layer is resolved. However, this also yields larger inaccuracies, especially for flows with large pressure gradients that lead to separation (ANSYS, Inc. [2020a]). In addition, wall functions are not applicable in case of low Reynolds numbers, massive transpiration through the wall, strong body forces or highly three-dimensional boundary layers. In all of these cases, resolving the boundary layer using the modified turbulence models is preferred.

3.1.3. Discretization

In order to be solvable for a computer, the Reynolds Averaged Navier-Stokes equations (equation 3.10) have to be discretized. This process reduces the continuous equations to equations that are only defined at certain discrete points in space and time. For this, there are three methods that are commonly used (Ferziger and Perić [2002]): Finite Differences Method (FDM), Finite Volume Method (FVM) and Finite Element Method (FEM). From these methods, FVM is based on the principle of local conservation (Andersson et al. [2012]). Therefore, this technique is usually used for CFD.

In FVM, the computational domain is divided into small, non-overlapping Control Volumes (CVs) (Hickel [2019]). The grid that is formed with these cells can either be structured or unstructured. To each of the CVs, the integral conservation laws are applied. The integrals in these equations are approximated using quadrature rules (Hickel [2019]), such as the second-order mid-point rule. For a general quantity ϕ , this rule can be written as:

$$\iiint_V \phi dV \approx \bar{\phi}_c V \quad (3.25)$$

Here, $\bar{\phi}_c$ is the cell-averaged value of the quantity that is assigned to the cell centre. So, the solution is calculated in the centres of the cells. In order to find the solution at points somewhere between the cell centres, interpolation has to be used (Hickel [2019]). Both the quadrature rules and the interpolation introduce truncation errors. An increasing order of the method increases the reduction rate of the error as a function of the cell size. This means that, when a mesh is refined, the truncation error reduces with a larger amount for a higher order than for a lower order method.

3.1.4. Solver

There are different types of numerical methods that can be used for solving the equations that are mentioned before. In this study, the coupled pressure-based solver is used. ANSYS, Inc. [2020a] showed that in this method, a pressure correction equation is used to meet the constraint of mass conservation. In addition, this equation and the momentum equations are solved simultaneously to improve the rate of convergence for the computation. In section 3.4, a complete overview is shown of the steps that are taken in the solving process.

3.1.5. Verification and validation

When simulating a physical problem, it is important to assess the quality and accuracy of the results. For this, two steps have to be taken. The first step is to find the numerical error, which is done by means of verification (Hickel [2019]). Afterwards, the difference between the mathematical modeling and the physical system, the modeling errors, can be found using validation.

Verification

As mentioned before, verification quantifies the errors related to the numerical approximations. According to Hulshoff [2019], verification can be split into code verification and solution verification. The former is used to find out whether the code is consistent or not. More specifically, programming and conceptual errors are to be identified in this step.

Since iterative methods are used to solve the system of equations, the first part of solution verification focuses on the iterative errors. A commonly used measure for this error is the residual (Hickel [2019]). This residual is defined as the difference between the computed solution and the exact solution. When considering the simple algebraic system $\vec{A}\vec{\varphi}^n - \vec{b} = 0$, the residual for the n^{th} iteration \vec{R}^n would be defined in the following way (Hickel [2019]):

$$\vec{R}^n = \vec{A}\vec{\varphi}^n - \vec{b} \quad (3.26)$$

Since the conservation equations are calculated for all cells in the mesh, the Root Mean Square (RMS) value of the residual is often displayed as a function of the completed number of iterations.

The second part of solution verification is about the round-off error of the computer. This error is due to the fact that a computer always uses a finite number of significant digits for a real number. This is also known as the machine accuracy (Versteeg and Malalasekera [2007]).

Finally, there is the discretization error, which is due to the discretization of the domain and the equations. This error can be quantified by using a scalar quantity ϕ as computed from at least three different grids. Provided that the discretization error is small enough, the following equation can be used for this error (Hulshoff [2019]):

$$\varepsilon_i = \phi_i - \phi_{exact} = a (\Delta x_i)^{p_o} \quad (3.27)$$

Here, ϕ_{exact} is the solution without discretization error, Δx is the average cell edge length within the grid and p_o is the observed order of accuracy of the model. This equation is a good approximation when the observed order of accuracy p_o is close to the actual order of accuracy p of the method. In that case, the solution is said to be in the asymptotic range, implying that the leading order error term is dominant. This can be validated by calculating p_o from the following (implicit) equation (Celik et al. [2008]):

$$p_o = \frac{1}{\ln(\Delta x_2/\Delta x_1)} \left| \ln \left| \frac{\phi_3 - \phi_2}{\phi_2 - \phi_1} \right| + \ln \left(\frac{(\Delta x_2/\Delta x_1)^{p_o} - 1}{(\Delta x_3/\Delta x_2)^{p_o} - 1} \right) \right| \quad (3.28)$$

The solution without discretization error can then be extrapolated from the results of the three different grids by using the following equation (Celik et al. [2008]):

$$\phi_{exact} = \frac{(\Delta x_2/\Delta x_1)^{p_o} \phi_1 - \phi_2}{(\Delta x_2/\Delta x_1)^{p_o} - 1} \quad (3.29)$$

Validation

The second step in the error and uncertainty quantification phase is called validation. In this step, the numerical results are compared to experimental results to find whether the mathematical model resembles the physical problem well. The errors that can be identified in this step are for instance due the assumptions that were made to simplify the equations (Hickel [2019]). In addition, by using validation, the modeling errors that come from turbulence modeling or the boundary locations and conditions are assessed in this step. It should be noted that the experiment may also yield errors and inaccuracies as compared to the real world problem.

3.1.6. Commercial CFD-codes

There are various commercial CFD-codes available. A choice between these codes can be based on the application that it was designed for. In addition, due to the high costs of CFD-licenses, the code should be available to the researcher via the company or research institute. Sapkota [2018] showed that the erosion modeling capabilities of ANSYS Fluent are relatively extensive (as compared to for instance ANSYS CFX). Multiple erosion models are implemented and there is an option to add an additional erosion model through the User Defined Functions. In addition, the package has good capabilities of simulating liquid-solid flows. Therefore, Fluent is often used for modeling erosion in centrifugal pumps due to slurry flow (see for instance Huang et al. [2019] and Lai et al. [2018]).

Based on the previous discussion and the fact that the author of this Master's Thesis is already familiar with ANSYS CFX (which shows many similarities with ANSYS Fluent), it is decided that ANSYS Fluent is used during the current study.

3.2. Slurry flow modeling

Essentially, there are two methods that are often used for extending the theory of section 3.1 to include slurry flows. These methods differ in the way the solid phase is treated. The first method uses the Eulerian point of view to setup the equations for the solid particles. This implies that a fixed control volume is used in which the flow parameters are calculated. Since this framework is also applied to the conservation laws that are described in section 3.1, this method is also called the Eulerian-Eulerian method. Another point of view for setting up the equations of motion for the solid particles is the Lagrangian method. Here, the particles are tracked through space by using Newton's second law (Cengel and Cimbala [2006]).

According to ANSYS, Inc. [2020a], the Eulerian-Eulerian method should be used when the solid volume fraction is larger than 0.1. When the volume fraction is below or equal to this value, the Eulerian-Lagrangian approach gives the best results. Since this latter condition is the case for the current study, the Eulerian-Lagrangian method is adopted here. Therefore, only this method is treated in the current chapter. For an explanation of the Eulerian-Eulerian method, the reader is referred to the works of for instance Brennen [2005]

and [Yeoh and Tu \[2009\]](#).

Within the Eulerian-Lagrangian methods, there are three different ways to model the slurry flow. The first of these is called one-way coupling, where it is assumed that the particles have no influence on the flow of the fluid. In addition, particle collisions are not taken into account in this approach. These assumptions are justified when the volume fraction is sufficiently small or when the Stokes number is much smaller than 1 ([Andersson et al. \[2012\]](#)).

In the case that the Stokes number is larger than 1 or the volume fraction is sufficiently large (but not too large to have many particle-particle collisions), two-way coupling should be used ([Andersson et al. \[2012\]](#)). This means that also the influence of the solid particles on the fluid is taken into account.

A step further in terms of interaction modeling is required when the particles interact with each other considerably. When that happens, four-way coupled should be used. According to [Andersson et al. \[2012\]](#), collisions are typically important for a volume fraction larger than 0.01. In that case, four-way coupling is needed to obtain accurate results. In the current study, a volume fraction equal to 0.1 will be used, implying that four-way coupling should be used.

When tracking the solid material through the domain, either single particles or collections of particles can be considered. According to [Crowe et al. \[2012\]](#), the former case is also known as the Discrete Element Method (DEM). Here, the Lagrangian particle equations are solved for each particle in the flow, which gives a detailed description of the particle movements. However, this quickly becomes computationally expensive, since often there are many particles in a flow. Therefore, a more efficient approach is by tracking collections of particles, which is called the Discrete Parcel Method (DPM). Here, the particle equations are solved for groups of particles (parcels), which are assumed to behave as a large particles.

When using the Eulerian-Lagrangian method, the particles or parcels are treated as point masses. Therefore, according to [Zhang et al. \[2017\]](#), when using cells smaller than the particle size near the wall, the particle can get closer to the wall than its radius. When this happens, the particle is influenced by the near wall flow solution, leading to a reduced impact speed and with that a reduced erosion rate. This effect is illustrated in figure 3.5.

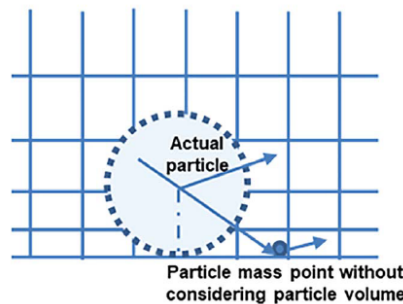


Figure 3.5: Effect of the particle diameter being greater than the first cell height in the mesh ([Wang et al. \[2021\]](#))

On the other hand, [Wang et al. \[2021\]](#) noticed that particles can get trapped in the region near the wall when the cells at that location are smaller than the particle radius. This leads to a severe overprediction of the erosion rates. It is for this reason that [Zhang et al. \[2017\]](#) and [Wang et al. \[2021\]](#) recommended to use a first cell height equal to or larger than the particle diameter and choose the appropriate wall treatment based on that. In the remainder of this section, the equations involved in the Eulerian-Lagrangian method are explained, starting with the force balance. This is followed by a description of the inclusion of turbulent dispersion. Then, the particle-fluid and particle-particle interactions are explained. Finally, a model for including particle-wall collisions is described.

3.2.1. Force balance

The force balance that is used to find the particle (or parcel) trajectories is based on Newton's second law and includes all forces that are acting on the particles. This equation was introduced by Basset, Boussinesq and Oseen (and is therefore named the BBO equation). At that time, it was only applicable to a uniform flow with a small particle Reynolds number ([Andersson et al. \[2012\]](#)). Later, this equation was adjusted to extend its applicability to higher Reynolds numbers and turbulent flows. The force balance including the relevant

forces for the current study is given by (Andersson et al. [2012]; ANSYS, Inc. [2020a]):

$$m_p \frac{dU_{i,p}}{dt} = F_{i,Drag} + F_{i,Buoy} + F_{i,Virt} + F_{i,Press} + F_{i,Rot} \quad i = 1, 2, 3 \quad (3.30)$$

In this equation, m_p is the mass of the particle, equal to $m_p = \pi d_p^3 \rho_p / 6$. In addition, the i -subscript refers to the vector component according to the Einstein notation and the subscript p is used for quantities related to the particle. The terms on the right-hand side represent the forces acting on the particle. These forces are described one-by-one in the following paragraphs.

Drag force

The first force that is considered here is the drag force. This term is also known as the steady state drag, since it represents the drag force in the case of a steady (not accelerating) relative velocity field (Crowe et al. [2012]). This relative velocity is also known as the slip velocity.

$$F_{i,Drag} = \frac{1}{2} \rho A_p C_{drag} \|\vec{U} - \vec{U}_p\| (U_i - U_{i,p}) \quad i = 1, 2, 3 \quad (3.31)$$

Here, A_p is the projected area of the particle normal to the flow (equal to $\pi d_p^2 / 4$). In addition, the term C_{drag} is the drag coefficient, for which various different models exist. For smooth, spherical particles, a general law called the Spherical Drag Law can be used (ANSYS, Inc. [2020a]; Yeoh and Tu [2009]):

$$C_{drag} = K_0 + \frac{K_1}{Re_p} + \frac{K_2}{Re_p^2} \quad (3.32)$$

In this equation, Re_p is the particle Reynolds number $Re_p = \rho d_p \|\vec{U} - \vec{U}_p\| / \mu$. Furthermore, K_0 , K_1 and K_2 are constants that have to be determined empirically. Values for these constant for different flow regimes can be found in Morsi and Alexander [1972]. In most practical or engineering flows, the drag force is the dominant force on the particle (Yeoh and Tu [2009]).

Buoyancy force

The buoyancy force arises from the density difference of the particles and the fluid. In mathematical terms, this force is given by (ANSYS, Inc. [2020a]):

$$F_{i,Buoy} = V_p g_i (\rho_p - \rho) \quad i = 1, 2, 3 \quad (3.33)$$

In this equation, V_p is the volume of a single particle, which is equal to $V_p = \pi d_p^3 / 6$.

Virtual mass force

When the particle accelerates through a fluid, a portion of the fluid is accelerated with it. This can be modeled as an additional mass, which is where the name virtual mass force comes from. This force can be written as (Andersson et al. [2012]):

$$F_{i,Virt} = -C_{VM} \rho V_p \left(\frac{DU_i}{Dt} - \frac{dU_{i,p}}{dt} \right) \quad i = 1, 2, 3 \quad (3.34)$$

According to Crowe et al. [2012], for the fluid acceleration the substantial or Lagrangian derivative D/Dt should be used. The virtual mass factor C_{VM} is often set equal to 0.5. The virtual mass force is relevant in cases where the fluid density is in the same order or higher than the particle density and large accelerations are present in the flow (Andersson et al. [2012]).

Pressure force

The pressure force is also named undisturbed flow force by Crowe et al. [2012], since it is related to both the pressure gradient and shear stresses in the undisturbed fluid flow (Andersson et al. [2012]):

$$F_{i,Press} = V_p \left(-\frac{\partial p}{\partial x_i} + \frac{\partial \tau_{ij}}{\partial x_j} \right) \quad i, j = 1, 2, 3 \quad (3.35)$$

In this equation, it is assumed that the pressure and shear stress do not change over the volume of the particle (Andersson et al. [2012]).

Rotational force

The rotational forces arise from rotating frames of reference (ANSYS, Inc. [2020a]). It includes the Coriolis (first term) and centrifugal forces (last two terms) and is equal to (Sapkota [2018]):

$$F_{i,Rot} = m_p \left(-2\Omega_j U_{k,p} \varepsilon_{jki} - \Omega_j r_j \Omega_i + \Omega_j \Omega_j r_i \right) \quad i, j, k = 1, 2, 3 \quad (3.36)$$

In this equation, r represents the position vector. In addition, ε_{jki} is the Levi-Civita symbol which is equal to 1 for an even permutation of the subscripts, -1 for an odd permutation and 0 in the case that one of the indices is repeated.

3.2.2. Turbulent dispersion

The particle tracking equation that is described in equation 3.30 does not take into account the turbulent fluctuations of the fluid flow (ANSYS, Inc. [2020a]). Since the fluctuations may be significant (especially for a highly turbulent flow), these have to be modeled. This can be done by including an additional force in equation 3.30, which models the effects of turbulent fluctuations on the particles.

On the other hand, there are stochastic models, which use statistical methods to calculate the turbulent dispersion. Within ANSYS Fluent, the turbulent dispersion is implemented in this way, for which there are two methods available (ANSYS, Inc. [2020a]). The first is called stochastic tracking (or Discrete Random Walk Model, DRW), where the fluctuating velocity is approximated using a random parameter. This fluctuating velocity lasts for a certain period of time (the integral time). During this period, the fluctuating velocity influences the particle trajectory. After the integral time, the random parameter takes a new value and the process repeats.

The second method is called particle cloud tracking, where statistical methods are used to model the turbulent dispersion of the particles from the mean particle trajectory (ANSYS, Inc. [2020a]). However, according to Ardakani [2016] this model is not accurate for simulations where the particles are treated as being unsteady, which is needed for modeling four-way coupling. Therefore, in the current study, the DRW model is adopted.

3.2.3. Particle-fluid interaction

In case of a two-way coupled method, the particles influence the fluid flow (besides the influence of the flow field on the particle trajectories). For a water-sand mixture, this is modeled using a momentum source term. This source term contains the different forces that are present in equation 3.30, except for the buoyancy term (Andersson et al. [2012]; ANSYS, Inc. [2020a]). The source term is simply added to the right-hand side of the momentum equation (the second part of equation 3.10). In addition, there is a source term involved in the turbulence equations, which accounts for the influence of the particles on the turbulence within the carrier fluid.

3.2.4. Particle-particle interaction

For slurries where the volume fraction of the particles is relatively high, particles collisions become so relevant that these have an influence on the trajectories of the particles. For the modeling of these collisions, there are two models that are usually being used (Crowe et al. [2012]): the hard and soft sphere models. According to Brennen [2005], the latter is usually considered to be the most complex and accurate one. Therefore, this model is used in the current study. For more information on the hard sphere model, the reader is referred to the work of Andersson et al. [2012].

As the name already suggests, the soft sphere model takes the particle deformation due to the collision into account. In this model, the forces in normal and tangential direction are split. In normal direction, the collision is modeled as a spring system (possibly augmented with a dashpot). This spring system can either be linear or non-linear. For the former, the force induced by the collision is equal to (ANSYS, Inc. [2020a]):

$$\vec{F}_{normal} = K_s \delta \vec{e}_{12} = \frac{\pi \|\vec{U}_{p,2} - \vec{U}_{p,1}\|^2}{3\varepsilon_D^2} D_{parc} \rho_p \delta \vec{e}_{12} \quad (3.37)$$

In this equation, K_s is the spring constant, δ is the overlap of the parcels (or particles) and ε_D is the fraction of the diameter that is allowed to overlap. In addition, D_{parc} is the diameter of the colliding parcels and \vec{e}_{12} is the unit vector between the two colliding parcels (or particles). This spring law can be augmented with the following dashpot term:

$$\vec{F}_{normal,dashpot} = \gamma \left[(\vec{U}_{p,2} - \vec{U}_{p,1}) \cdot \vec{e}_{12} \right] \vec{e}_{12} \quad (3.38)$$

The γ in this equation represents the damping coefficient. Although the non-linear contact model is considered to be more accurate and sophisticated, [Maio and Renzo \[2005\]](#) showed in their study that the linear model provides accurate results for the kinematic properties after collisions. For their comparison, they used the linear, as well as the non-linear spring-dashpot model. Since the linear model is less complex, this model is used during the current study.

In tangential direction, ANSYS Fluent offers two models. The first model is based on Coulomb's friction law ([ANSYS, Inc. \[2020a\]](#)):

$$F_{friction} = \mu_{coll} \|\vec{F}_{normal}\| \quad (3.39)$$

In this equation μ_{coll} is the friction coefficient that depends on the relative tangential velocity magnitude U_r ([ANSYS, Inc. \[2020a\]](#)):

$$\mu_{coll}(U_r) = \begin{cases} \mu_{stick} + (\mu_{stick} - \mu_{glide}) \left(\frac{U_r}{U_{glide}} - 2 \right) \frac{U_r}{U_{glide}}, & U_r \leq U_{glide} \\ \mu_{glide}, & U_{glide} < U_r \leq U_{limit} \\ \mu_{glide} \frac{1 + (U_r - U_{limit}) / \alpha_{limit}}{1 + \mu_{glide} (U_r - U_{limit}) / (\alpha_{limit} \mu_{limit})}, & U_r > U_{limit} \end{cases} \quad (3.40)$$

In this function, the parameters μ_{stick} , μ_{glide} , μ_{limit} , U_{glide} , U_{limit} and α_{limit} are constants. According to [Lambert et al. \[2017\]](#), these constants, in combination with the damping coefficient γ , have to be determined by using either literature or experiments.

The other tangential collision model takes rolling friction into account, which is not relevant in the current study. According to [ANSYS, Inc. \[2020a\]](#), the collision model is included as an additional force term in the particle trajectory equation (equation 3.30).

3.2.5. Particle-wall rebound

In addition to particle-particle interactions, the collisions of particles with the wall are of importance for dense or wall-dominated dilute flows ([Crowe et al. \[2012\]](#)). This includes the damage to the wall that is done by the particles (erosion) as well as the rebound of particles from the wall. According to [Andersson et al. \[2012\]](#), due to the rebound, the particle loses kinetic energy, which dissipates as heat. [Grant and Tabakoff \[1975\]](#) proposed an empirical model for the restitution parameters (ratios of normal and tangential velocities before and after the collision) with a dependency on the particle impact angle. This model is based on a statistical analysis of the rebound behaviour of particles. By using a Least Squares polynomial fit through the mean values, two straightforward equations were found for the restitution parameters in normal and tangential direction, e_N and e_T respectively:

$$\begin{aligned} e_N &= \frac{U_{N2}}{U_{N1}} = 0.993 - 1.76\alpha + 1.56\alpha^2 - 0.49\alpha^3 \\ e_T &= \frac{U_{T2}}{U_{T1}} = 0.988 - 1.66\alpha + 2.11\alpha^2 - 0.67\alpha^3 \end{aligned} \quad (3.41)$$

In these equations, α represents the angle in radians between the particle trajectory and the wall just before the collision.

Since comparisons between different rebound models as performed by [Peng and Cao \[2016\]](#) and [Pereira et al. \[2014\]](#) showed that the Grant and Tabakoff model gave superior results, this model is used in the current study.

3.3. Erosion modeling

In section 2.3, it is shown that the erosion rate due to the impingement and sliding of solid particles depends on many factors. Therefore, according to [Hafid \[2018\]](#), it is difficult (or even impossible) to find a model that is suited for all situations. Often, there are models that can only be used for certain flow regimes. In addition, these models have to be tuned using experimental data before they can be applied to a certain problem.

The first commonly used erosion model (which was adopted by [Sapkota \[2018\]](#)) is the Finnie model. [Finnie \[1960\]](#) showed that this model shows good correspondence with experimental data for lower impact angles. However, for angles larger than 45° , the model severely underpredicts the erosion rate. These experiments were conducted for relatively large particle velocities. Another disadvantage of the model is that there is no parameter that is related to the diameter or shape of the particles.

Other common erosion models are the E/CRC (formulated by the Erosion/Corrosion Research Center at the

University of Tulsa, Zhang et al. [2017]) and the Oka model (Oka et al. [2005a]). As compared to the Finnie model, these models take more parameters into account, such as the hardness of the target material and particle parameters (the particle diameter for the Oka model and the particle shape for the E/CRC model). Among others, the performance of the Oka model and E/CRC model was compared for an electrical submersible pump (ESP) by Zhu et al. [2019]. In this study, it was concluded that the Oka model performed the best for the impeller of the pump. When considering the complete pump, both the E/CRC and the Oka model gave results with the smallest error with respect to the experiment. The fact that both the E/CRC and Oka models are equally accurate was confirmed by Zhang et al. [2007], when they compared the performance of the E/CRC and Oka models. This comparison was executed on both water-sand and air-sand mixtures flowing through a 90° pipe bend. In the same study, it was found that, although both the Oka model and the E/CRC model are developed for high particle velocities, they perform well for low impact velocities (in the same range as the velocities that occur in the current project) as well.

As said before, in the Oka model, the particle size is taken into account, whereas particle variation in the E/CRC is included in the sharpness factor. In general, the evaluation of the diameter is more convenient than the evaluation of the shape of the particle. In addition, the Oka model was tested for a large range of particle diameters (including the diameters that occur in the dredge pump impeller), whereas only relatively small particles diameters were used in the experiments for establishing the E/CRC model. Finally, the E/CRC model was developed by using the material Inconel 718, whereas the Oka model is tested for more materials. Therefore, it is concluded that the Oka model is most suitable for the current study.

The Oka model, as proposed by Oka et al. [2005a], was especially developed to be applicable to many different materials under various conditions. For this, the impact velocity, impact angle, particle size and material hardness are taken into account. The model calculates the erosion rate in terms of volume ER_v from the same erosion rate at an impingement angle of 90°, with the use of an impact angle dependency function $f(\alpha)$:

$$ER_v = \frac{E_v}{m_p} = ER_{v,90} f(\alpha) \quad (3.42)$$

The impact dependency function was found to be equal to:

$$f(\alpha) = \sin^{n_1}(\alpha) [1 + Hv(1 - \sin(\alpha))]^{n_2} \quad (3.43)$$

This function includes two coefficients (n_1 and n_2) and the material Vicker's hardness Hv . The coefficients themselves also depend on the hardness of the target material (Oka et al. [2005a]):

$$n_1 = s_1 (Hv)^{q_1} \quad n_2 = s_2 (Hv)^{q_2} \quad (3.44)$$

The values of the empirical constants in this equation ($s_{1,2}$ and $q_{1,2}$) can be found in table 3.1. Essentially, the impact angle dependence function consists of a part that represents the cutting action as well as a part for the repeated deformation. This is illustrated in figure 3.6.

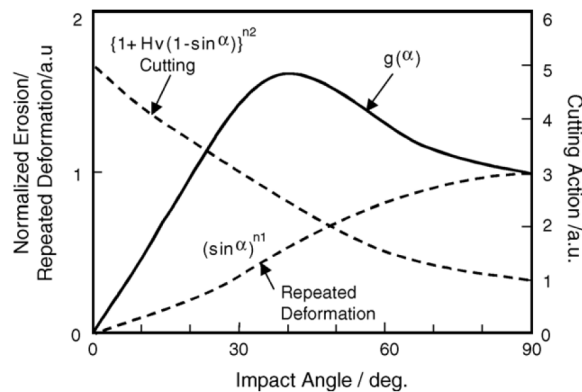


Figure 3.6: Impact angle dependence function for the Oka erosion model (Oka et al. [2005a]). This function is composed of a cutting term and a term that accounts for the repeated deformation. The combination of the two gives the actual function that is used in the Oka model (equation 3.43). In this figure, the function is named $g(\alpha)$, instead of $f(\alpha)$.

The erosion rate for a normal impact was defined by Oka et al. [2005b] in the following way:

$$ER_{v,90} = K (aHv)^{k_1 b} \left(\frac{U_p}{U^*} \right)^{k_2} \left(\frac{d_p}{d^*} \right)^{k_3} \quad (3.45)$$

In this equation, the constants K , k_1 and k_3 are dependent on the particle properties, whereas k_2 is determined both by the material hardness and the particle properties. Moreover, a and b are empirical coefficients. The quantities U^* and D^* are the standard impact velocity and the particle diameter, which were used in the experiments for the determination of the erosion correlations (Oka et al. [2005b]).

The different constants that occur in the Oka model for two types of sand (SiO₂ and SiC) can be found in table 3.1.

Table 3.1: Different constants for the Oka erosion model (Oka et al. [2005a]; Oka et al. [2005b])

Type	K [-]	k_1 [-]	k_2 [-]	k_3 [-]	U^* [m/s]	D^* [μm]	s_1 [-]	q_1 [-]	s_2 [-]	q_2 [-]
SiO ₂	65	-0.12	$2.3(Hv)^{0.038}$	0.19	104	326	0.71	0.14	2.4	-0.94
SiC	45	-0.05	$3.0(Hv)^{0.085}$	0.19	99	326	0.71	0.14	2.8	-1.00

Oka et al. [2005b] conducted experiments to determine the relationship between the erosion rate for normal impact and the material hardness. By approximating these results with the exponential function from equation 3.45, they determined the values of the constants a and b for different materials.

In table 3.1, it is shown that the Oka model was developed for high particle velocities. However, Zhang et al. [2007] showed that the model also yields good results for low speeds and small particles.

3.4. Conclusion

This chapter can be summarized by a scheme as shown in figure 3.7, which includes the different steps within the numerical model. The dashed part of this figure is optional, depending on the coupling type of the method.

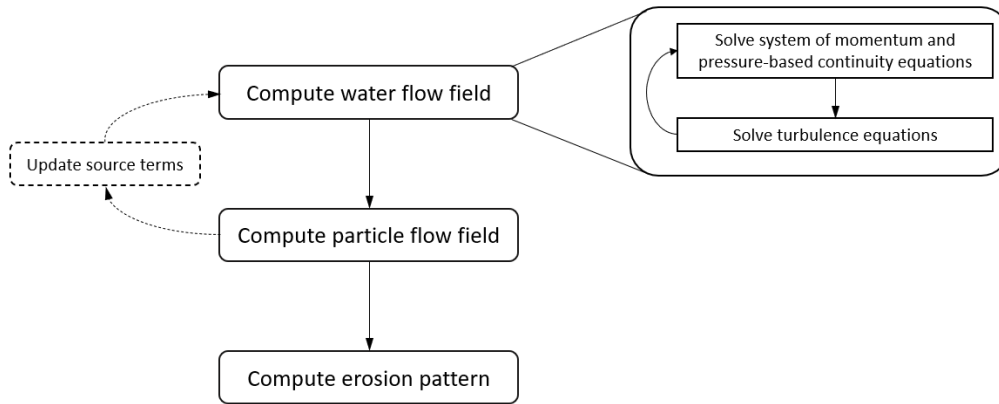


Figure 3.7: Schematic overview of the numerical model that is used to calculate the erosion pattern due to solid particles impacting a target surface. The dashed part of the figure is only included for the two-way coupled and four-way coupled methods. In addition, the right-hand side represents the steps that are taken to compute the water flow field.

There are three different methods within the Eulerian-Lagrangian model. For all of those methods, the first step is to calculate the converged water flow field. This is done by iteratively solving the momentum, continuity and turbulence equations. The continuity equation is modified such that it is essentially a pressure correction equation. For the turbulence equations, the k - ω SST turbulence model is used.

After obtaining the converged fluid flow field, the particle flow field is calculated using Newton's second law for sets of particles, named parcels. Finally, there is the calculation of the erosion pattern based on the impact of the particles. For this, the Oka erosion model is used which takes into account the impact angle and velocity of the individual parcels hitting the target surfaces. The energy loss that is involved when a particle

collides to a solid wall is modeled using the Grant-Tabakoff rebound model.

In the case of one-way coupling, the dashed part in figure 3.7 is omitted. This implies that, for this method, the water flow field, particle flow field and erosion patterns are computed sequentially. In the two-way coupled method, the water and particle flow fields are solved multiple times (indicated with the dashed arrows in figure 3.7) in order to take into account the influence of the particles on the water. This is done by including particle source terms in the water momentum and turbulence equations. By using an additional extension of the model, the four-way coupled method is obtained. Here, also the forces due to inter-particle collisions are taken into account when calculating the particle flow field. This is done using the linear soft sphere collision model (also known as the DEM-model). It is shown that for this model, a great number of constants are required that have to be determined by using experimental data.

A concise overview of the equations that are used in the numerical model is shown in appendix A.

4

Experimental Setup

In order to assess the validity of a numerical model, an experimental validation is invaluable. Since in literature, detailed experimental data on this subject are limited, carrying out experiments is part of the present study. In this chapter, the setup and results of the experiment are discussed.

In the first section of this chapter, the facility that is used for the experiment is introduced. This is followed by an explanation of the experimental conditions. After that, the method to measure the erosion on the impeller blades is described. Finally, the post-processing procedure and the results are discussed.

4.1. Facility

For the experiments, a facility is used that is operational and available with the company Damen Dredging Equipment. This circuit is known as the "Testloop" and can be seen in figure 4.1.

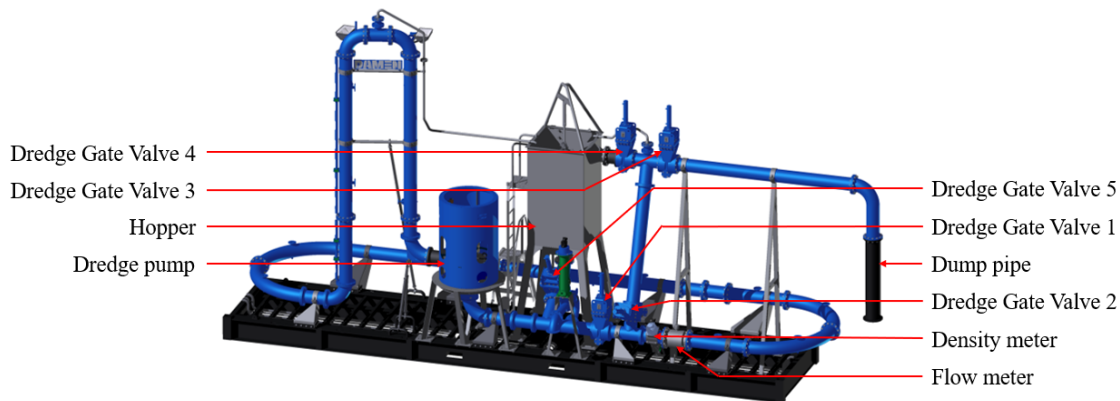


Figure 4.1: The "Testloop" facility that is available within the company Damen Dredging Equipment (figure adapted from [Visscher \[2012\]](#)). The for this project relevant components are mentioned in this figure.

Starting from the dredge pump, the mixture flows through the vertical U-bend and a horizontal 180 degree bend. After encountering a long horizontal pipe and another 180 degree bend, the flow enters a section with a density and a flow meter. During the erosion experiment, Dredge Gate Valve 2 (DGV2) is closed, which allows the mixture to flow directly back to the dredge pump. Therefore, during the experiments, the circuit is a closed-loop system. When DGV2 is opened, the mixture can be forced through the hopper or the dump pipe which allows the user to control the sand concentration within the circuit.

In the following subsections, the description of the installed sensors is elaborated. In addition, the dredge pump that is installed in the Testloop is discussed.

4.1.1. Installed sensors

As shown in figure 4.1, there are a number of sensors integrated in the circuit. The first is a flow meter, which measures the velocity (averaged over the cross sectional area) of the mixture that flows through the pipes. This flow meter induces a magnetic field inside the pipe (KROHNE [2011]). Due to the electrical conductivity of the fluid, a voltage is generated. This voltage can then be measured and converted into the mean velocity of the mixture. The flow meter is capable of measuring flow speeds up to 12 m/s with an accuracy of $\pm 0.2-0.3\%$. Since the diameter of the pipes is known, the result of this velocity meter can easily be converted to the flow rate Q :

$$Q = \pi \left(\frac{D_{pipe}}{2} \right)^2 U_{mean} \quad (4.1)$$

Another important quantity for the experiments is the concentration of the mixture. For this, the circuit is equipped with a density meter. According to Berthold Technologies [n.d.], this density meter makes use of a radioactive source. The gamma radiation that is transmitted by the source is attenuated by the mixture after which the remaining intensity is measured with a detector. By making use of the dependency of the attenuation ratio on the density of the absorbing material, the density of the mixture, averaged over the cross sectional area, can be obtained. VBKO [1998b] showed that the density can be converted into the spatial volumetric concentration C_{vs} by using the following relation:

$$C_{vs} = \frac{\rho_m - \rho_l}{\rho_p - \rho_l} \quad (4.2)$$

In addition to these two flow monitoring sensors, there are differential pressure sensors installed in the circuit. Due to the fact that these are placed directly upstream and downstream of the pump, the sensors can be used to measure the performance (head) of the pump. The pressure sensors can measure differential pressures between 50 kPa and 16000 kPa with an accuracy equal to $\pm 0.2\%$. In addition, for controlling and registering the rotational speed of the pump, a sensor is installed that measures this speed.

The measured values of all of these sensors can be logged with a frequency equal to 1 Hz . Using these log-files, the conditions within the Testloop can be found at any moment during the experiments.

4.1.2. Dredge pump

The dredge pump that is installed in the Testloop is the BP2525MD model (see figure 4.2). This pump has both an impeller inlet and volute outlet diameter that is equal to 250 mm . In addition, BP stands for "Bagger-pomp" (dredge pump) and MD for "Medium Discharge". The latter of these is related to the head that can be achieved with this pump type.



Figure 4.2: 3D-model of the BP2525MD centrifugal dredge pump

The pump has a three-bladed impeller, which ensures a large spherical ball passage and with that, a relatively easy passage of large particles. The outer diameter of the impeller is 635 mm , whereas its height measures 180 mm . The material that is used for the impeller is a cast iron alloy named Bainitic Nodular, which has

a density of approximately 7800 kg/m^3 and a Vickers hardness between 3.54 GPa and 3.98 GPa (Markus [2020]). A cross-section of the impeller can be seen in figure 4.3.

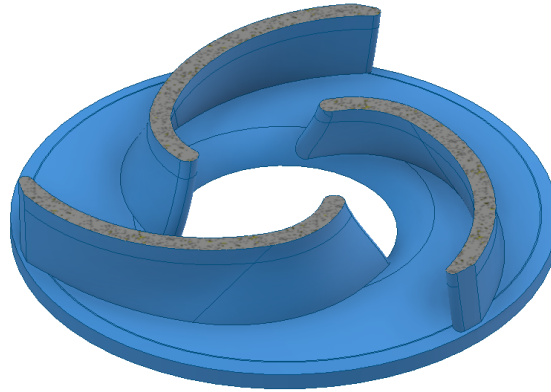


Figure 4.3: Cross-section of the BP2525MD centrifugal dredge pump impeller

Typically, centrifugal dredge pumps operate in their best efficiency conditions (BEP-conditions). For this pump, rotating with 600 revolutions per minute, these conditions are listed in table 4.1.

Table 4.1: Best efficiency conditions for the BP2525MD centrifugal dredge pump

Parameter	Value
n [1/s]	10
Q_{BEP} [m^3/s] ($[m^3/h]$)	0.208 (748.86)
H_{BEP} [m]	20.75
η_{BEP} [-]	76.63
P_{BEP} [W]	55

From the performance parameters at the BEP, the specific speed of the pump can be calculated in the following way:

$$n_s = \frac{n\sqrt{Q_{BEP}}}{H_{BEP}^{3/4}} = 0.469 \text{ m}^{3/4}/\text{s}^{3/2} \quad (4.3)$$

4.2. Experimental conditions

As mentioned before, centrifugal dredge pumps are designed to operate at their Best Efficiency Point. Therefore, it is most useful to be able to estimate and validate the erosion at those conditions. As in this Testloop it is not possible to set the different parameters with high accuracy, in this section, the intended conditions are compared to the actual conditions averaged over the experimental time.

While aiming for a rotational rate of 10 1/s , the average value during the experiment turned out to be 9.94 1/s . For the intended rotational rate, the average velocity for the Best Efficiency Point is equal to:

$$U_{mean} = \frac{Q_{BEP}}{\pi(\frac{1}{2}D_{pipe})^2} = 4.24 \text{ m/s} \quad (4.4)$$

During the experiment, this velocity ended up to be equal to 4.301 m/s . This indicates that the pump did operate slightly above its Best Efficiency Point.

For the sand, two parameters are of main importance for the experiment. These are the volume fraction or concentration and the (mean) particle diameter. For the former, it is important that it is not too large, since the numerical model that is used gives inaccurate results for concentrations higher than 10%. On the other hand, the concentration should not be too small, since this would reduce the erosion wear on the impeller. Due to the limited amount of time that is available for this project, a shorter experimental time is preferable. It is for these reasons that a concentration equal to 10% is chosen beforehand. After performing the experiment, it turned out that the average concentration during the experiments was equal to 9.95%.

For the particle diameter, it is again important not to use particles that are too small, since this would increase the required experimental time. On the other hand, for particles that are relatively large, the concentration within the Testloop is difficult to control. This might be due to the non-homogeneous distribution of the sand particles, which is more pronounced for larger particles. In the past, particles with a mean diameter of 0.5 mm have already proven to satisfy the latter condition within the Testloop. Therefore, a mean diameter close to this value is used during the current study. Due to the availability of the sand, it was not possible to use the same sand type during the entire experiment. Therefore, two different types are used, from which the PSDs are shown in figure 4.4.

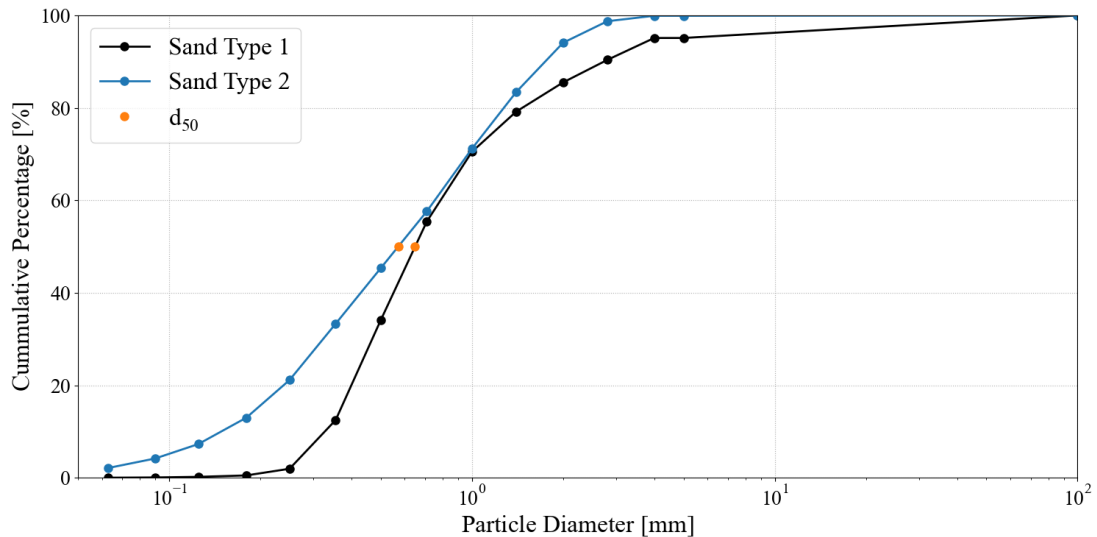


Figure 4.4: Particle Size Distributions for the two different sand types that are used during the experiment. The d_{50} diameters for both types are shown in orange.

In this figure, it can be seen that, although there is a noticeable difference in the distribution of the particle diameters, the difference in d_{50} between the two sand types is relatively small. Therefore, it is expected that the use of the two types of sand only has a minor influence on the impeller blade erosion. Taking the experimental time into account, the average d_{50} diameter during the experiment was equal to 619 μm .

In general, when circulating a sand-water mixture through a closed-loop system, the sand particles degrade due to the collisions with other particles and with the walls. While using the Testloop, it is not possible to take a representative sample of the sand flowing through the circuit to estimate this effect. In the experimental study by Sadighian [2016], a mixture of water and sand (with a volumetric concentration of 20% and a mean diameter equal to 420 μm) was circulated through a closed loop pipeline at a velocity of 4 m/s for four weeks. It was found that the mean diameter was still the same after one week, while showing a small difference with the initial value after four weeks. In addition, the mass fraction of particles with a diameter smaller than 0.21 mm increased from 1.1% to 2.0% during the first week. Since the conditions used by Sadighian [2016] are similar to the conditions in the current study, it is expected that, by refreshing the sand about every 9 hours, the effect of particle degradation is minimized. Therefore, this frequency is used during the experiment.

Besides the particle diameters, the sand is also often characterized by the shape of the particles. In the current study, an erosion model is used that does not take this parameter into account. Therefore, the shape of the particles is not directly relevant for the validation of this model.

A summary of the experimental conditions averaged over the experimental time can be found in table 4.2.

Table 4.2: Experimental conditions averaged over the experimental time

Parameter	Value
n [1/s]	9.94
U_{mean} [m/s]	4.301
C_{vs} [%]	9.95
d_{50} [μm]	619

4.3. Duration of the experiment

The duration of the experiment determines the visibility of the erosion wear on the impeller blades. Therefore, the experiment should last long enough such that the erosion wear can be measured accurately. On the other hand, a long experiment may involve a geometry change of the impeller which in turn alters the flow and erosion behaviour. This means that the duration of the experiment should be chosen carefully beforehand.

For this, an experiment by [Sellgren et al. \[2005\]](#) was used, who compared the erosion wear in different centrifugal pumps using numerical simulations. The selected centrifugal pumps had specific speeds ranging from 0.4 to 1.4 $m^{3/4}/s^{3/2}$, which all operated at a prescribed head. This implies that the pumps did not operate exactly at their Best Efficiency Points. From these simulations, they found a correlation between the ratio of the total vane area and the square of the suction diameter and the average impeller vane wear rate. This was recorded for the conditions that are shown in table 4.3.

Table 4.3: Conditions used in the computations by [Sellgren et al. \[2005\]](#)

Parameter	Value
C_{vs} [%]	10
H [m]	50
d_p [μm]	300

The ratio of the total vane area and the square of the suction diameter of the pump that is used in the current study is equal to:

$$\frac{\text{Total Vane Area}}{D_0^2} = 2.15 \quad (4.5)$$

According to [Sellgren et al. \[2005\]](#), this results in an average wear rate on the impeller blade that is equal to 2.9 $\mu m/h$.

In the current study, the pump operates at its Best Efficiency Point, which in general yields less erosion wear. In addition, the conditions that are described in table 4.3 are not the same as the conditions of the current study. However, despite these differences, the estimation given by [Sellgren et al. \[2005\]](#) still gives a rough idea of the erosion wear rate that can be expected.

Based on the availability of the Testloop and the available amount of time within the project, the duration of the experiment was chosen to be around 55 hours. From the correlation found by [Sellgren et al. \[2005\]](#), an average thickness loss on the impeller blades of around 160 μm could be expected. Given the accuracy of the device used to measure the erosion (see section 4.4), this amount of wear is sufficient to accurately determine the erosion wear on the blades (which is demonstrated in section 4.6). On the other hand, since the blade thickness is 25 mm, this amount of erosion does not have a significant effect on the flow (and with that, the subsequent erosion pattern).

The exact duration of the experiment, which is needed for the validation of the numerical model turned out to be 55.7 hours. Here, the time to start and stop the system are not taken into account.

4.4. Erosion measurement

For the quantification of the erosion wear, a Coordinate Measurement Machine (CMM) is used. This device measures the x-, y- and z-coordinates (relative to a reference frame defined on the object) of discrete points that are located on the surfaces of the measured object ([Keyence Corporation \[n.d.\]](#)). These points can either be measured using a contact probe or an optical probe. The main advantage of the CMM is that it can measure complex geometries with a high accuracy.

The CMM that is used during the current study is the CRYSTA-Apex S1200 series (see figure 4.5). This device is capable of measuring objects with dimensions up to 1205 × 3005 × 1005 mm ([Mitutoyo \[n.d.\]](#)). For this, the theoretical accuracy of the machine is defined in the following way ([Mitutoyo \[n.d.\]](#)):

$$\text{Accuracy} = 2.3 + \frac{0.3L}{100} \mu m \quad (4.6)$$

In this equation, L is a measure for the size of the object in millimeters. In practice, the accuracy also depends on factors related to the state of the object, such as the roughness. Therefore, the practical accuracy will

generally be lower than its theoretical counterpart. The resolution of the device can be as low as $0.1 \mu\text{m}$ (Mitutoyo [n.d.]).



Figure 4.5: CRYSTA-Apex S121210 Coordinate Measurement Machine (Mitutoyo [n.d.])

The thickness loss due to erosion wear at the different measured points can be found by comparing the CMM measurements of the impeller before and after the wear experiment. For this, the CMM can be programmed such that it measures the same profiles during both measurements.

Although these do exist, there was no long measurement probe available on short notice. Therefore the CMM was not able to measure the entire blade. More specifically, the Leading Edge and a part of the Suction Side of the blade are not included in the experimental erosion results. In addition, the parts of the blade that are close to the hub and shroud of the impeller are not measured.

4.5. Post-processing

As mentioned before, two sets of measurements (measured before and after the experiment) are obtained from the CMM. From this, the erosion at those points can be calculated. However, after measuring for the second time, it turned out that the impeller was not aligned in the exact same way during the two measurements. In figure 4.6, this is visualized by plotting the points of the measurement before the experiment and the points after the experiment for a certain height on a horizontal plane.

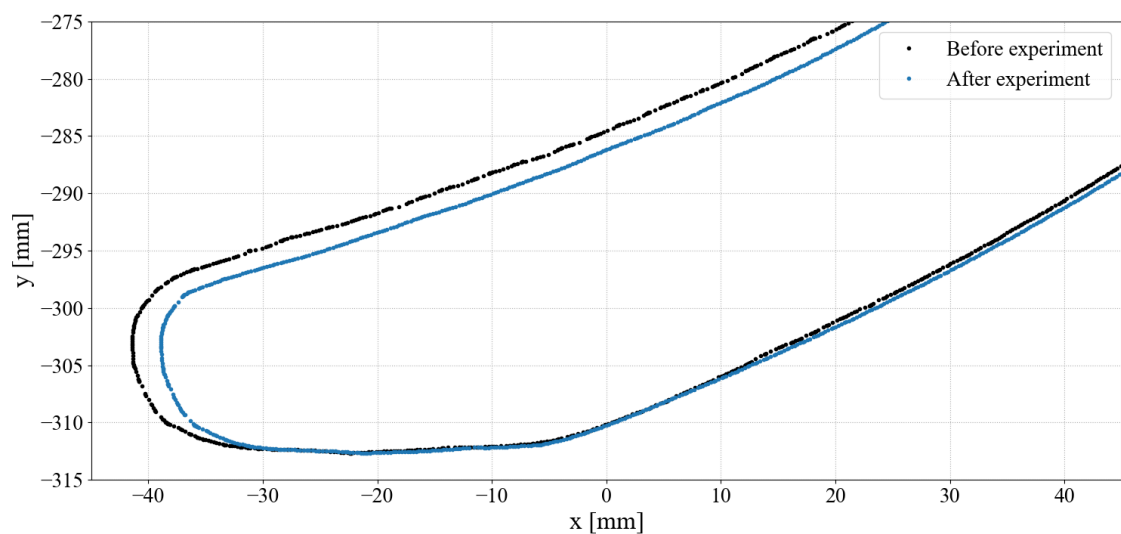


Figure 4.6: Measured points before and after the experiment near the Trailing Edge of one of the impeller blades

This graph is zoomed in at the Trailing Edge, which is located at the left part of the figure. It can be seen that for this particular profile, material is removed from the Suction Side (upper part of the profile), whereas material seems to be added to the Pressure Side (lower right part of the profile).

To correct for this misalignment, the profiles have to be shifted such that the erosion on the impeller blade is physically meaningful. Since the z -coordinate was used as input for the measurements, the variables that can be used for shifting the profiles are the translation in x -direction, the translation in y -direction and the rotation around the z -axis.

There are different methods for finding the optimal values for the aforementioned parameters:

1. The first option is to use a Least Squares fit at the locations where the minimum erosion is expected. This expected minimum erosion zone could be found using the numerical model for the impeller. However, since the experimental results are intended to be used as validation for the numerical model, this option would compromise this goal. The minimum erosion zone could also be found using similar studies in literature. However, since there are many parameters involved in erosion studies, it is difficult (if not impossible) to find a case that is sufficiently comparable.
2. A slightly different method for shifting the profile would be to compare the roughness of the profiles before and after the experiment. The locations where the roughness did not change can then be used for the Least Squares fit. Therefore, this method is based on the assumption that the roughness of the impeller changes under the influence of erosion wear.
3. The third method is based on the idea that no material addition can occur anywhere on the impeller blade. For that, the three parameters can be altered such that the negative erosion is minimized. By doing this for all nine profiles on all the three blades simultaneously, the optimal values for these parameters can be found.

Since the last option automatically disqualifies the results that are not physical, this is the most appropriate option. In addition, the second method can be used to verify whether the obtained shift is indeed correct. By using this combination of the methods, the actual erosion on the impeller blade can be calculated with reasonable certainty. In figure 4.7, the roughness profiles that are measured before and after the experiment are shown along the curve length for a single profile. In addition, the erosion profile is included to show the relation between the roughness change and the erosion. At the right-hand side of figure 4.7, the definition of the curve length is given.

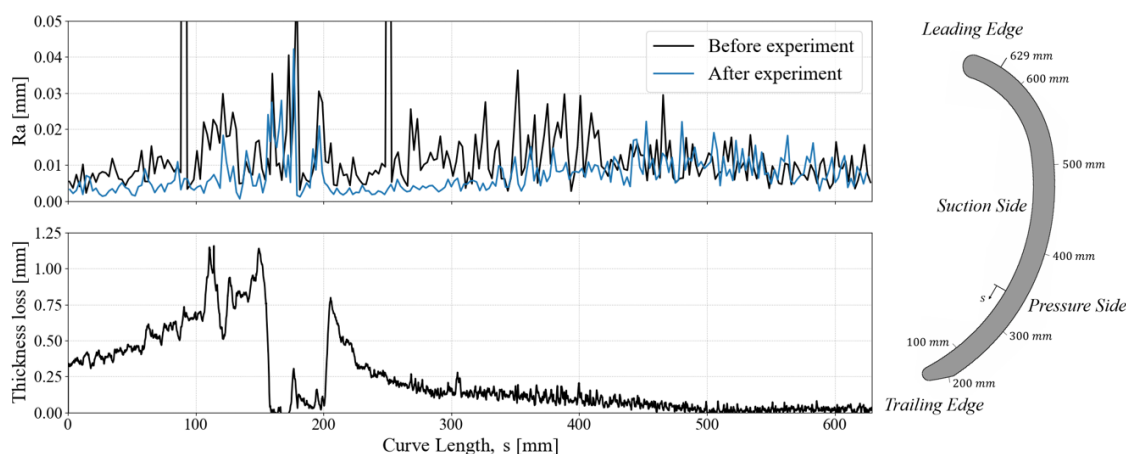


Figure 4.7: Relation between the change in roughness profiles (quantified in terms of the arithmetical mean roughness, Ra) and the thickness loss. On the right-hand side, the definition of the curve length is explained.

The roughness in figure 4.7 is quantified in terms of the Ra , which, according to Mitutoyo [2016], is the arithmetical mean roughness value. To determine this quantity, the first step is to divide the measurement points in sampling sets of 10. By fitting a linear curve through these points, the deviation from this line can be calculated. The Ra is then defined as this deviation averaged over the sampling set.

It can be seen that, at the locations where the erosion rate is relatively high, there is a noticeable difference between the roughness profiles before and after the experiment. Moreover, at the locations where the erosion is close to zero (for instance near the Trailing Edge and close to the Leading Edge at the Pressure Side), there is a much smaller difference between the roughness profiles before and after the experiment. The comparison of the roughness is a relatively crude way to identify the zones with maximum erosion. However, in combination with the minimization of material addition, it does provide a good certainty for the experimentally determined erosion on the impeller blade.

After shifting the graph such that the negative erosion is minimized and calculating the erosion on the individual blades, the erosion can be averaged over the three blades to get the final erosion results.

4.6. Results

By using the post-processing procedure that is described in the previous section, the erosion at the measured region of the impeller can be calculated. The contours of this quantity are shown in figure 4.8a and figure 4.8b for the Pressure Side and the Suction Side, respectively. In this figure, the experimental results are shown on the numerical domain that is clarified in section 5.2. In addition, the areas of the impeller where there were no measurements are colored grey. The erosion itself is quantified in terms of the thickness loss in meters and for the regions between the different points, a linear interpolation is used.

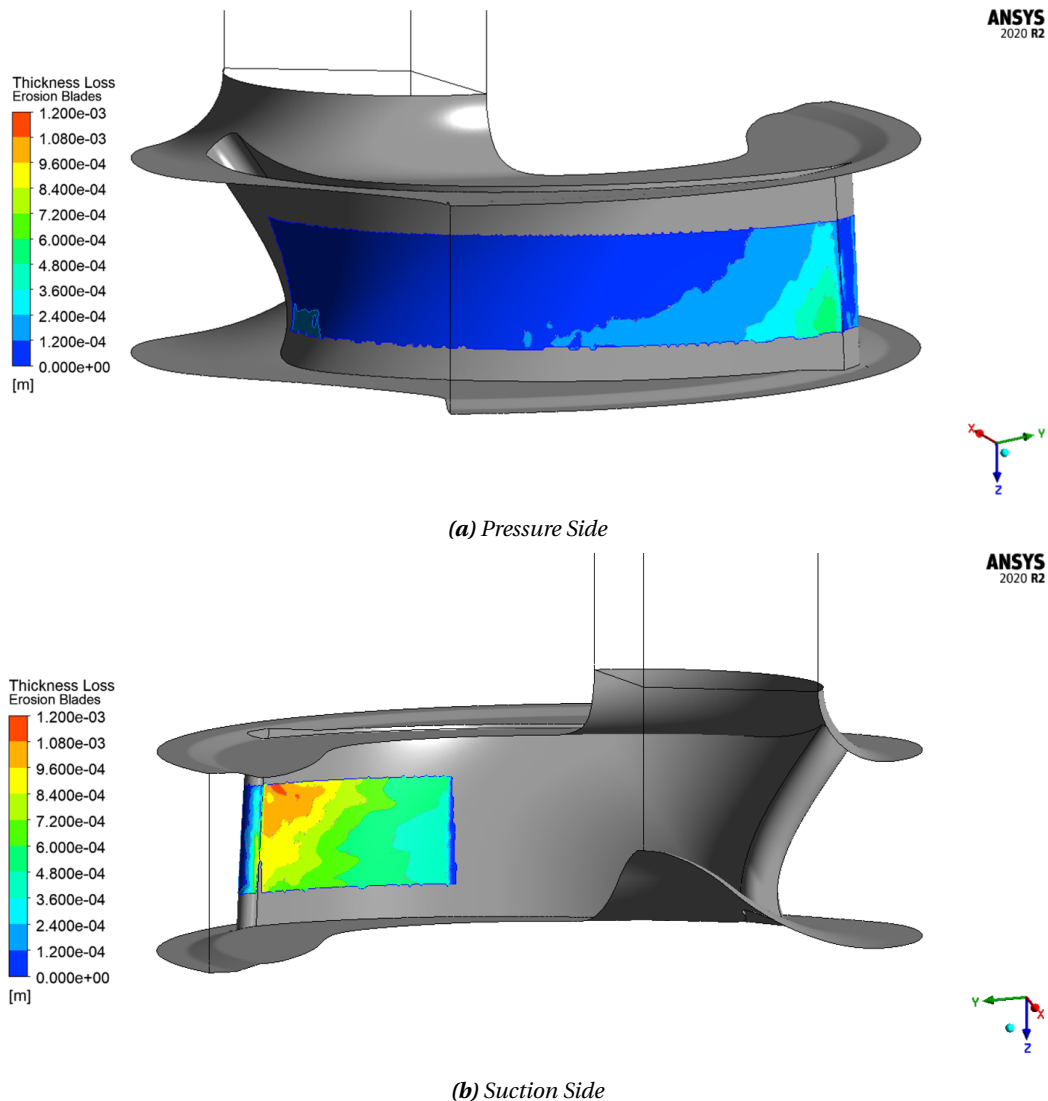


Figure 4.8: Contour of the experimental thickness loss averaged over the three blades. The erosion at the grey parts of the blade is not measured.

In their study, [Krüger et al. \[2010\]](#) showed that the erosion at the Leading Edge of the blade is due to shock-like processes, whereas along the blade, the friction-like process dominates. Therefore, the greatest part of the erosion that is shown in figures [4.8a](#) and [4.8b](#) can be attributed to particles sliding over the surface or impacting the surface with a shallow angle.

It can be seen that there is more erosion occurring on the Suction Side than on the Pressure Side. It is also on this side of the blade (close to the Trailing Edge) where the maximum thickness loss occurs. For both sides it can be concluded that the erosion increases when moving towards the Trailing Edge. This might be due to the turbophoresis effect, which, according to [Schlatter et al. \[2012\]](#), causes the particles in a wall-bounded flow to move towards the region near the wall. This results in a positive erosion gradient in the direction of the mean flow. Another explanation for the increase in erosion rate towards the trailing edge would be that the absolute particle velocities increase with increasing distance from the impeller centre ([Lai et al. \[2018\]](#)). This also increases the velocity with which the particles impact the blade. Thirdly, there may be recirculation zones on one of the two (or both) sides, leading to an increase in erosion rate at the location. Since the particle or fluid velocities were not measured during the experiment, an attempt has been made in chapter [5](#) to identify phenomena that cause the erosion pattern by using the numerical results.

At the Trailing Edge itself, the erosion is rather small. This is due to the inertia of the particles, which results in the fact that these cannot follow the curved streamlines of the water at that location. This leads to a low local volume fraction around the Trailing Edge and therefore a low erosion rate.

5

Numerical Results

In this chapter, the results of the numerical study are discussed. This discussion is split into three different parts. The first part consists of a validation study against a benchmark problem to demonstrate the validity of the numerical model. Then, a verification study is done using the impeller setup to find the optimal parameters for this setup. Finally, a detailed comparison between the numerical and experimental erosion results is performed in order to validate the numerical model for the impeller.

An important note for the four-way coupled simulations is that there are many parameters involved in the collisions of particles (see section 3.2.4). Moreover, Lambert et al. [2017] showed that for the majority of these parameters, experimental data are needed to determine their values. In the case that detailed experimental data are unavailable, they recommended the use of the default values. Therefore, this is the approach that is used in the current study.

Since this approach introduces an uncertainty in the four-way coupled simulations, the results involving particle tracking in this chapter are all based on the two-way coupled method, unless otherwise specified.

5.1. Benchmark study: Impinging jet

For the first part of the numerical study a benchmark study is used to show the validity of the numerical model for a relatively easy setup. In addition, this provides a deeper understanding of the numerical model prior to applying it to the complex case of a centrifugal dredge pump impeller. For the benchmark, an impinging jet submerged in water is used, because of the availability of experimental results in literature for this setup. In addition, the impingement of slurry flow on an object also occurs in the impeller of a centrifugal dredge pump, for instance at the Leading Edge of the blade.

In order for the benchmark to be useful as a validation study, the flow should be comparable to the flow that can be expected in the impeller. This means that the flow of the fluid and the particles for both cases should be in the same regime. According to Oliemans [2001], an important parameter for fluid flow similarity is the Reynolds number. A turbulent pipe flow can be expected for Reynolds numbers larger than 2300. Using the flow conditions for the impeller (which are listed in chapter 4.2), it can be found that the Reynolds number at the inlet of the impeller is equal to 1.1×10^6 . This means that the flow can be considered turbulent. Therefore, the flow exiting the nozzle of the impinging jet should also be turbulent.

For a comparable particle flow, it is important to have a similar Stokes number (Oliemans [2001]). As mentioned before, the value of this parameter describes the influence of the fluid on the particle flow. For the flow through the impeller, the Stokes number is equal to 1.05. This means that the benchmark should have a Stokes number that is close to this value.

According to Oliemans [2001], there are additional parameters that are important for the dynamic similarity of slurry flows. However, since the flow in the benchmark should only be comparable to the flow in the impeller, it is sufficient to use a benchmark study where the Reynolds number and the Stokes number fall in the same regime as for the impeller.

The benchmark problem is split into three parts. The first part comprises of a validation of the fluid flow field. Secondly, the computed particle flow field is compared to experimental results. Finally, there is a validation of the resulting erosion pattern. Since there are no experimental studies which treat all these aspects in a detailed manner while having a Reynolds number and a Stokes number that are similar to the values occur-

ring in the impeller, two separate studies are used for this benchmark study. The fluid and particle flow fields are validated using the experiment by Miska [2008], whereas the validation of the resulting erosion pattern is performed using the research conducted by Wang et al. [2021].

5.1.1. Flow field validation

The first part of the benchmark study, the validation of the fluid and particle flow fields, is performed using an experimental study conducted by Miska [2008]. In this study, the mixture consists of water and aluminium particles. Since the density of the aluminium particles is the same as the density of sand ($\rho_p = 2650 \text{ kg/m}^3$), the flow behaviour of these particles is similar to that of sand particles. A schematic overview of the setup used in this study is shown in figure 5.1.

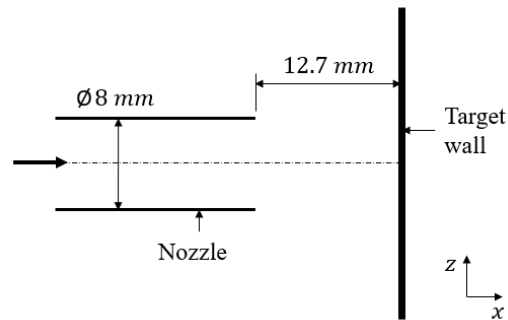


Figure 5.1: Experimental setup for the submerged impinging jet as used in the study of Miska [2008]. The mixture flows (from left to right) out of the round nozzle, after which it impinges on the target wall.

As can be seen in the figure, the slurry flows through a nozzle with a diameter of 8 mm before hitting a surface that is located 12.7 mm behind the nozzle exit. During the experiments, the flow rate was held constant at a value of $1.82 \text{ m}^3/\text{h}$. This results in a Reynolds number that is equal to 8.5×10^4 , which is sufficiently high to ensure a turbulent flow.

The computational domain that is obtained from the experimental setup in figure 5.1 is shown in figure 5.2.

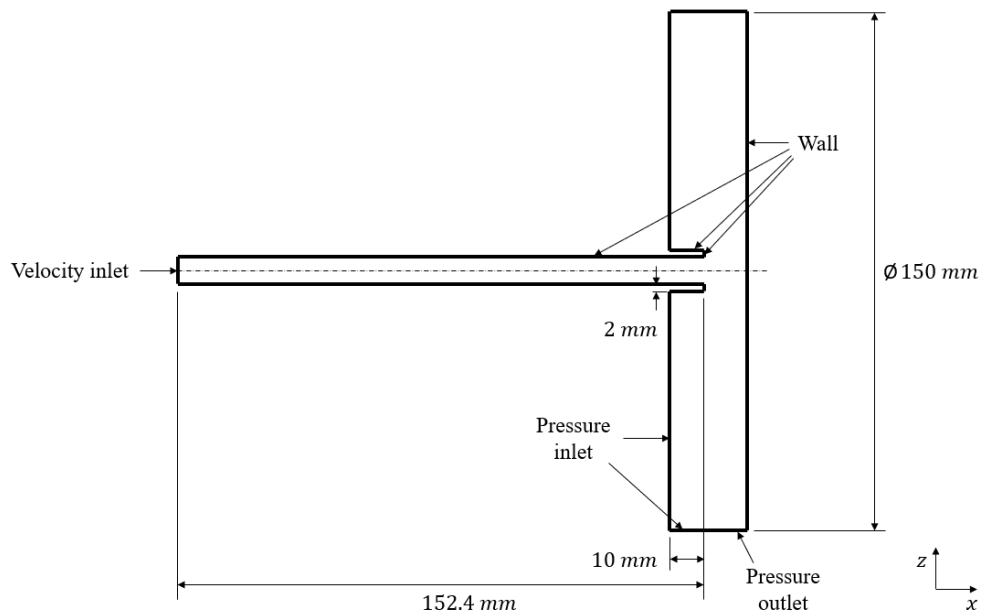


Figure 5.2: Cross-section of the computational domain for the flow field benchmark

For the length of the nozzle, a value of 152.4 mm is used, which was also used by Wang et al. [2021] in their numerical validation using the experiments by Miska [2008]. Later on in this section, it is shown that for this

nozzle length, the flow exiting the nozzle can be considered fully developed. The thickness of the nozzle was not specified by Miska [2008]. Therefore, a reasonable guess is used for this. The outside diameter of the domain and the distance between the pressure inlet and the wall are selected such that these boundaries do not have a large influence on the flow within the domain.

Since the flow rate through the nozzle is known, a constant velocity is specified at the inlet of the nozzle by using a "velocity inlet" boundary condition. The inner and outer sides of the nozzle, as well as the target surface are described by the "no-slip wall" boundary condition. The part of the outer diameter that is closest to the wall is defined as a "pressure outlet", whereas for the remaining sides of the domain the "pressure inlet" boundary condition is used to allow for entrainment.

In reality, there is the gravitational acceleration acting in the negative z-direction. Due to the small size of the domain and the relatively high velocity of the mixture, it is expected that the force due to the gravity is negligible. This assumption is verified for the particle flow field later on in this section.

For measuring the velocity field, the Laser Doppler Velocimetry (LDV) technique was adopted by Miska [2008]. In this technique two different laser beams are emitted that cross and form a fringe pattern at the desired measurement location. When particles move through this fringe pattern, light is scattered with oscillating intensity, which can be detected by an optical sensor. The frequency of the oscillation is related to the velocity of the particle. By analyzing the data obtained with the sensor, the average velocity of the particles can be extracted. This was done for both radial and axial directions at different locations behind the nozzle to obtain a two-dimensional velocity field.

In the thesis by Miska [2008], it is stated that the average velocity in the nozzle was equal to 10.5 m/s. Therefore, this value is used for the calculations that are discussed in this section. During the experiments however, the fluid velocity was controlled by setting the flow rate at 1.82 m³/h, which does not correspond to the specified average velocity. Since there are no visible differences between the numerically computed normalized velocity profiles for the two different inlet velocities, the normalization is also used to compare the numerical with the experimental velocities. In these cases, the average nozzle velocity is used to obtain the non-dimensional velocity.

Fluid flow field

For the fluid flow field measurements, particles with a mean diameter equal to 3 μm were added to the flow (Miska [2008]). Since this results in a Stokes number much smaller than 1, it can be assumed that the particles follow the fluid streamlines and therefore represent the fluid flow well. In addition, the volumetric concentration of the solid particles was equal to 0.03%. According to Andersson et al. [2012], for these conditions, it can be assumed that the solid particles do not alter the fluid flow.

The first step in the validation of the fluid flow field consists of a grid convergence study, which is discussed in the next paragraph. This is followed by a comparison between different turbulence models and wall treatments. In the final paragraph the choice of the nozzle length is verified.

Grid convergence study

In order to ensure that the discretization error is reasonably small, a grid convergence study has to be performed. For this, four different meshes are selected with the parameters that are shown in table 5.1.

Table 5.1: Grid parameters used in the grid convergence study for the flow field benchmark

Grid	Δx [mm]	First cell height [mm]	Number of cells [-]	$y_{\text{avg, nozzle}}^+$ [-]
Grid 1	2.34	0.97	3.16×10^4	235.3
Grid 2	1.55	0.64	1.09×10^5	162.5
Grid 3	0.81	0.32	7.69×10^5	82.9
Grid 4	0.42	0.16	5.37×10^6	41.3

In this table, also the resulting y^+ -value averaged over the nozzle surface is shown to give an indication of the mesh resolution within the boundary layers. As can be seen, for all the grids, the average y^+ at the nozzle is within the range where wall functions are applicable. Although resolving the grid near the wall is in general preferable, using wall functions is the only possibility since a more refined grid near the wall would result in cells that are smaller than the particle diameter.

The different grids used for the flow field study are shown in figure 5.3.

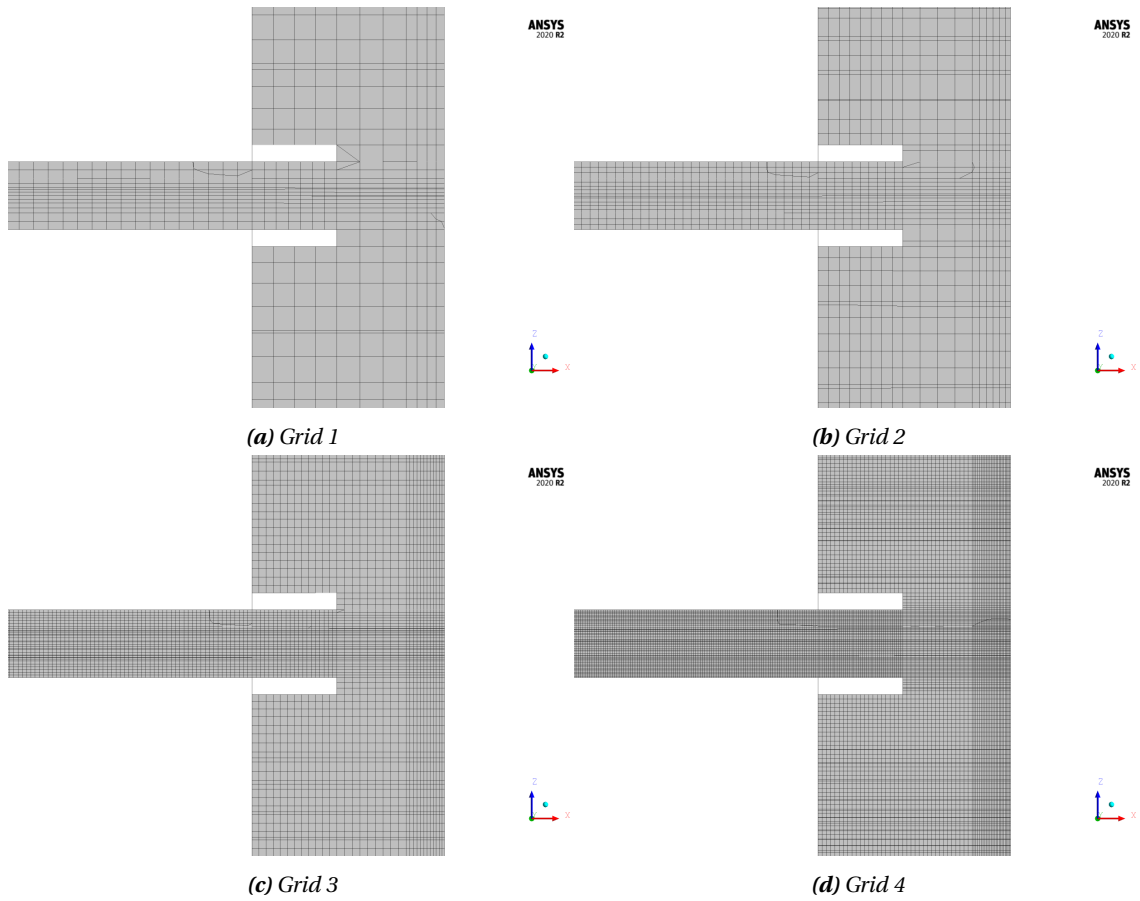


Figure 5.3: The grids used for validating the flow field, zoomed in at the nozzle exit region

For quantifying the grid convergence, the pressure averaged over the target surface is used as the scalar quantity. From this quantity, calculated for the three finest grids, an observed order of accuracy equal to 1.7 is found. This is illustrated in figure 5.4.

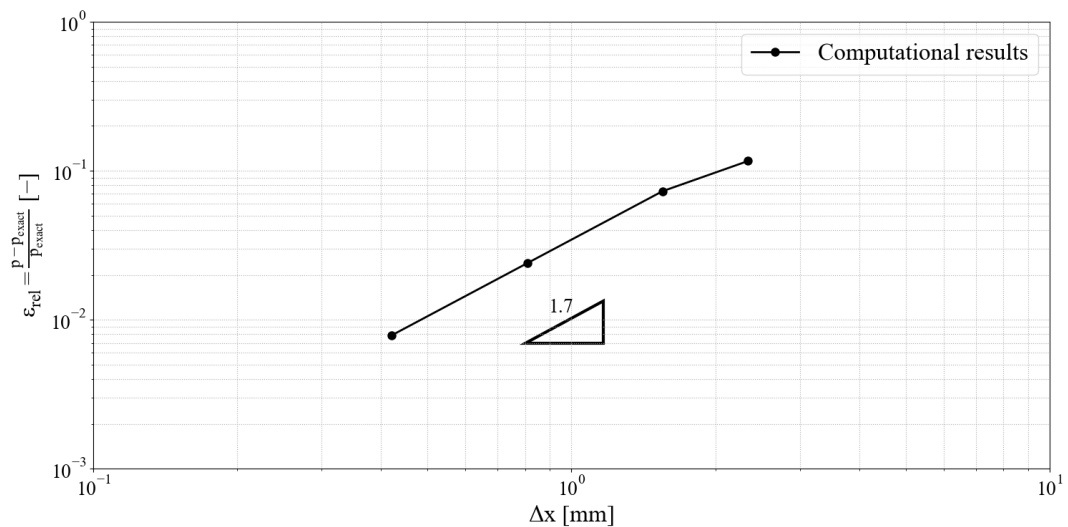


Figure 5.4: Relative error (based on the pressure averaged over the target surface) for the flow field benchmark as a function of the typical cell size of the grid. The triangle indicates the slope of the curve, which is equal to the observed order of accuracy for the three finest grids.

In this figure, ε_{rel} is the error ε divided by p_{exact} . The actual order of accuracy of the numerical model that is used is equal to 1. Since the observed order of accuracy is close to this value, it can be concluded that the three finest meshes are within (or at least close to) the asymptotic range.

In figure 5.5, the fluid flow fields as calculated with the four grids are compared with the experimental results of Miska [2008]. This is done using the velocity profiles at four different locations. Figure 5.5a shows the axial velocity field 1 mm downstream of the nozzle. In figure 5.5b, the axial velocity at the middle line is shown. Figures 5.5c and 5.5d show the radial velocity profile in line with the nozzle wall and 12 mm away from the symmetry axis, respectively.

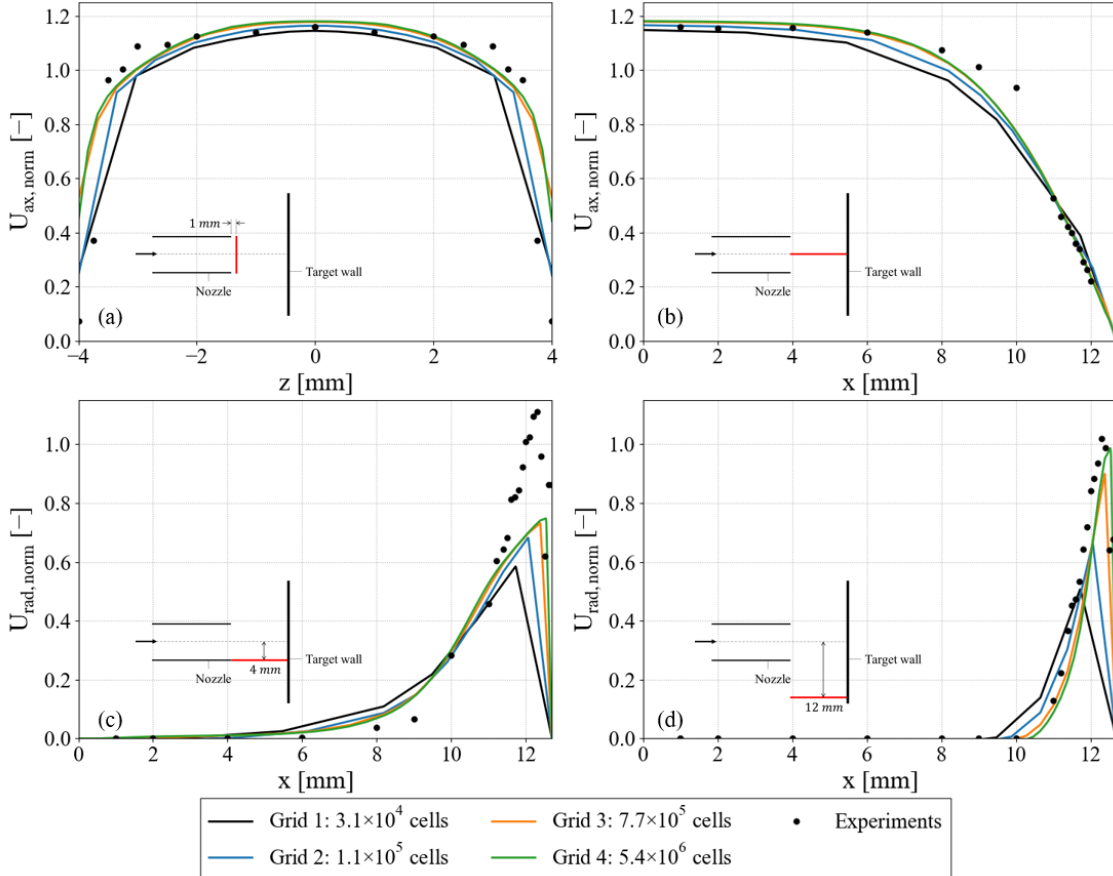


Figure 5.5: Comparison of the numerical results, as computed using different grids, with the experimental fluid velocity field for different profiles (experiments from Miska [2008]). The locations of the velocity profiles are indicated with the red lines.

In this figure, a clear convergence of the results in terms of grid size can be seen. While there is still a relatively large difference for the velocity profiles between grids 1, 2 and 3, that difference gets much smaller between grids 3 and 4. Considering this and the fact that the increase in computational effort is relatively large as compared to the increase in accuracy, it can be concluded that grid 3 is sufficiently refined for this case. Therefore, that grid is used for the comparisons in the following subsections.

When comparing the numerical to the experimental results, figures 5.5a and b show that the axial velocity in the middle of the jet is computed accurately. In addition, in figure 5.5d, it can be seen that the numerical radial velocity profile away from the centre of the domain is close to the experimental profile. On the other hand, directly behind the nozzle wall, the axial velocity is overpredicted, especially near the sides of the profile. In addition, in line with the nozzle wall, there is a noticeable difference between the numerical and experimental profiles for the radial velocity. This latter discrepancy may be due to the highly curved streamlines in that region (see figure 5.6).

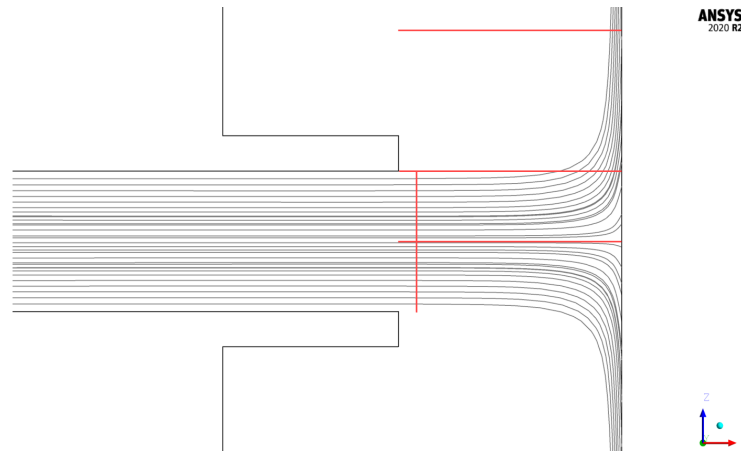


Figure 5.6: Fluid streamlines (grey) which exit the nozzle and impinge against the target surface. In this figure, the flow is from left to right. The black lines indicate the flow domain and the red lines represent the profiles at which the velocity is shown in the different figures in this section.

In this figure, the grey lines are the streamlines of the water and the red lines are the locations where the velocity profiles are extracted. As can be seen, for the profile directly in line with the nozzle wall, the streamline curvature is the relatively large. Since eddy viscosity turbulence models (including the $k-\omega$ SST model) assume isotropic turbulence (Davidson [2018]), these models are not able to accurately calculate the flow at that location.

Influence of turbulence model

In chapter 3, it is explained that the $k-\omega$ SST turbulence model is used for the simulations within this project. In order to verify this choice, the flow field is compared for different turbulence models. Since the studies by Wang and Wang [2012] and Ilker and Sorgun [2020] showed that both the $k-\omega$ SST and $k-\epsilon$ RNG turbulence models yield the best results for slurry flows as well as flows through centrifugal pumps, the $k-\epsilon$ RNG model is included in the comparison. In addition, a Reynolds Stress Model (RSM) is added, since these models are considered to be more accurate by regarding the turbulence as being anisotropic, in contrary to the Eddy Viscosity models (Hickel [2019]).

In figure 5.7, the different turbulence models are compared for two different velocity profiles, the axial velocity profile directly downstream the nozzle exit and the radial velocity profile located 12 mm away from the centerline. The other two profiles are omitted since the differences are hardly visible at those locations.

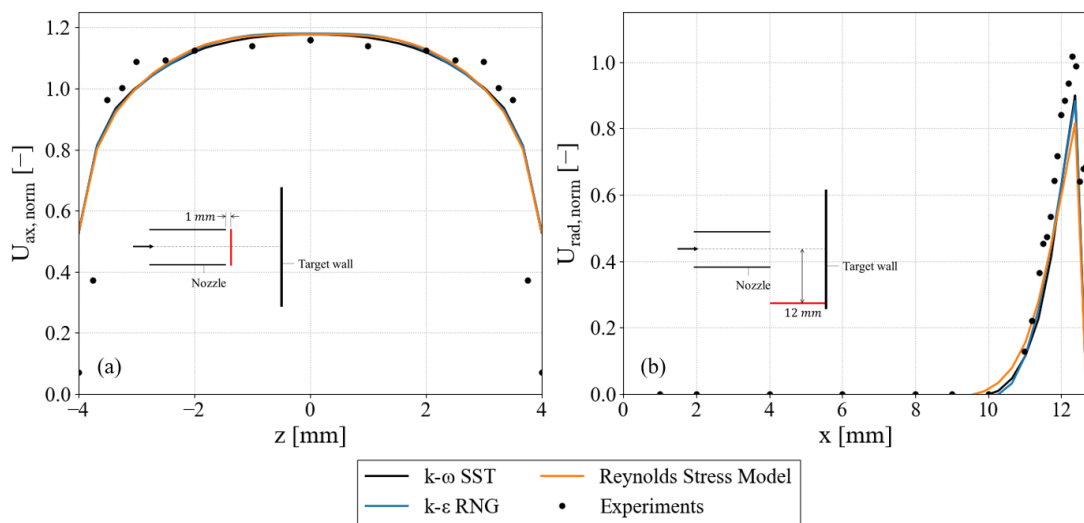


Figure 5.7: Comparison of the velocity profiles for different turbulence models (including the experiments from Miska [2008]). The locations of the velocity profiles are indicated with the red lines.

In this figure, it can be seen that the $k-\varepsilon$ RNG and $k-\omega$ SST turbulence models yield equally accurate results. This was also found by Wang et al. [2021] in their study with centrifugal pumps.

In addition, the results that are calculated using the Reynolds Stress Model are very close to the results of the aforementioned turbulence models. This means that this model does not accurately calculate the velocity at the location of the highly curved streamlines either. Although, according to Davidson [2018], RSM models are capable of dealing with highly curved flows, ANSYS, Inc. [2020a] shows that there are additional closure assumptions involved in the models. This may well be the reason that the Reynolds Stress Model does not yield more accurate results for this specific situation.

Influence of wall treatment

The second comparison that is of importance is that of the wall treatment. As explained in chapter 3, the flow in the boundary layer can either be resolved using the modified turbulence model or calculated by using wall functions. Since the smallest cell (and especially the first cell next to a wall) should be larger than the particle diameter, it is often required to use wall functions when dealing with liquid-particle flows. In figure 5.8, the two profiles that yield the largest differences for the two methods are shown to give an indication of the error involved when using wall functions for this situation. In both of these computations, the same grid is used for the regions far away from the wall. For the computation with wall functions, the resulting y^+ averaged over the nozzle surface is equal to 73, whereas a value of 0.72 is found in the computation where the boundary layer is resolved.

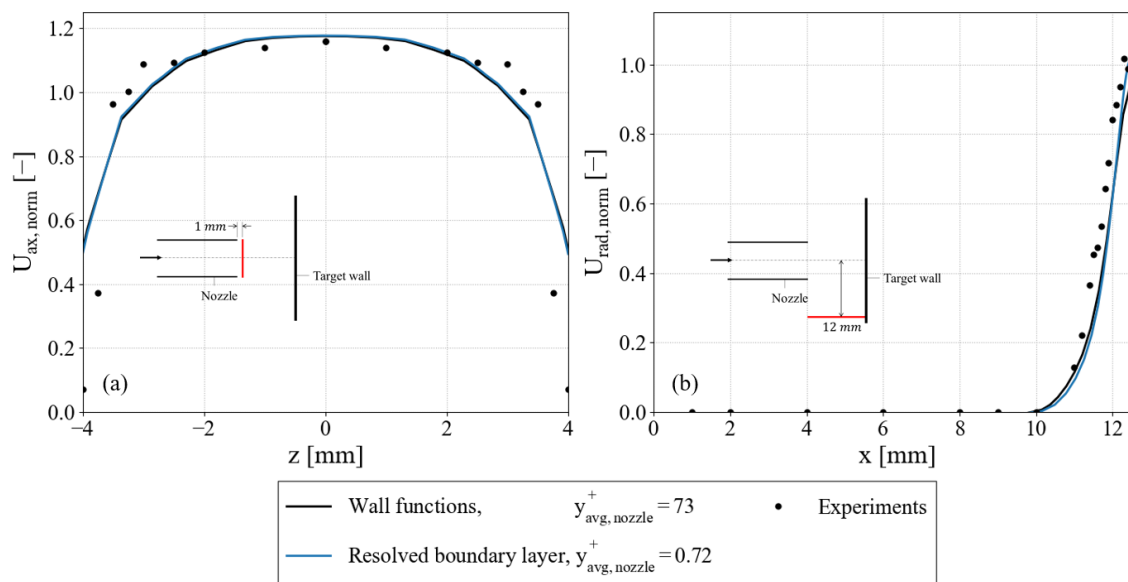


Figure 5.8: Comparison of the numerical results while using wall functions and resolving the boundary layer (including the results of the experiments by Miska [2008]). The locations of the velocity profiles are indicated with the red lines.

In the flow directly downstream the nozzle exit, there is hardly any difference visible in the velocity profiles calculated by using wall functions and resolving the boundary layer. This shows that the error at the sides of the profile is not introduced by the use of wall functions. In addition, there is only a small difference between the two velocity profiles away from the centre of the domain. Therefore, the use of wall functions is justified for the case of a submerged impinging jet.

Nozzle length

In numerical modeling, it is important to place the boundary conditions such that these do not introduce errors in the solution at the locations of interest. For the inlet of the numerical domain, this means that it should be placed such that the flow exiting the nozzle is fully developed. According to Çengel and Cimbala [2006], this means that the velocity profile is independent of the streamwise coordinate. Therefore, the same is true for the wall shear stress. In figure 5.9, the wall shear stress along the nozzle wall for a nozzle length of 238 mm is shown.

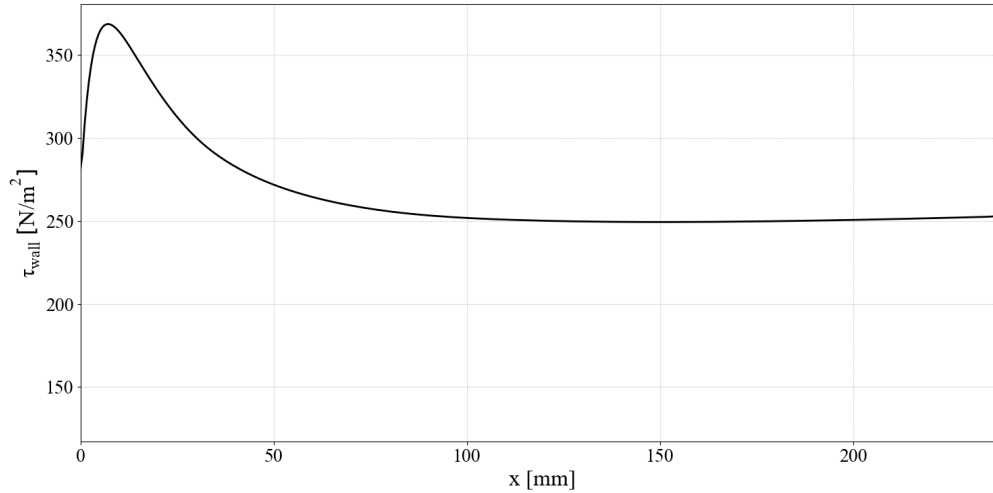


Figure 5.9: Wall shear stress as a function of the streamwise coordinate. The nozzle inlet is located at $x = 0$ mm, whereas the nozzle outlet can be found at $x = 238$ mm.

In this figure, it can be seen that after about 150 mm, the wall shear stress becomes more or less constant, which implies that after 150 mm, the flow can be considered fully developed. Close to the nozzle exit, there is a sudden drop in wall shear stress. This is due to the fact that at the exit itself, the fluid separates from the walls and flows into the open area.

To show that the nozzle length that is specified at the beginning of this section is sufficient, the resulting velocity profiles for two different nozzle lengths are compared in figure 5.10.

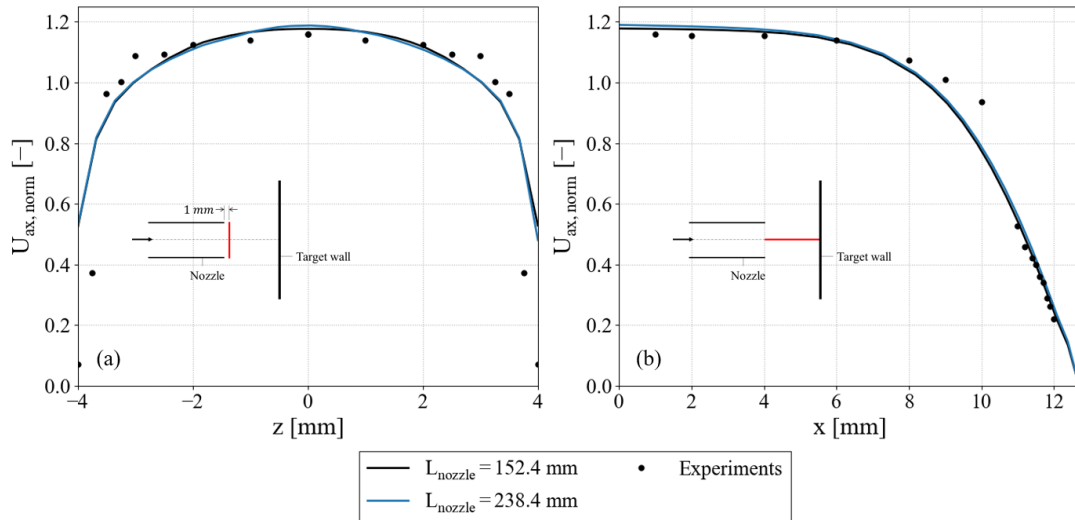


Figure 5.10: Comparison of the numerical results for two different nozzle lengths (including the results of the experiments by Miska [2008]). The locations of the velocity profiles are indicated with the red lines.

For both axial velocity profiles, there is hardly any visible difference when comparing the results from the computations with the two nozzle lengths. Since the differences for the radial velocity graphs are even smaller, these are omitted. Based on these results, it can be concluded that a length equal to 152.4 mm is sufficient.

Particle flow field

In the second phase of the experimental study by Miska [2008], the small particles were replaced by aluminium particles with a mean diameter of 120 μm . This results in a Stokes number equal to 2.66, which is sufficiently close to the value that is expected to occur in the impeller. In addition, the volumetric concentration of the solid particles is equal to 0.03%. Just like for the fluid flow field, the velocity of the particles was

measured using the LDV-setup that is described before.

In the first subsection, it is verified whether the grid convergence that is established for the fluid flow field is also valid for the particle flow field. This is followed by a comparison between the one-way, two-way and four-way coupling methods. Then, the influence of the gravitational acceleration is discussed. This section ends with an explanation of the influence of the particles on the water flow field and the slip velocity (the difference between the mixture and particle velocities).

Grid convergence study

As mentioned before, the first step in the validation of the particle flow field is to verify whether these results converge to a certain solution while refining the grid. To this end, in figure 5.11, the resulting particle velocity profiles are compared for the three finest grids.

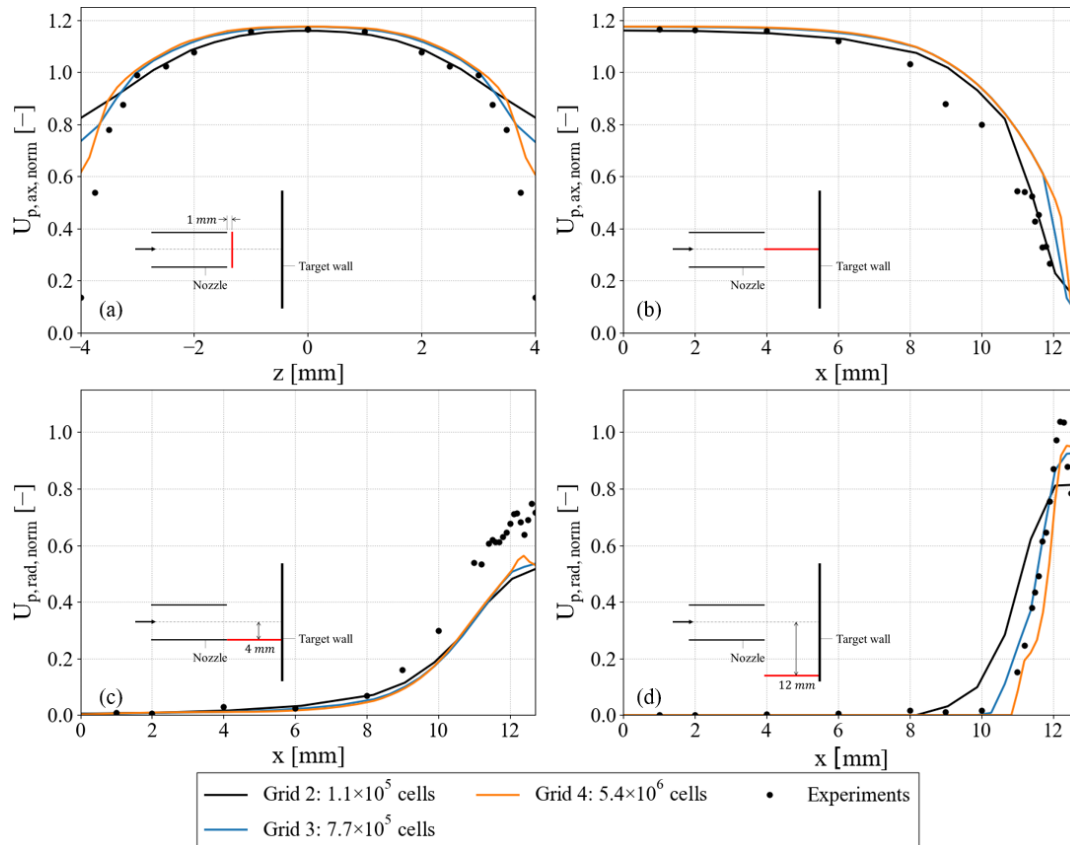


Figure 5.11: Comparison of the two-way coupled numerical results, as computed using different grids, with the experimental particle velocity field for different profiles (experiments from Miska [2008]). The locations of the velocity profiles are indicated with the red lines.

It can be seen that also for the particle velocities, a converged solution in terms of grid size can be found using the grids that are specified in table 5.1. Following the same argument used in the previous section, it is concluded that the third mesh is used for the different comparisons that follow in the upcoming subsections. When comparing the numerical to the experimental results, it turns out that the axial particle velocity is overpredicted by the numerical model. On the other hand, the radial particle velocity is underpredicted. This latter is probably caused by the same underprediction of the radial water velocity at those locations. Also in this case, the discrepancy in radial velocity becomes smaller with increasing distance from the centre of the domain.

An interesting aspect of particle flow that can be noticed in figure 5.11 is the fact that the particle velocity does not necessarily go to zero close to the wall, whereas this is the case for the fluid in which the particles are transported. This is especially true in the flow over the target surface (figures 5.11c and d). According to Capecepatro and Desjardins [2013], this is due to the fact that the particles maintain their inertia close to the walls. On the other hand, the fluid is slowed down by viscous effects (the no-slip condition).

Comparison of coupling methods

It is explained before that there are three different types of interaction modeling. For one-way coupling, only the influence of the water on the particles is taken into account. When using two-way coupling, the influence of the particles on the water is computed as well. The most inclusive method, four-way coupling, also includes the collisions between different particles. In order to investigate the influence of these different method applied to the impinging jet, the results for these methods are displayed in figure 5.12. In this figure, the two profiles with the smallest differences between the three methods are omitted.

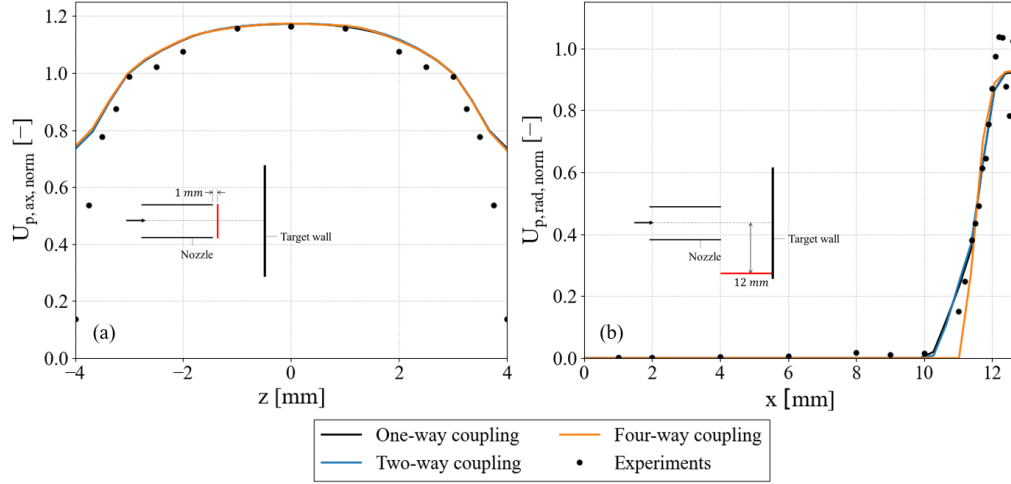


Figure 5.12: Comparison of the numerical results for the different coupling methods (including the results of the experiments by Miska [2008]). The locations of the velocity profiles are indicated with the red lines.

It can be noted is that there is no visible difference between the results calculated by the one-way and two-way coupled methods. In addition, for the first profile, the differences between the two-way and four-way coupled are negligible. These small differences are due to the low volumetric concentration of the particles, which implies that the influence of the particles on the water and of the particle-particle collisions are small. For the radial velocity profile away from the centre of the jet (figure 5.12b), there is a slight difference between the two-way and four-way coupled results.

It can be seen in figure 5.12b that when the collisions are included in the computation (four-way coupling), the particles tend to stick closer to the wall as compared to the case where the collisions (two-way coupling) are not included. This difference between two-way and four-way coupling was also observed by Geurts and Vreman [2006] and Vreman et al. [2009], where an LES computation of a gas-solid channel flow was used to investigate the effect of inter-particle collisions. They found that, for a Stokes number somewhat larger than used in the current project, the turbophoresis effect is less pronounced when the particle collisions are neglected. According to Schlatter et al. [2012], the turbophoresis effect causes the particles to move from regions with high turbulence intensity to regions with low turbulence intensity. For wall-bounded flows, this implies that the particles accumulate in regions near solid walls. Therefore, neglectation of the inter-particle collisions leads to an underprediction of the particle accumulation near the solid walls.

It should be noted that it depends on the exact values of the collision model parameters to what extend the turbophoresis effect is enhanced by the inter-particle collisions. This is demonstrated in section 5.1.2.

Influence of gravitational acceleration

As indicated before, during the experiment, the impinging jet was oriented in such way that the gravitational acceleration acted in the negative z -direction. By executing one simulation with gravity turned and one with gravity turned off, it was found that there is no visible difference in particle velocity fields for those two cases. This can be explained by looking at the densimetric Froude number for this specific situation:

$$Fr = \frac{\rho_f U^2}{(\rho_p - \rho_f) g D} = 776.2 \quad (5.1)$$

Since this characteristic number is defined as the ratio of the inertial and gravitational forces, a value of 776.2 indicates that the inertial forces are much higher than the gravitational forces. The latter therefore have a

negligible effect on the (particle) velocity field.

Influence of the particles on the water flow field

In some situations, the particles have a large influence on the flow of the water. This is for instance the case when the volume fraction of the particles is large. By comparing the water velocity fields as calculated with the one-way coupled and two-way coupled computations, it can be found to what extent the water velocity field is influenced by the particles.

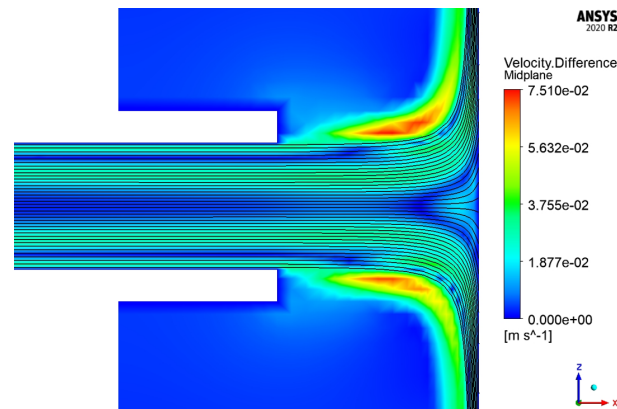


Figure 5.13: Contour plot of the difference in water velocity magnitude with and without sand particles in the flow. For the former, the two-way coupled method is used. In this figure, the flow is from left to right.

For this situation, the difference in velocity between the two computations is rather small, considering the fact that the average particle velocity in the nozzle is equal to 10.5 m/s . This is because, as explained before, the volumetric concentration of the particles is low.

The maximum differences occurs just outside the jet stream. At that location, the water flows faster with particles than without them, which indicates that the jet becomes wider when particles are included. In addition, the water close to the nozzle wall is accelerated due to the particles, since these have a much smaller velocity gradient normal to the wall. This acceleration of the water is compensated in the middle of the domain, where the water is decelerated.

Slip velocity

Besides the influence of the particles on the water flow field, it is interesting to look at the difference between the mixture and particle velocities, the slip velocity. This slip velocity indicates to what extent the particles follow the water streamlines. Figure 5.14 shows a contourplot at the midplane of the domain with this quantity.

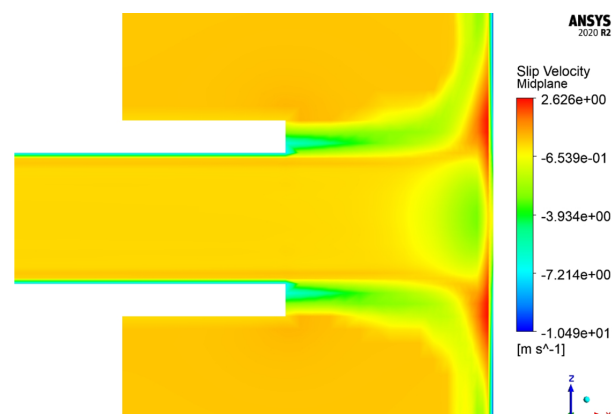


Figure 5.14: Contour plot of the slip velocity, which is defined as the difference between the velocity of the mixture and the velocity of the particles. For the latter, the two-way coupled method is used. In this figure, the flow is from left to right.

In the middle of the jet, the slip velocity is almost equal to zero, indicating that the particles flow with the same speed as the water. As explained before, close to the nozzle walls and the target surface, a negative slip velocity is calculated. Although this negative slip velocity was also measured by Miska [2008], the numerical method tends to overpredict the magnitude of the slip velocity at this location.

When moving closer to the target surface in the centre region of the jet, the slip velocity becomes negative. This is due to the inertia of the particles, which prevents them from decelerating as fast as the water close to the stagnation point. The positive slip velocity close to this region (the red areas) is caused by particles that bounce off the walls, resulting in a net average particle velocity that is smaller than the fluid velocity.

5.1.2. Erosion validation

In the second part of the benchmark study, the numerical erosion is compared to the results of an experiment conducted by Wang et al. [2021]. As can be seen in figure 5.15, the setup used during these experiments was slightly different from the setup used by Miska [2008]. In the experiments by Wang et al. [2021], the nozzle had a diameter of 6.8 mm and was oriented such that the flow was aligned with the gravitational acceleration. The effect of the gravity however, can be considered negligible, since the densimetric Froude number of this flow is equal to 1780.

The mixture had a velocity equal to 14 m/s and consisted of water and sand particles with a diameter of 80.5 μm . The volumetric concentration of these solid particles was 1%. Using these conditions, a Stokes number equal to 1.96 and a Reynolds number equal to 9.5×10^4 can be found. Therefore, both the fluid and particle flow are in the same regime as in the case of the flow through the impeller.

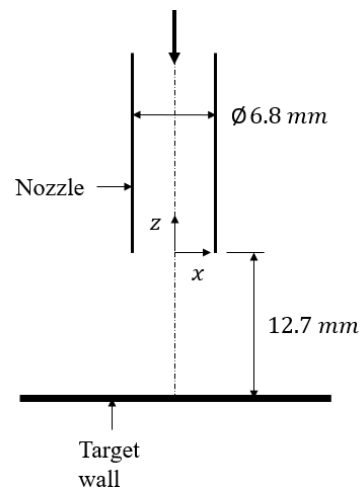


Figure 5.15: Experimental setup for the submerged impinging jet as used in the study of Wang et al. [2021]. The mixture flows (from top to bottom) out of the round nozzle, after which it impinges on the target wall.

During the experiments, Wang et al. [2021] used a target surface made of stainless steel 316. This material has a density of 7980 kg/m^3 . For the numerical computations, a hardness equal to 1.795 GPa is used for this material (value taken from M. Woite [2012]).

The domain for this benchmark study is very similar to the domain that is shown in figure 5.2. The length of the nozzle is again equal to 152.4 mm. For this length, a fully developed flow is obtained at the nozzle exit, which is confirmed in the same way as for the flow field benchmark in the previous section. In addition, the thickness of the nozzle, the height of the lower portion of the domain and the outer diameter of the domain are the same as for the flow field benchmark.

Since the current setup is slightly different from the setup used for the flow field validation in the previous section, a new grid convergence study is performed. That study is discussed in the next paragraph. This is followed by a comparison of the different coupling methods and the different erosion models.

Grid convergence study

For the grid convergence study of the erosion benchmark, four different grids are used. The parameters for setting up these grids and the resulting y^+ values averaged over the nozzle wall can be found in table 5.2.

Table 5.2: Grid parameters used in the grid convergence study for the erosion benchmark

Grid	Δx [mm]	First cell height [mm]	Number of cells [-]	$y_{\text{avg.nozzle}}^+$ [-]
Grid 1	1.25	0.29	1.90×10^5	98.5
Grid 2	0.87	0.19	5.74×10^5	62.9
Grid 3	0.65	0.14	1.34×10^6	46.9
Grid 4	0.45	0.094	4.01×10^6	31.0

Also in this case, the y^+ -values for the different grids imply that wall functions are used for the flow near the wall.

In figure 5.16 the relative error is displayed as a function of the typical cell size in a log-log plot to show the observed order of accuracy. For the calculation of the relative error, the pressure averaged over the target surface is utilized.

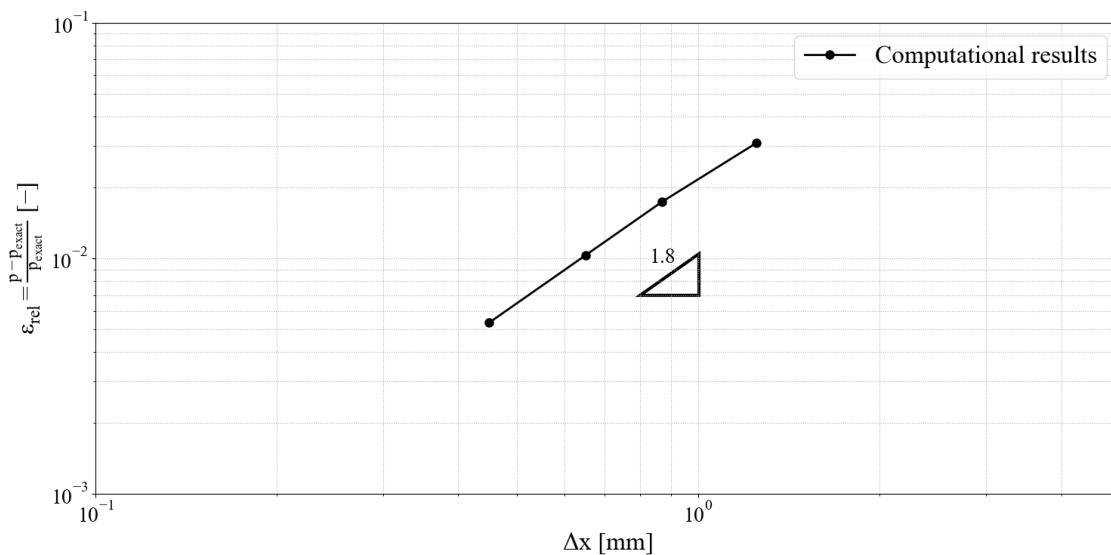


Figure 5.16: Relative error (based on the pressure averaged over the target surface) for the erosion benchmark as a function of the typical cell size of the grid. The triangle indicates the slope of the curve, which is equal to the observed order of accuracy for the three finest grids.

The resulting observed order of accuracy is very close to the value that was found for the flow field benchmark. In addition, it is close enough to the actual order of accuracy (which is equal to 1) to be able to conclude that the results of all four grids are within the asymptotic range. This order of accuracy also implies that the results that are calculated using the grids that are specified in table 5.2 are converging to a certain result, which is demonstrated for the erosion at the target surface in figure 5.17. Here, $x = 0$ refers to the middle of the domain, which means that only one side of the erosion profile at the target surface is shown. The result of the first grid is omitted in this graph, since the error introduced in that calculation is too large, which would have resulted in a loss of detail in the graph.

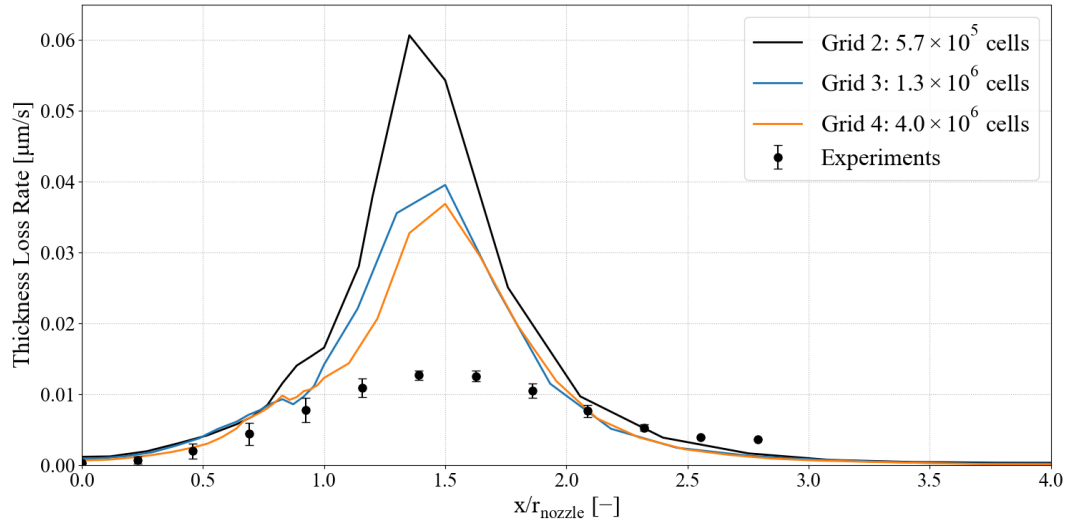


Figure 5.17: Comparison of the erosion profile, as computed using the two-way coupled method for different grids, with the experimental erosion profile at the target surface (experiments from Miska [2008]). The middle of the domain is located at $x/r_{\text{nozzle}} = 0$.

The erosion is quantified in terms of the thickness loss rate in $[\mu\text{m/s}]$. For this, the numerical results (quantified in terms of the erosion rate density in $[\text{kg}/\text{m}^2\text{s}]$) are divided by the density of the target material. This method was proposed by Graham et al. [2010]. The x-coordinate is non-dimensionalized by using the radius of the nozzle. The differences between grids 3 and 4 are much smaller than those between grids 2 and 3. Since the increase in computational effort of grid 4 with respect to grid 3 is considerable, grid 3 is considered to be sufficiently refined. Therefore, this grid is used for the comparisons in the following paragraphs.

The minimum amount of erosion (from the points that are measured during the experiment) can be found directly in line with the centre-line of the nozzle. This is due to the particle velocity being (almost) equal to zero as was also demonstrated for the flow field benchmark in the previous section. In addition, for stainless steel, the erosion is smaller for normal impacts than for impacts with an angle between 20 and 60 degrees (see figure 3.6). When moving away from the centre of the target surface, the erosion rate increases until it reaches its peak around $x = 1.5 \times r_{\text{nozzle}}$. This implies that the erosion peak occurs outside the nozzle diameter projected on the target surface. The occurrence of the erosion peak at that location can be explained by looking at the numerical volume fraction contour at the plane in the middle of the domain.

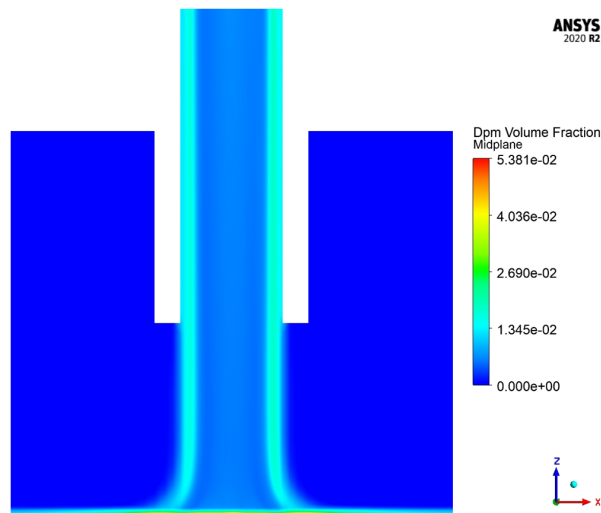


Figure 5.18: Contour of the volume fraction around the nozzle exit, computed with the two-way coupled numerical method. In this figure, the flow is from top to bottom.

Within the nozzle, the particles tend to move towards the wall due to the turbophoresis effect (as explained in the previous section), resulting in a higher volume fraction near the walls than in the centre of the nozzle. After exiting the nozzle, the particles near the nozzle walls spread out slightly due to the streamline curvature close the target surface. This explains the presence of the erosion peak on the target surface just outside the radius of the nozzle.

When comparing the numerical and experimental results, a few remarkable points can be observed. The first is that the numerical erosion rate at the centre of the target surface is in good agreement with the experimental values. In addition, the location of the erosion peak is predicted well by the two-way coupled numerical model. On the other hand however, the magnitude of the erosion peak is largely overpredicted. One explanation for this difference would be that the hardness that is specified in the computation does not correspond to the hardness of the actual material that was used during the experiments. For the specific type of stainless steel that was used by Wang et al. [2021], hardness values as high as 3.687 GPa can be found (RGPBALLS Srl [n.d.]). In figure 5.19, the resulting erosion profile for this hardness is compared to the erosion profile obtained with a hardness equal to 1.795 GPa.

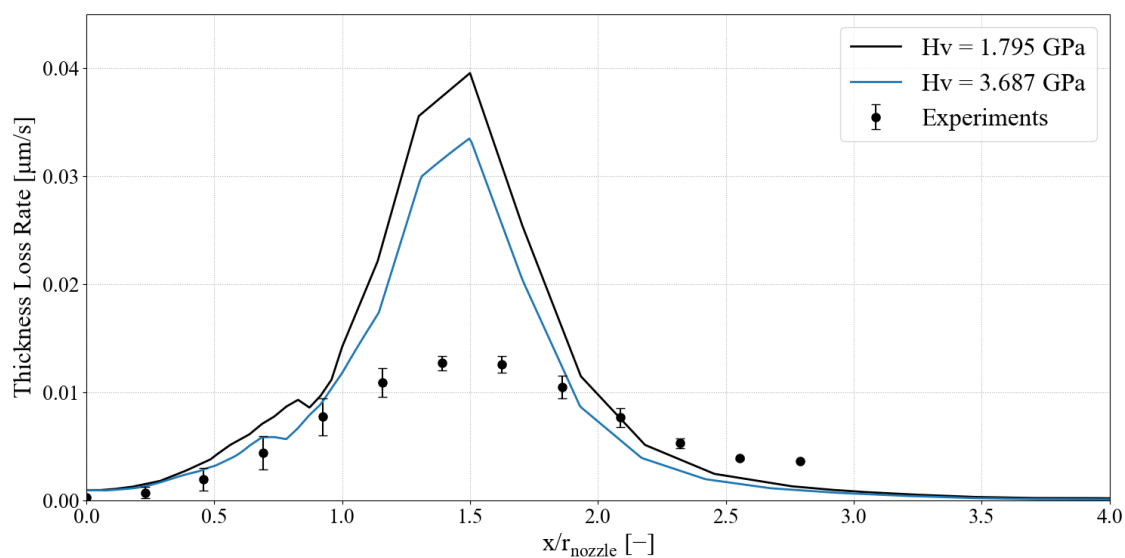


Figure 5.19: Comparison of the erosion results, as computed using the two-way coupled method for different values for the hardness (including the results of the experiments by Miska [2008]). The middle of the domain is located at $x/r_{\text{nozzle}} = 0$.

Although the larger hardness still involves a certain error, changing the hardness does have a significant effect. From this, it can be concluded that for accurate erosion predictions, it is important to have the actual material properties available.

Another possible explanation for the overprediction of the erosion peak is that the $k-\omega$ SST turbulence model is not capable of dealing with large streamline curvature, while the erosion peak is located at the region where those streamlines impact the surface. As demonstrated in the previous section, this leads to an underprediction of the radial particle velocity near the location of the erosion peak. Since this would also imply an increase in the angle of impact, this may well lead to an overprediction of the erosion rate.

A second difference between the numerical and experimental results can be seen in the erosion farther away from the centre of the domain. Here, the erosion is underpredicted by the numerical model.

Coupling

Since the volumetric concentration of the sand particles is equal to 1% in this problem, it is advised by Andersson et al. [2012] to use a four-way coupled solver. This is due to the fact that the inter-particle collisions become relevant for this concentration. In addition, the influence of the particles on the water flow field is expected to be significant in this situation. In figure 5.20, the erosion profiles for the different coupling methods are compared. In addition, to illustrate the dependency of the four-way coupled method on the parameters of the collision model, the resulting profile for this method is shown for two different values of the static friction coefficient μ_s .

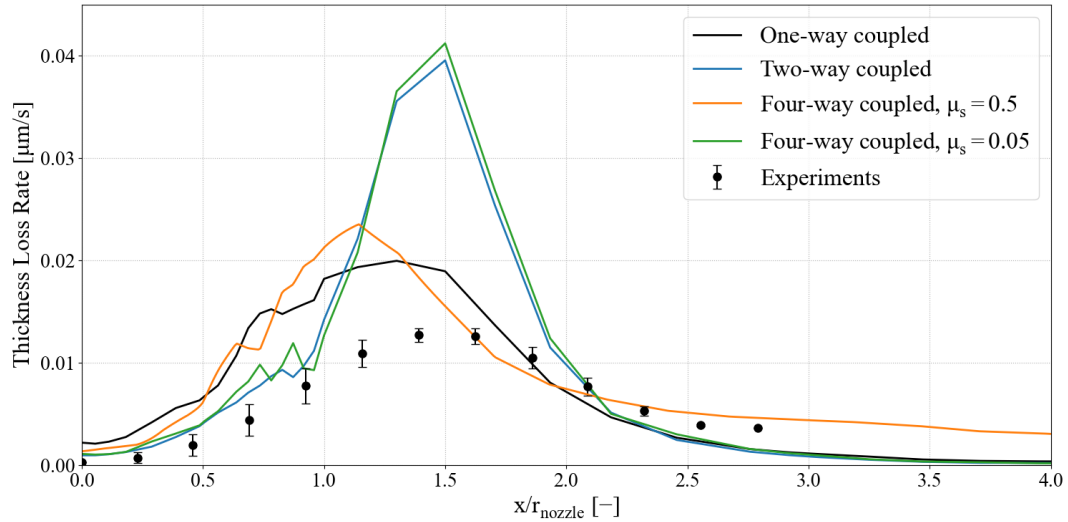


Figure 5.20: Comparison of the erosion results using the different coupling methods (including the results of the experiments by Miska [2008]). The middle of the domain is located at $x/r_{nozzle} = 0$.

It can be seen that there is a large difference between the two profiles that are computed using the four-way coupled method. While the profile for $\mu_s = 0.5$ is closer to the one-way coupled result, the profile for $\mu_s = 0.05$ is similar to the profile that is computed with the two-way coupled solver. This large difference can be attributed to the loss in kinetic energy of the particles due to the friction: for a higher friction coefficient, the velocity of the particles near the wall decreases considerably as compared to the situation with a small friction coefficient. In addition to a higher volume fraction close to the wall for the large friction coefficient, this results in the particles being spread out when exiting the nozzle. Therefore, also the erosion profile is more smoothed in that case with a lower magnitude for the erosion peak and more erosion farther away from the centre of the domain.

From this discussion, it can be concluded that, for the four-way coupled method, there is a large dependency of the erosion profile on the specific values of the collision model. Therefore, in order for the four-way coupled solver to be accurate, the exact values of the parameters from this collision model should be obtained (either from literature or from conducted experiments).

The differences between the erosion profiles as computed by the one-way coupled and two-way coupled methods can be explained by looking at the volume fraction in the middle of the domain.

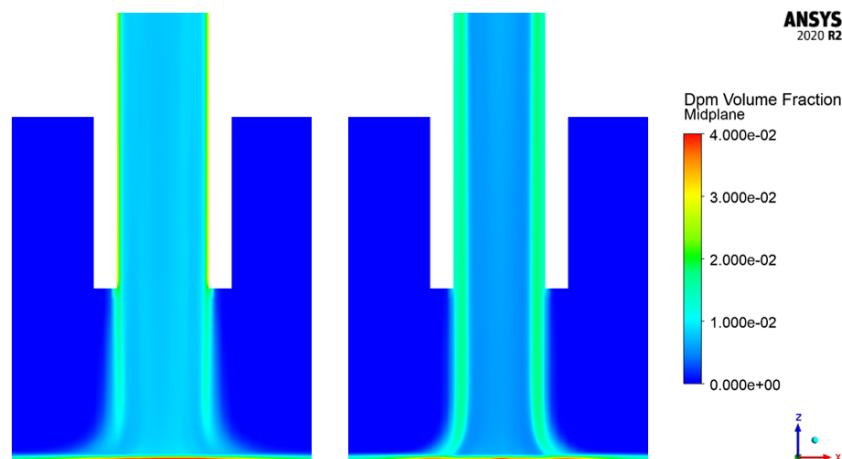


Figure 5.21: Contour of the volume fraction around the nozzle exit for a one-way coupled (left) and a two-way coupled (right) computation. In this figure, the flow is from top to bottom.

Figure 5.21 shows that the particles accumulate more towards the wall in the case of the two-way coupled

result. Due to the volume fraction peak near the walls, many particles follow the outer streamlines of the jet after which these hit the target surface outside the nozzle radius. In the one-way coupling situation, the particles are distributed more evenly. This results in a more smoothed erosion profile at the wall and an erosion peak closer to the middle of the domain.

Erosion model

Besides the Oka model, there are many other erosion models that are commonly used. These models are all developed for a certain application and therefore often limited to situations that are comparable to the conditions used during the development of the model. To verify the choice of the Oka erosion model for this specific situation, a comparison is performed in this paragraph. This comparison includes the E/CRC erosion model, which is considered to have a similar performance as the Oka model (Zhang et al. [2007]). In addition, the Finnie erosion model is included since this model is often used in literature. For the exact formulation of these models, the reader is referred to Zhang et al. [2007] and Finnie [1960], respectively.

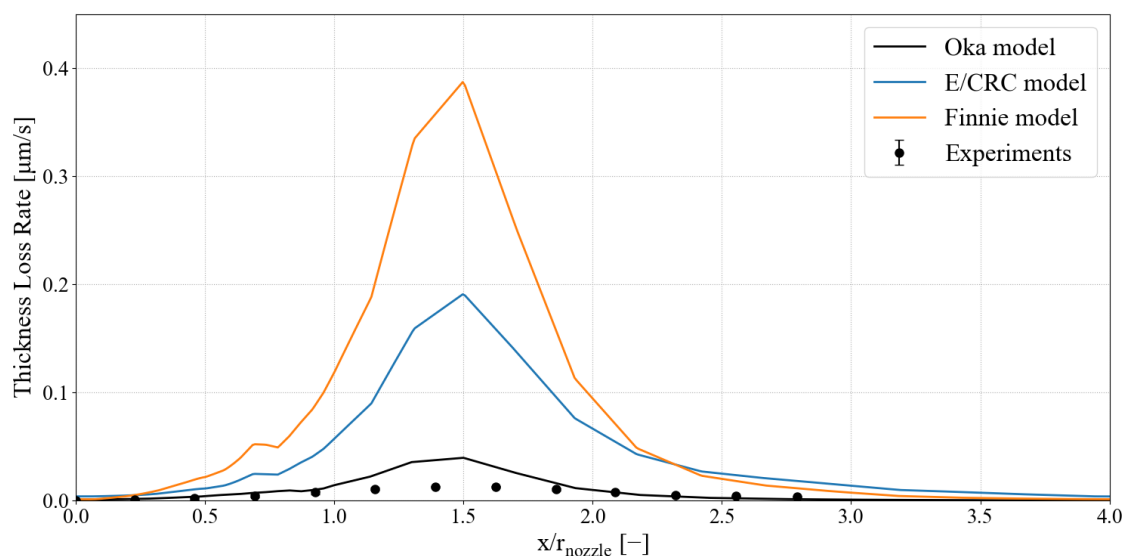


Figure 5.22: Comparison of the erosion results, as computed using the two-way coupled method in combination with different erosion models (including the results of the experiments by Miska [2008]). The middle of the domain is located at $x/r_{nozzle} = 0$.

When qualitatively comparing the erosion profiles calculated with the different erosion models, a few similarities can be observed. For all the profiles (including the experimental profile), the erosion is the smallest in the middle of the target surface. Then, the erosion rate increases until it reaches its peak around $x = 1.5 \times r_{nozzle}$. This location is predicted well by all the considered erosion models. After this peak, the erosion rate reduces to zero with increasing distance from the centre of the domain.

Quantitatively however, there are large differences between the results. This has something to do with the information that is available for the different erosion models. Since no experimental data on the usage of the Finnie model in combination with stainless steel walls could be found, the parameters for carbon steel walls are used. This is one reason for the large deviation of the Finnie model with respect to the experimental values. In addition, the Finnie model does not take into account the size and shape of the solid particles. This introduces additional uncertainties in the model.

For the E/CRC model, a similar reasoning can be given as for the Finnie model. Zhang et al. [2007] showed that the parameters that are used in the E/CRC model were developed with experimental data using the material Inconel 718. Also for this model, no experimental data are available for solid particles impacting stainless steel walls. In addition, although the E/CRC model does take into account the shape of the particles, the diameter of the particles is not included in the model.

5.2. Verification impeller model

In this section, the numerical model applied to the impeller is verified. For this, the computational domain is used that is displayed in figure 5.23. The pipe is shortened considerably in this figure in order to improve the visibility of the different parts of the domain.

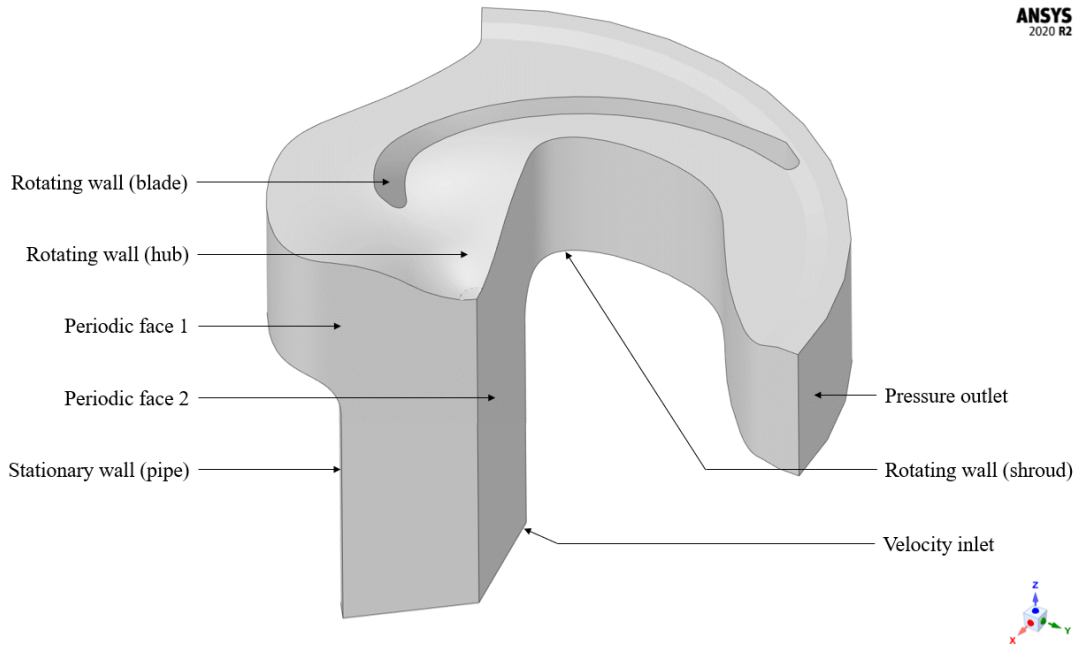


Figure 5.23: Numerical domain for the impeller computations. In this figure, the pipe is shortened to ensure a good visibility.

By making use of the symmetry within the impeller, only one of the three blades is included. To this end, two periodic faces are defined with a rotational symmetry boundary condition. The domain contains four different walls, the hub, the shroud, the blade and the pipe (all walls are defined with the no-slip condition). In addition, the flow enters the pipe through a velocity inlet condition and exits the impeller via a pressure outlet. Although in reality, the pressure at the outlet varies, in this model, it is assumed to be constant. To simulate the rotation of the impeller while treating the fluid phase as being steady, a frame motion is applied to the domain. In addition, the impeller walls rotate with the same rotational velocity as the domain. By keeping the rotational velocity of the pipe wall equal to zero, a straight flow is ensured in that section of the domain. The domain is oriented in the same way as during the experiment. This means that the gravitational acceleration acts in the negative z-direction.

The conditions that are used for the numerical computations are equal to the experimental conditions averaged over the experimental time. These are listed in table 5.3.

Table 5.3: Physical parameters used for the impeller simulations

Parameter	U_{in} [m/s]	ρ_f [kg/m ³]	ρ_p [kg/m ³]	d_p [mm]	C_{vs} [%]	Ω [rad/s]
Value	4.301	998.2	2650	0.619	9.95	62.48

The inlet velocity that is mentioned in this table is the velocity of the mixture. This implies that the value specified here is used for both the fluid phase as well as the solid phase. In addition, Ω is the rotational velocity of the impeller, used for defining the frame and wall motions.

In the first paragraph, the choice for the domain size is substantiated. This is followed by a description of the grid convergence study that is performed for the impeller. Finally, the influence of the coupling method and erosion model on the erosion profile are investigated.

The exact settings that are used within Fluent for the computations that are described in this section can be found in appendix B.

Domain size

In figure 5.23, two non-physical boundaries are visible. Therefore, these boundaries should be placed such that there is only a small influence on the solution in the region of interest. For the outlet of the impeller, this is difficult choice, since in reality, there is the volute casing close to this region. Therefore, the boundary cannot be placed in the freestream where the disturbances from the impeller are negligible. Gülich [2020] recommended the use of the following equation to determine the position of the interface between the impeller and volute zones in the case that the volute is included:

$$\frac{r_{interface}}{r_2} = \left(\frac{d_3}{d_2}\right)^{0.5} \quad (5.2)$$

In this equation, the subscript 2 refers to the trailing edge of the impeller blades, while the subscript 3 is used for the volute cutwater. Since the volute is not included in this study, the impeller outlet is placed at the location of the interface between the impeller and the volute.

For the length of the inlet pipe, it is important that the flow is fully developed when entering the impeller, since in that case, the solution is not dependent anymore on the turbulence inlet conditions. For finding the optimal pipe length, the approach is used that is described in section 5.1.1. It is found that after 5.5 *m*, the wall shear stress reaches a constant value. Therefore, this pipe length is used for the simulations in this section.

Grid convergence study

For the grid convergence study, three different grids are constructed which are as geometrically similar as possible. For this, the parameters that are listed in table 5.4 are used.

Table 5.4: Grid parameters used in the grid convergence study for the impeller

Grid	Δx [mm]	First cell height blade [mm]	Number of cells [-]	$y_{avg,blade}^+$ [-]
Grid 1	5.17	1.57	8.48×10^5	132.5
Grid 2	3.76	1.10	2.19×10^6	77.6
Grid 3	3.02	0.85	4.26×10^6	53.0

It can be seen that for all three grids, the first cell height is larger than the particle diameter that is used in the computations. This results in a y^+ -value for all three grids within the range of the applicability of wall functions. Although flow separation is expected to occur from the impeller blades, it is not possible to refine the near-wall region further, since this would compromise the computations of the particle paths.

In figure 5.24, the different grids around the impeller blades on a *y-z* plane are displayed.

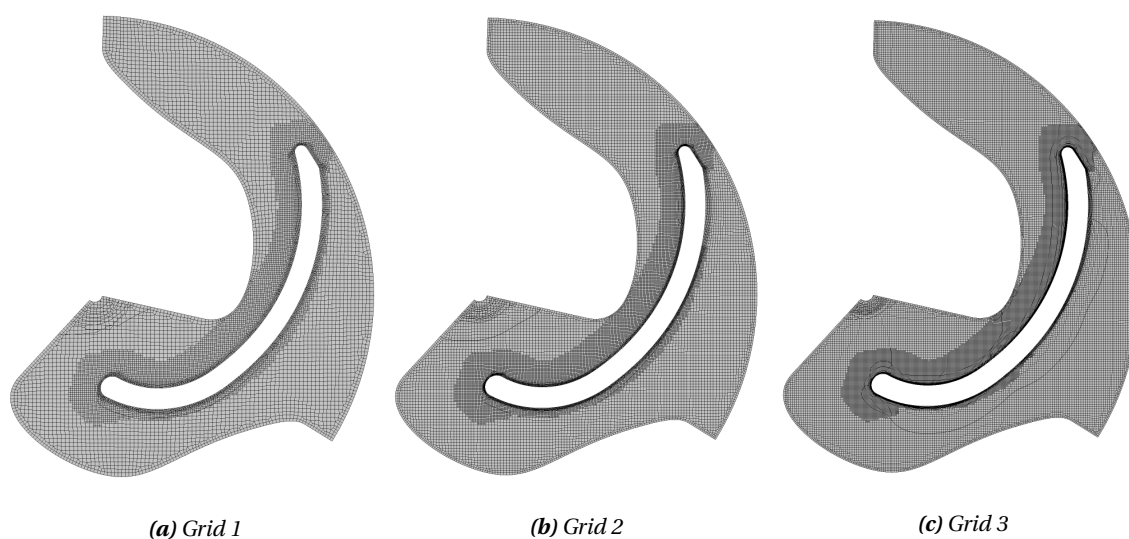


Figure 5.24: Cross-section of the different grids that are used for the impeller grid convergence study

For the quantification of the grid convergence, the head of the pump can be used. As explained in chapter 2, this quantity is the total pressure difference between the outlet and the inlet of the impeller. The resulting relative error is displayed as a function of the typical cell size in figure 5.25. Since the convergence of computations on the two finest grids is such that there is still a variation in head of about 1%, the head that is used to calculate the relative error is averaged over the last 200 iterations. Therefore, there is still an uncertainty in the observed order of accuracy that is displayed in the graph.

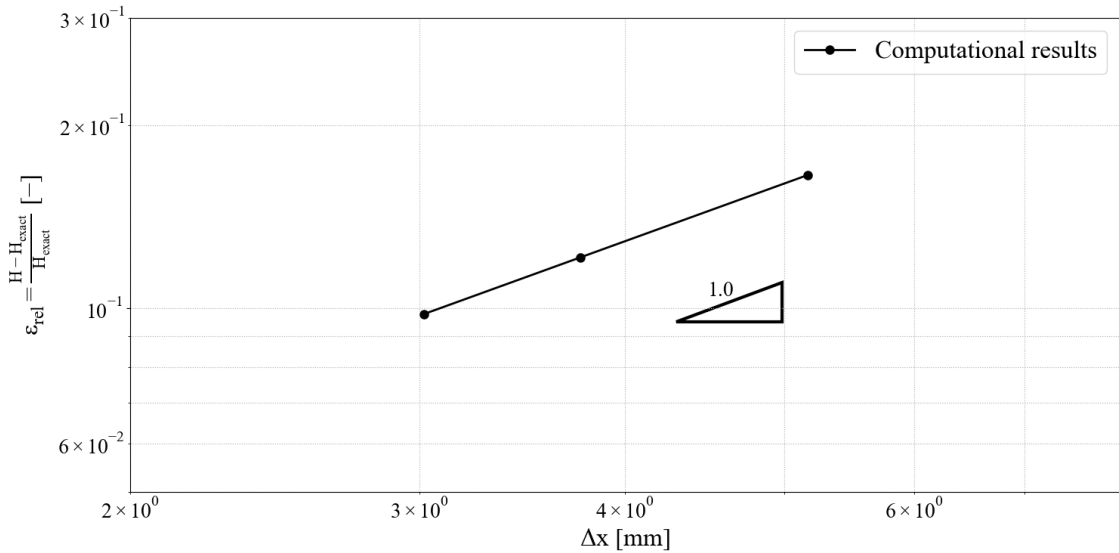


Figure 5.25: Relative error (based on the head) for the impeller computation as a function of the typical cell size of the grid. The triangle indicates the slope of the curve, which is equal to the observed order of accuracy.

Although the relative error for the finest grid is still around 10%, the observed order of accuracy of 1.0 indicates that the grids are within the asymptotic range. In order to verify the grid convergence on a local scale, the pressure along the blade is shown in figure 5.26.

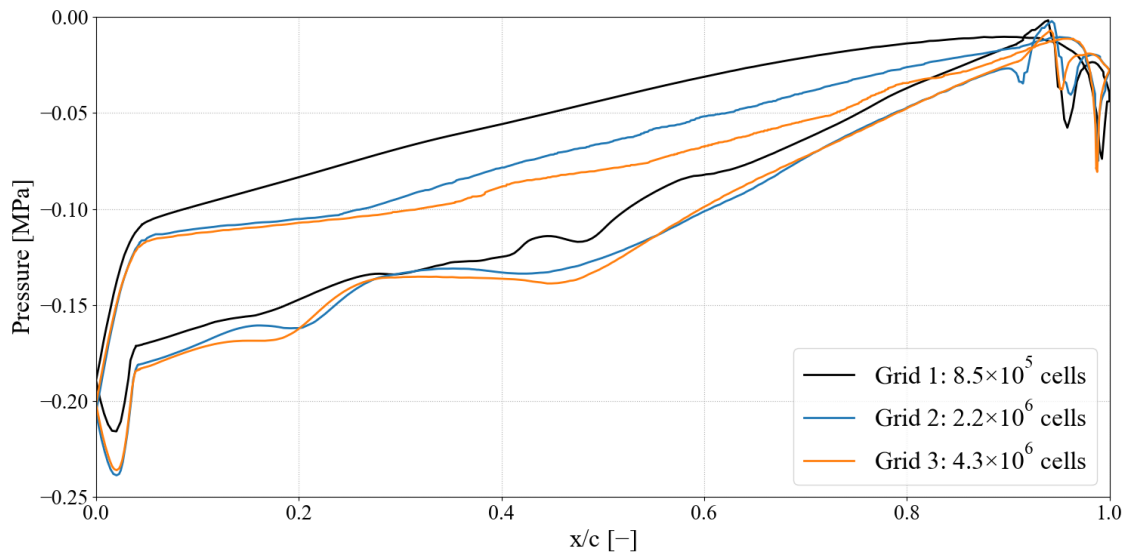


Figure 5.26: Comparison of the pressure distribution along the impeller blade for the different grids

In this figure, the position on the blade is non-dimensionalized using the chord length of the blade. Therefore, the Leading Edge can be found at $x/c = 0$, whereas the Trailing edge is located around $x/c = 1$. It can be seen that the difference between the results become smaller with an increasing number of cells. However,

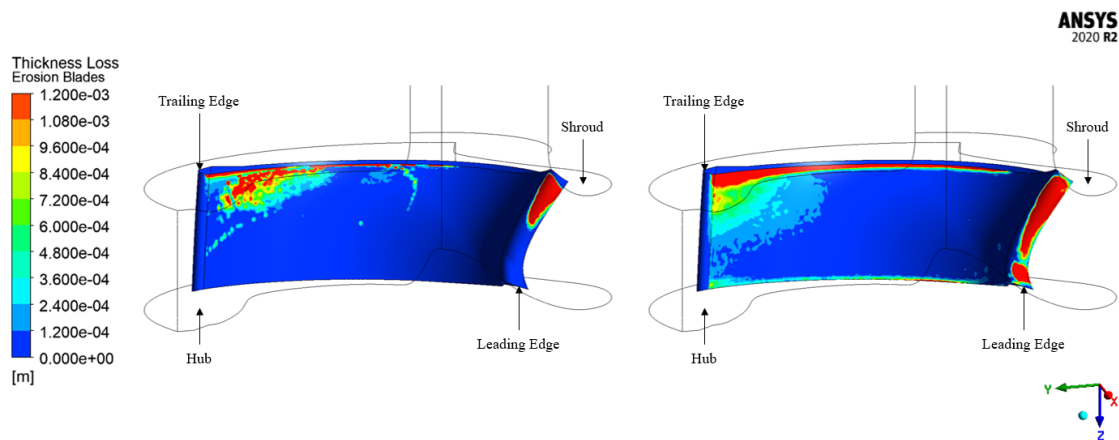
the difference between grids 2 and 3 is still relatively large, which is also visible in figure 5.26.

From the discussion in this paragraph, it can be concluded that grid 3 is the best option to do the erosion calculations on. However, it turned out that on the two finest grids, the particle tracking computations using the two-way coupled method could not be converged. Therefore, in the following paragraphs, the coarsest grid is used.

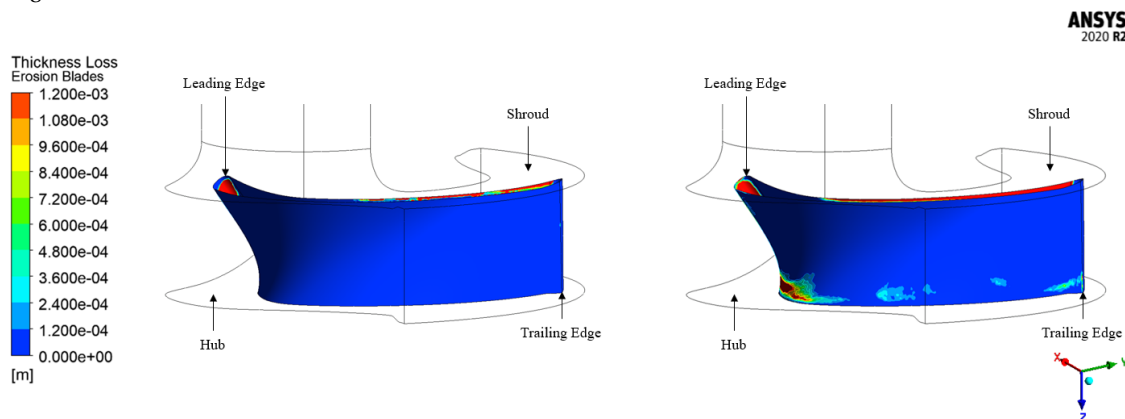
Influence of coupling method

This paragraph shows the differences in erosion on the impeller blades for the one-way coupled and two-way coupled methods. Unfortunately, it was not possible to include the four-way coupled result in this discussion since it was not possible to get a converged solution for this computation.

In figure 5.27, the resulting erosion patterns on the blade are compared for the two different coupling methods. As mentioned before, the numerical results are computed in terms of the erosion rate density (measured in $[kg/m^2s]$). According to Graham et al. [2010], this quantity can be converted into the thickness loss by division by the density and multiplication with the total experimental duration. Therefore, the contours that are shown in figure 5.27 represent the thickness loss that occurred during the experiment.



(a) Erosion pattern on the Suction Side of the blade for the one-way coupled (left) and the two-way coupled method (right)



(b) Erosion pattern on the Pressure Side of the blade for the one-way coupled (left) and the two-way coupled method (right)

Figure 5.27: Comparison between the one-way coupled and two-way coupled erosion patterns on the Suction Side (a) and the Pressure Side (b) of the blade

The largest difference between the two methods is that the one-way coupled method only predicts erosion at the part of the blade near the shroud, whereas the two-way coupled method calculates erosion over the entire height (in z-direction) of the blade. This difference is due to a large recirculation zone that is present at the Pressure Side near the hub and the Leading Edge of the blade for the one-way coupled results (see figure

5.28). This recirculation zone slows the particles down that approach the blade and pushes those particles around the blade while they do not make contact with the blade itself. In addition, due to the low velocity of those particles, the gravitational acceleration pulls them towards the shroud of the impeller. This results in the erosion distribution that can be seen at the Leading Edge in the left part of figure 5.27a. On the other hand, for the two-way coupled method, the influence of the particles on the fluid flow is taken into account. Due to the inertia of the particles, the velocity of the water increases. Therefore, when taking the influence of the particles on the water into account, the recirculation zone hardly exists and the particles are not slowed down as much as in the one-way coupled situation.

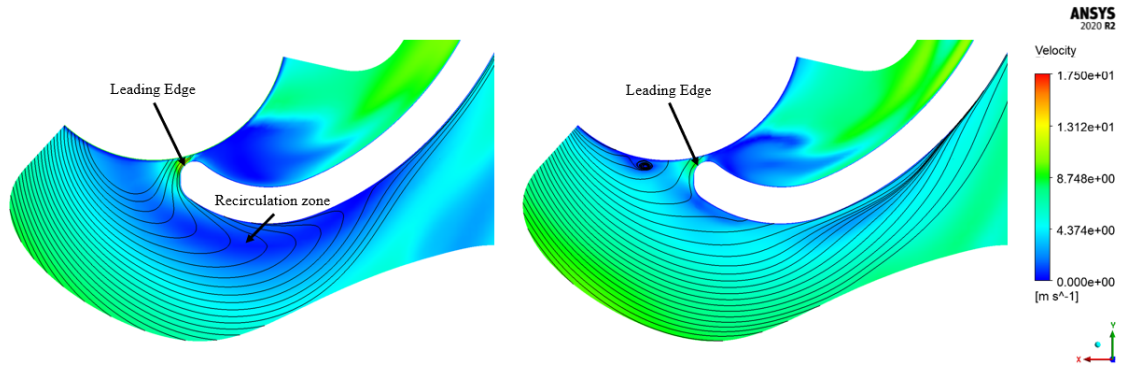


Figure 5.28: Recirculation zone at the Pressure Side near the hub and the Leading Edge of the blade for the one-way coupled (left) and two-way coupled solvers (right). In these figures, the contours of the velocity magnitude are shown in combination with the streamlines of the flow.

Besides the aforementioned large difference, it can be seen that the major erosion zones at the Leading Edge of the blade, near the shroud along the blade and near the Trailing Edge are predicted by both of the methods. For that latter zone, the erosion predicted by the one-way coupled solver is rather localized, whereas the erosion for the two-way coupled method is more spread out.

Influence of erosion model

In the previous section, a comparison between different erosion models is performed for the impinging jet benchmark. In this paragraph, the same analysis is done for the impeller. Here, the Oka erosion model is compared to the Finnie model and the E/CRC model (details about these models can be found in sources such as Zhang et al. [2007] and Finnie [1960]). To this end, the erosion along a certain section of the blade is shown in figure 5.29. In addition, the experimental results are shown in this figure. Therefore, only the part of the blade where the erosion was measured is included.

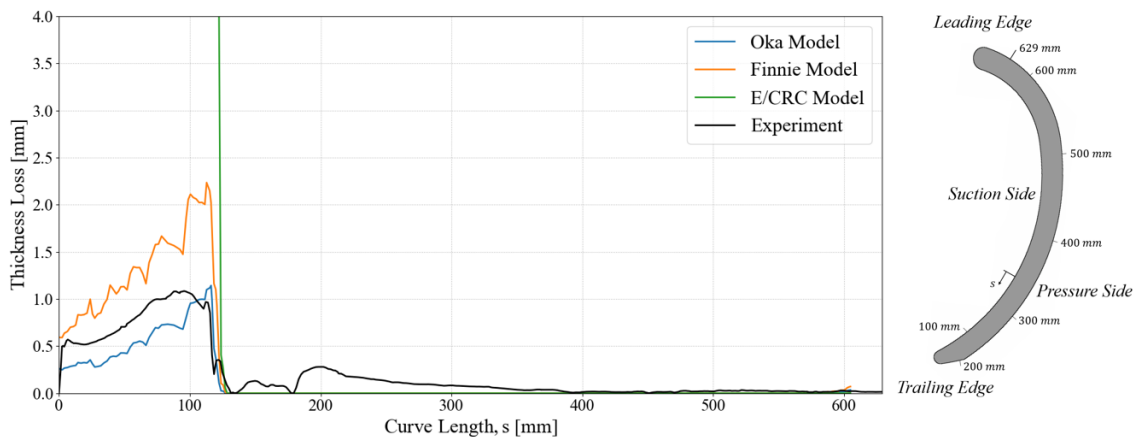


Figure 5.29: Erosion profile along the blade for different erosion models (including the results of the experiment). On the right-hand side of the figure, the definition of the curve length s is shown.

It can be seen that the erosion values predicted by the E/CRC model are much larger than those for the experiment as well as for the other erosion models. This large overprediction may be due to the fact that the model was designed for high particle velocities in combination with rather small particle diameters (Zhang et al. [2017]). In addition, the material that was used during the experiments was Inconel 718. Therefore, it may be that the applicability of the model is restricted to situations that are more similar to the design conditions than the conditions used in the current project.

The differences between the Oka and Finnie erosion models are much smaller. While there is a slight underprediction in figure 5.29 of the erosion rate at the Suction Side of the blade by the Oka model, the Finnie model predicts a higher erosion rate than the experimental value at the same location. The reason for this is that the Finnie model predicts the maximum erosion for a lower impingement angle than the Oka model. This is visualized in figure 5.30.

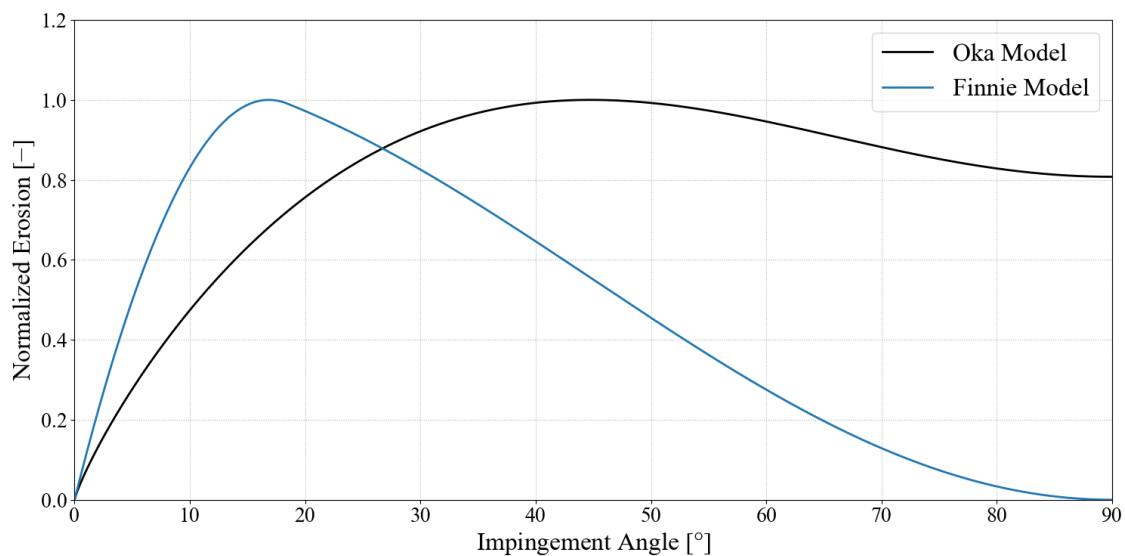


Figure 5.30: Normalized erosion as function of the impingement angle

The erosion that occurs in the region that is shown in figure 5.29 is mostly due to sliding wear (Krüger et al. [2010]). Therefore, the differences in results for the Finnie and the Oka erosion models are due to the different angle dependency of the two models. In the specific profile that is shown in figure 5.29, the Oka model is closer to the experimental results. However, in other regions, the Finnie model corresponds better to the experiment. Therefore, for the validated region, the models perform equally well. However, at regions where the impact wear is dominant (for instance at and near the Leading Edge of the blade) it is expected that the prediction of the Oka model is much closer to reality than that from the Finnie model. This is due to the fact that the Finnie model yields an underprediction of the erosion rate for impact angles larger than 45° (Finnie [1960]). Moreover, 5.30 shows that at 90° impact angle, the Finnie model predicts no erosion at all. Therefore, it can be concluded that the Oka model is more suitable for computing the erosion in a centrifugal dredge pump impeller than the Finnie model.

An explanation for the differences between the results computed by the Oka model and the experiment is given in the next section.

5.3. Validation impeller model

This section consists of a detailed and extensive comparison between the results from the numerical model and the experiment. For the former, the two-way coupled result on the coarsest grid (see table 5.4) is used. The Suction Side and Trailing Edge of the blade are shown in figure 5.31.

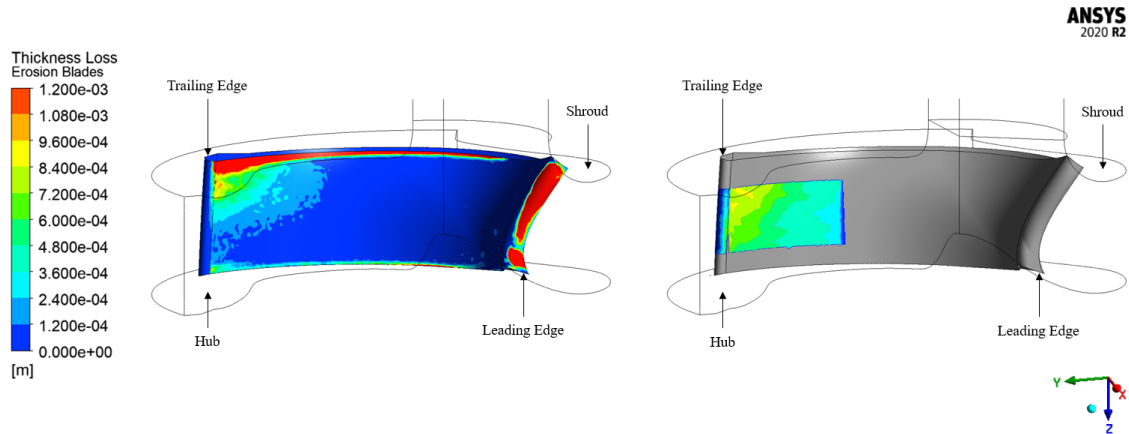


Figure 5.31: Erosion pattern on the Suction Side and the Trailing Edge of the blade for the two-way coupled numerical model (left) and the experiment (right)

When comparing the erosion values at the Suction Side of the blade, it can be seen that, qualitatively the erosion profiles correspond well. The magnitude of the erosion increases when moving towards the Trailing Edge of the blade. In addition, the erosion increases in the direction of the shroud. Quantitatively however, there is an underprediction of the erosion values at the Suction Side of the blade by the numerical model. One explanation for this would be that a constant particle diameter was used in the numerical model, while the PSD showed a large spread of particle diameters as used during the experiment (see figure 4.4). Due to the fact that the gravitational acceleration acts in the positive x-direction, neglecting the smaller particles results in more particles moving towards the shroud. Especially since the densimetric Froude number for this situation is equal to 4.4, which indicates that the effect of the gravity cannot be neglected.

Another explanation would be that the recirculation zone that is causing the erosion at the Suction Side is smaller in reality than that is calculated. Since the recirculation zone is a complex phenomenon to capture, the strength of the vortices within the recirculation zone may be larger in reality than in the calculation. This leads to an underprediction of the impingement velocity and volume fraction at the blade.

Shifting the attention to the Trailing Edge of the blade shows that the erosion at that location is underpredicted. According to the numerical model, there is only erosion at the part of the blade close to the shroud, while the experiment showed erosion over the entire height (in x-direction) that was measured. This discrepancy can be explained by looking at the fact that the flow separates from the blade somewhere at the Trailing Edge. Keeping in mind that the numerical model that is used in this study is not capable of calculating large separating flows (ANSYS, Inc. [2020a]), it cannot be expected that the model captures the flow well at that region.

The third region that was measured during the experiments is the Pressure Side of the blade. The comparison between the numerical and experimental results for this side are shown in figure 5.32.

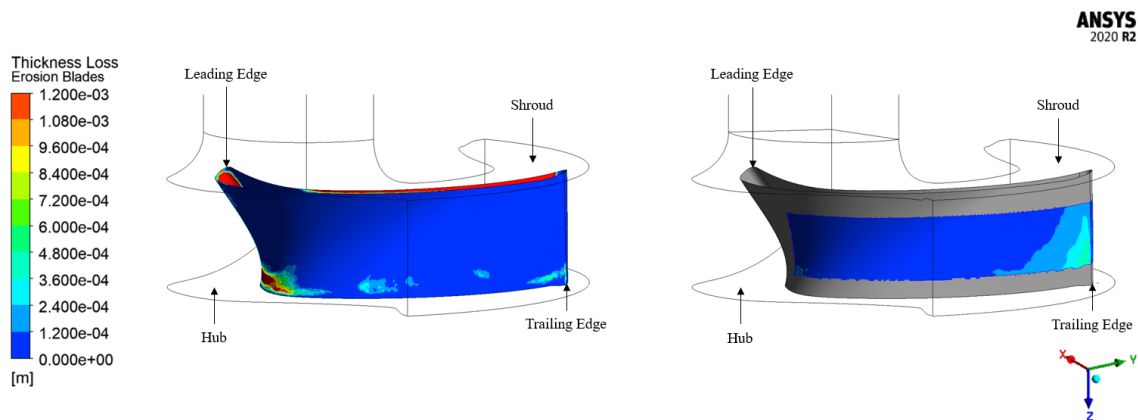


Figure 5.32: Erosion pattern on the Pressure Side of the blade for the two-way coupled numerical model (left) and the experiment (right)

At the Pressure Side, only a small (relative to the erosion occurring at the Suction Side of the blade) amount of erosion was measured. This erosion region is missing in the numerical results. An explanation for this would be that the inter-particle collisions are neglected in the numerical model. As mentioned before, these collisions enhance the turbophoresis effect and with that, the particle flux towards the wall. The fact that the erosion increases while moving towards the Trailing Edge supports this explanation, since the turbophoresis effect would also yield a positive volume fraction gradient (and with that a positive erosion gradient) in the flow direction.

6

Conclusions and Recommendations

The focus of this Master's Thesis is on the subject of erosion estimation for the impeller blades of a centrifugal dredge pump. A numerical model is developed, which is validated using an experiment, that is also carried out as part of the project.

Although several studies have already been conducted on this subject, there are no specific publications available with the exact details of the numerical models that were used. The purpose of this project is to develop such a model. The study is carried out by the author at Damen Dredging Equipment, who have an interest in using the developed model.

In this chapter, the conclusions and recommendations of the project are presented.

6.1. Conclusions

The main goal of this research is to develop, validate and demonstrate a numerical model capable of estimating the erosion wear due to slurry flow on the impeller blades of a centrifugal dredge pump by using Computational Fluid Dynamics (CFD). To reach this goal, three research questions are considered. In this section, an answer is formulated to each of these research questions.

What is the best way to model slurry flow using Computational Fluid Dynamics?

It is found that for the conditions that typically occur in a centrifugal dredge pump impeller, the Eulerian-Lagrangian method is the most appropriate for modeling the slurry flow (Andersson et al. [2012]). This means that the water flow field is treated using the (for CFD standard) Eulerian framework, whereas Newton's second law (the Lagrangian framework) is used to calculate the flow field of the particles. For the former, a RANS model in combination with the $k-\omega$ SST turbulence model is used. Due to the fact that the Eulerian-Lagrangian method breaks down if the particles are larger than the first cell height as measured from a solid wall, the near wall flow is computed using wall functions. For the influence of the particles on the water, source terms are included in the momentum and turbulence equations. The collisions between the particles and the walls are modeled using the Grant-Tabakoff model, whereas the linear soft sphere model is used for the inter-particle collisions.

What is the best way to model erosion wear using Computational Fluid Dynamics?

Erosion wear is influenced by many parameters, including flow parameters, particle parameters and parameters related to the target object. This implies that erosion is a complex phenomenon to model. It is found that the Oka erosion model is the appropriate choice for the current project. This erosion model uses the impact velocity and impact angle of sets of particles to calculate the pattern of erosion on the target surface. In addition, for the actual magnitude of the erosion, the hardness of the material, the particle diameter and the material of the particles are taken into account.

How can the numerical model for erosion wear due to slurry flow on the impeller blades of a centrifugal dredge pump be verified and validated?

The different numerical models that are needed for modeling erosion wear due to slurry flow are used as implemented in ANSYS Fluent. With this complete model, several studies are conducted in order to verify and

validate the model:

- **A submerged impinging jet benchmark study for validating the fluid and particle flow fields.** From this study, it is found that, in general, the prediction of the fluid and particle velocities showed good correspondence with the experimental results (as conducted by Miska [2008]). The largest deviation between the numerical model and the experiments could be found directly in line with the nozzle exit, which is probably due to the inability of the model to calculate the flow field at locations with large streamline curvature.
- **A submerged impinging jet benchmark study for validating the erosion pattern on the target surface.** For this validation study, the results of the experiment by Wang et al. [2021] are used. It is found that there is a considerable dependency of the erosion pattern on the hardness of the target surface material. Therefore, for estimating the erosion wear, it is important to have an accurately determined value for this. In addition, the erosion profile as computed with the four-way coupled method turned out to be influenced to a large extent by the values of the collision model parameters. On the other hand, while neglecting the influence of the inter-particle collisions, it was found that the erosion peak is predicted at the correct location, although the magnitude of the erosion at that location is overpredicted.
- **A verification study for the impeller** starting with an investigation into the grid convergence. Although an optimal mesh (in terms of the balance between the computational costs and the accuracy) is found in this investigation, it turned out that convergence could not be reached for the computation on that optimal mesh where the sand particles are included. Since the available time of this project was limited, the rest of the studies were conducted using a coarser grid. For this grid, the discretization error that is involved in the computation of the head is relatively large (around 16%). In addition, the occurrence and strength of the recirculation zones still show a dependency on the grid. Therefore, it is expected that the use of a finer grid does have a significant influence on the accuracy of the erosion results. During the rest of the verification study, it is found that the two-way coupled method provides significantly more accurate results than the one-way coupled method. A comparison between the different erosion models showed that the E/CRC erosion model yields a large overprediction making it useless for the current application. In addition, the Finnie and Oka erosion models performed equally well for the validated region. However, due to the inability of the Finnie model to predict the erosion at and near the Leading Edge of the impeller blade, it can be concluded that the Oka model is the most suitable model for computing the erosion occurring in the centrifugal dredge pump impeller.
- **A validation of the numerical model for the actual impeller using experimental data that are acquired within the current project itself.** For this experiment, a facility was used that is available and operational within the company Damen Dredging Equipment. Within this facility, a certain dredge pump operated for about 56 hours while using a certain set of conditions. By measuring a number of points before and after the experiment using a Coordinate Measurement Machine, the erosion wear on the impeller blades could be found. By comparing the numerical results (as calculated using the two-way coupled method), it is found that the erosion rate at the Suction Side of the blade is slightly underpredicted, while the results show good agreement in qualitative manner. For the Pressure Side of the blade, there are larger differences, although the major part of this side does not show any erosion at all for both the numerical and the experimental results.

6.2. Recommendations

The results that are discussed in this Master's Thesis show the potential of using numerical models for estimating the erosion wear in centrifugal dredge pump impellers. It is found that for the validated region, the location of maximum erosion wear as well as the order of magnitude for the erosion wear could be predicted with reasonable accuracy. Therefore, the currently available model can be used during for instance the early design stage of a centrifugal dredge pump. This could be for the following purposes:

- Optimisation of a blade design such that the blade experiences the least erosion (as computed with the numerical model).
- Adjustment of the blade design based on the maximum erosion zones that are found in the current study. In that way, the blade can be reinforced locally in order to extend its lifetime.

- Estimation of the lifetime of the impeller blade based on the results that are presented in the current study.

On the other hand, there are still a number of discrepancies between the numerical and experimental results, as well as limitations in its applicability. Therefore, it is recommended to investigate or improve the following aspects of the numerical method:

- The erosion results for the impeller that are obtained are based on a relatively coarse grid where still a large discretization error is present. Therefore, it is recommended to investigate the effect of the discretization on the erosion results. For this, first the convergence issues have to be resolved which occurred during the current project. A possible solution for these issues would be to lower the solid particle volume fraction.
- The effect of including the inter-particle collisions should be further investigated. In addition, it is found that the four-way coupled results show a large dependency on the values of the collision model parameters. Therefore, in order for the collision model to be accurate and meaningful, experimental data on these parameters should be obtained (either from literature or by performing an experiment).
- In practice, the erosion rate on a certain location in the impeller is not constant over time. Due to the varying geometry of the impeller, the flow pattern and with that the erosion pattern changes. Therefore, when estimating the long-term effects of operating the dredge pump, the variation in time of the impeller geometry should be taken into account in the numerical model.
- The numerical model is validated against the experimental data that is obtained during this project. The value of the validation could be improved by including additional measurement points at the Leading Edge, the Suction Side and the parts of the blade near the hub and shroud. The additional experiment can be built on the knowledge that is acquired in the current project, for instance in terms of the duration of the experiment and the method to measure and post-process the erosion.
- Operating the pump at different flow rates results in very different flow patterns. For example by reducing the flow rate below the Best Efficiency conditions, more severe recirculation zones are expected to occur. It is known that the RANS CFD model (especially in combination with the use of wall functions), is not very capable of computing the flow field when there is a lot of flow separation. Therefore, the results of this study cannot be extended to other conditions than those used in this study. Ideally, an additional validation should be performed for a case where a lot of recirculation is expected.
- In the current project, only a steady-state, symmetric analysis of the isolated impeller was performed with a single diameter for the sand particles. In addition, the geometry of the pipes that were upstream of the pump during the experiment is not modeled. Although the results of this analysis showed good agreement with the experiments, an increased accuracy can be expected when the neglected aspects are included in the computation.

Bibliography

- Ahmad, K., Baker, R. C., and Goulas, A. (1986). Computation and Experimental Results of Wear in a Slurry Pump Impeller. In *Proceedings of the Institution of Mechanical Engineers*, volume 200, pages 439–445.
- Andersson, B., Andersson, R., Håkansson, L., Mortensen, M., Sudiyo, R., and van Wachem, B. (2012). *Computational Fluid Dynamics for Engineers*. Cambridge University Press, Cambridge.
- ANSYS, Inc. (2020a). ANSYS Fluent Theory Guide.
- ANSYS, Inc. (2020b). ANSYS Fluent User's Guide.
- Ardakani, E. S. (2016). "Numerical and Experimental Study of the Arc Fluctuations in a DC Plasma Torch". PhD thesis, University of Toronto.
- Berthold Technologies (n.d.). *Density Meter - LB444*.
- Bitter, J. G. A. (1962). A Study of Erosion Phenomena. *Wear*, 6:5–21. Part I.
- Brennen, C. E. (2005). *Fundamentals of Multiphase Flows*. Cambridge University Press.
- Capecelatro, J. and Desjardins, O. (2013). Eulerian-Lagrangian Modeling of Turbulent Liquid-Solid Slurries in Horizontal Pipes. *Journal of Multiphase Flow*, 55:64–79.
- Celik, I. B., Ghia, U., Roache, P. J., Freitas, C. J., Coleman, H., and Raad, P. E. (2008). Procedure for Estimation and Reporting of Uncertainty Due to Discretization in CFD Applications. *Journal of Fluids Engineering*, 130(7).
- Crowe, C. T., Schwarzkopf, J. D., Sommerfeld, M., and Tsuji, Y. (2012). *Multiphase Flows with Droplets and Particles*. CRC Press, Boca Raton, second edition.
- Davidson, L. (2018). An Introduction to Turbulence Models. Technical report, Chalmers University of Technology.
- Ferziger, J. H. and Perić, M. (2002). *Computational Methods for Fluid Dynamics*. Springer, third edition.
- Finnie, I. (1960). Erosion of Surface by Solid Particles. *Wear*, 3:87–103.
- Fraser, W. H. (1981). Flow Recirculation in Centrifugal Pumps. In *Proceedings of the Tenth Turbomachinery Symposium*, pages 95–100.
- Gandhi, B. K., Singh, S. N., and Seshadri, V. (2001). Variation of wear along the volute casing of a centrifugal slurry pump. *JSME International Journal*, 44:231–237.
- Geurts, B. J. and Vreman, B. (2006). Dynamic Self-Organization in Particle-Laden Channel Flow. *International Journal of Heat and Fluid Flow*, 27:945–954.
- Graham, L. J. W., Lester, D. R., and Wu, J. (2010). Quantification of Erosion Distributions in Complex Geometries. *Wear*, 268:1066–1071.
- Grant, G. and Tabakoff, W. (1975). Erosion Prediction in Turbomachinery Resulting from Environmental Solid Particles. *Journal of Aircraft*, 12:471–478.
- Gülich, J. F. (2020). *Centrifugal Pumps*. Springer, fourth edition.
- Hafid, S. (2018). Erosion Modeling.
- Hickel, S. (2019). CFD for Aerospace Engineers. Lecture Slides.

- Huang, S., Huang, J., Guo, J., and Mo, Y. (2019). Study on Wear Properties of the Flow Parts in a Centrifugal Pump based on EDEM-Fluent Coupling. *Processes*, 431.
- Huang, S., Su, X., and Qiu, G. (2015). Transient Numerical Simulation for Solid-Liquid Flow in a Centrifugal Pump by DEM-CFD Coupling. *Engineering Applications of Computational Fluid Dynamics*, 9:411–418.
- Hulshoff, S. J. (2019). AE2220-II Computational Modelling. Lecture notes.
- Ilker, P. and Sorgun, M. (2020). Performance of Turbulence Models for Single Phase and Liquid-Solid Slurry Flows in Pressurized Pipe Systems. *Ocean Engineering*, 214.
- Karelin, V. Y., Denisov, A. I., and Wu, Y. L. (2002). Fundamentals of Hydroabrasive Erosion Theory. In Duan, C. and Karelin, V. Y., editors, *Abrasive Erosion and Corrosion of Hydraulic Machinery*, volume 2, chapter 1, pages 1–51. Imperial College Press, London.
- Keyence Corporation (n.d.). Coordinate Measuring Machines.
- Khalid, Y. A. and Sapuan, S. (2007). Wear analysis of centrifugal slurry pump impellers. *Industrial Lubrication and Tribology*, 59:18–28.
- KROHNE (2011). *OPTIFLUX 4000 Handbook - Electromagnetic flow sensor*.
- Krüger, S., Martin, N., and Dupont, P. (2010). Assessment of Wear Erosion in Pump Impellers. In *Proceedings of the Twenty-Sixth International Pump Users Symposium*, pages 51–56.
- Kundu, P. K. and Cohen, I. M. (2008). *Fluid Mechanics*. Elsevier, fourth edition.
- Lai, F., Zhu, X., Xu, X., and Li, G. (2018). Erosion Wear and Performance Simulation of Centrifugal Pump for Solid-Liquid Flow. In *Proceedings of the ASME 2018 Power Conference*.
- Lambert, M., Braun, M., Dimitrova, D., Schuetze, J., and Stenger, D. (2017). *CFD-DEM, Theory, Numerics, Best Practice*. ANSYS, Inc.
- Maio, F. P. D. and Renzo, A. D. (2005). Modelling Particle Contacts in Distinct Element Simulations: Linear and Non-Linear Approach. *Chemical Engineering Research and Design*, 83:1287–1297.
- Markus, C. (2020). *Materiaaleigenschappen*.
- Matoušek, V. (2004). *Dredge Pumps and Slurry Transport*. Delft University of Technology.
- Menter, F. R. (1994). Two-Equation Eddy-Viscosity Turbulence Models for Engineering Applications. *AIAA Journal*, 32(8).
- Miedema, S. A. and Ramsdell, R. C. (2019). *Slurry Transport, Fundamentals, A Historical Overview and the DHELLDVF*. Delft University of Technology, second edition.
- Miska, S. J. (2008). Particle and Fluid Velocity Measurements for Viscous Liquids in a Direct Impingement Flow Resulting in Material Erosion. Master's thesis, University of Tulsa.
- Mitutoyo (2016). Quick Guide to Surface Roughness Measurement - Reference Guide for Laboratory and Workshop.
- Mitutoyo (n.d.). CRYSTA-APEX S.
- Morsi, S. A. and Alexander, A. J. (1972). An Investigation of Particle Trajectories in Two-Phase Flow Systems. *Journal of Fluid Mechanics*, 55:193–208. Part 2.
- M. Woite (2012). Material No.: AISI 316.
- Neopane, H. P. (2010). *Sediment Erosion in Hydro Turbines*. PhD thesis, Norwegian University of Science and Technology.
- Nieuwstadt, F. T. M., Boersma, B. J., and Westerweel, J. (2016). *Turbulence, Introduction to Theory and Applications of Turbulent Flows*. Springer.

- Oka, Y. I., Okamura, K., and Yoshida, T. (2005a). Practical Estimation of Erosion Damage Caused by Solid Particle Impact. *Wear*, 259:95–101. Part 1: Effects of Impact Parameters on a Predictive Equation.
- Oka, Y. I., Okamura, K., and Yoshida, T. (2005b). Practical Estimation of Erosion Damage Caused by Solid Particle Impact. *Wear*, 259:102–109. Part 1: Mechanical Properties of Materials Directly Associated with Erosion Damage.
- Oliemans, R. V. A. (2001). *Applied Multiphase Flows*. Delft University of Technology, Delft.
- Pagalthivarthi, K. V. and Gupta, P. K. (2009). Prediction of Erosion Wear in Multi-Size Particulate Flow through a Rotating Channel. *Fluid Dynamics and Materials Processing*, 5:93–121.
- Peng, W. and Cao, X. (2016). Numerical Simulation of Solid Particle Erosion in Pipe Bends for Liquid-Solid Flow. *Powder Technology*, 294:266–279.
- Pereira, G. C., de Souza, F. J., and de Moro Martins, D. A. (2014). Numerical Prediction of the Erosion due to Particles in Elbows. *Powder Technology*, 261:105–117.
- Rayan, M. A. and Shawky, M. (1989). Evaluation of Wear in a Centrifugal Slurry Pump. In *Proceedings of the Institution of Mechanical Engineers*, volume 203.
- RGPBALLS Srl (n.d.). AISI 316/316L Stainless Steel Balls.
- Roco, M. C. and Addie, G. R. (1987). Erosion Wear in Slurry Pumps and Pipes. *Powder Technology*, 50:35–46.
- Roco, M. C., Addie, G. R., and Visintainer, R. (1985). Study on casing performances in centrifugal slurry pumps. *Particulate Science and Technology*, 3:65–88.
- Sadighian, A. (2016). *Investigating Key Parameters Affecting Slurry Pipeline Erosion*. PhD thesis, University of Alberta.
- Sapkota, S. (2018). Technical and Sustainability Analysis of Sediment Erosion of Impeller Blades of Dredge Pumps. Master's thesis, University of Twente, Enschede.
- Schlatter, P., Brandt, L., Picano, F., and Casciola, C. M. (2012). Wall Accumulation and Spatial Localization in Particle-Laden Wall Flows. *Journal of Fluid Mechanics*, 699:50–78.
- Sellgren, A., Addie, G., Visintainer, R., and Pagalthivarthi, K. (2005). Prediction of slurry pump component wear and cost. In *Annual Texas A&M Dredging Seminar: 19/06/2005-22/06/2005*. Western Dredging Association.
- Stachiowak, G. W. and Batchelor, A. W. (2014). *Engineering Tribology*. Butterworth-Heinemann, Oxford, fourth edition.
- Tarodiya, R. and Gandhi, B. K. (2017). Hydraulic Performance and Erosive Wear of Centrifugal Slurry Pumps - A Review. *Powder Technology*, 305:27–38.
- Tarodiya, R. and Gandhi, B. K. (2019). Experimental Investigation of Centrifugal Slurry Pump Casing Wear Handling Solid-Liquid Mixtures. *Wear*, 434-435.
- VBKO (1998a). *Voortgezette Opleiding Uitvoering Baggerwerken - Baggerpomp en Aandrijving*. Drukkerij Smits, Den Haag.
- VBKO (1998b). *Voortgezette Opleiding Uitvoering Baggerwerken - Vloeistofmechanica*. Drukkerij Smits, Den Haag.
- Versteeg, H. K. and Malalasekera, W. (2007). *An Introduction to Computational Fluid Dynamics, the Finite Volume Method*. Pearson Education, Essex, second edition.
- Visscher, H. (2012). Ontwerp Testopstelling. Inhoudelijk Verslag.
- Vlasblom, W. J. (2004). *Dredge Pumps - Lecture Notes*. Delft University of Technology.

- Vreman, B., Geurts, B. J., Deen, N. G., Kuipers, J. A. M., and Kuerten, J. G. M. (2009). Two- and Four-Way Coupled Euler-Lagrangian Large-Eddy Simulation of Turbulent Particle-Laden Channel Flow. *Flow Turbulence Combust*, 82:47–71.
- Wang, Q., Huang, Q., Sun, X., Zhang, J., Karimi, S., and Shirazi, S. A. (2021). Experimental and Numerical Evaluation of the Effect of Particle Size on Slurry Erosion Prediction. *Journal of Energy Resources Technology*, 143.
- Wang, Y. and Wang, W. J. (2012). Applicability of Eddy Viscosity Turbulence Models in Low Specific Speed Centrifugal Pump. In *26th IAHR Symposium on Hydraulic Machinery and Systems*, volume 15.
- Wilson, K. C., Addie, G. R., Sellgren, A., and Clift, R. (2006). *Slurry Transport using Centrifugal Pumps*. Springer, third edition.
- Xiao, Y., Guo, B., Ahn, S. H., Luo, Y., Wang, Z., Shi, G., and Li, Y. (2019). Slurry Flow and Erosion Prediction in a Centrifugal Pump after Long-Term Operation. *Energies*, 1523.
- Yeoh, G. H. and Tu, J. (2009). *Computational Techniques for Multiphase Flows*. Butterworth-Heinemann, Oxford, first edition.
- Zhang, J., McLaury, B. S., and Shirazi, S. A. (2017). Effect of Near Wall Modeling Approaches on Solid Particle Erosion Prediction. In *Proceedings of the ASME 2017 Fluid Engineering Division Summer Meeting*.
- Zhang, Y., Reuterfors, E. P., McLaury, B. S., Shirazi, S. A., and Rybicki, E. F. (2007). Comparison of Computed and Measured Particle Velocities and Erosion in Water and Air Flows. *Wear*, 263:330–338.
- Zhu, H., Zhu, J., Rutter, R., and Zhang, H. Q. (2019). A Numerical Study on Erosion Model Selection and Effect of Pump Type and Sand Characters in Electrical Submersible Pumps by Sandy Flow. *Journal of Energy Resources Technology*, 141.
- Çengel, Y. A. and Cimbala, J. M. (2006). *Fluid Mechanics, Fundamentals and Applications*. McGraw-Hill.

A

Governing Equations

This appendix consists of a list of the equations that are used in the numerical model, starting with the Reynolds Averaged Navier-Stokes equations:

$$\begin{aligned} \frac{\partial \bar{U}_j}{\partial x_j} &= 0 \quad j = 1, 2, 3 \\ \rho \left[\frac{\partial \bar{U}_i}{\partial t} + \frac{\partial (\bar{U}_i \bar{U}_j)}{\partial x_j} \right] &= -\frac{\partial \bar{p}}{\partial x_i} + \rho \bar{f}_i + \mu \frac{\partial^2 \bar{U}_i}{\partial x_j \partial x_j} - \rho \frac{\partial \overline{U'_i U'_j}}{\partial x_j} \quad i, j = 1, 2, 3 \end{aligned} \quad (\text{A.1})$$

For the modeling of the Reynolds stress term, the k - ω SST turbulence model is used:

$$\begin{aligned} -\rho \overline{U'_i U'_j} &= \mu_t \left(\frac{\partial \bar{U}_i}{\partial x_j} + \frac{\partial \bar{U}_j}{\partial x_i} \right) - \frac{1}{3} \overline{U'_k U'_k} \rho \delta_{ij} \quad i, j, k = 1, 2, 3 \\ \mu_t &= \frac{\rho a_1 k}{\max(a_1 \omega; SF_2)} \\ \frac{D\rho k}{Dt} &= -\rho \overline{U'_i U'_j} \frac{\partial u_i}{\partial x_j} - \beta^* \rho \omega k + \frac{\partial}{\partial x_j} \left(\{ \mu + \sigma_k \mu_t \} \frac{\partial k}{\partial x_j} \right) \quad i, j = 1, 2, 3 \\ \frac{D\rho \omega}{Dt} &= -\frac{\gamma}{\nu_t} \rho \overline{U'_i U'_j} \frac{\partial u_i}{\partial x_j} - \beta \rho \omega^2 + \frac{\partial}{\partial x_j} \left[(\mu + \sigma_\omega \mu_t) \frac{\partial \omega}{\partial x_j} \right] + 2(1 - F_1) \rho \sigma_\omega^2 \frac{1}{\omega} \frac{\partial k}{\partial x_j} \frac{\partial \omega}{\partial x_j} \quad i, j = 1, 2, 3 \quad (\text{A.2}) \\ F_1 &= \tanh \left\{ \min \left[\max \left(\frac{\sqrt{k}}{0.09 \omega y}; \frac{500 \nu}{y^2 \omega} \right); \frac{4 \rho \sigma_\omega^2 k}{CD_{k\omega} y^2} \right] \right\} \\ F_2 &= \tanh \left[\max \left(2 \frac{\sqrt{k}}{0.09 \omega y}; \frac{500 \nu}{y^2 \omega} \right) \right] \\ CD_{k\omega} &= \max \left(2 \rho \sigma_\omega^2 \frac{1}{\omega} \frac{\partial k}{\partial x_j} \frac{\partial \omega}{\partial x_j}; 10^{-20} \right) \quad j = 1, 2, 3 \end{aligned}$$

The paths of the particles are computed by using Newton's second law:

$$\begin{aligned} m_p \frac{dU_{i,p}}{dt} &= F_{i,Drag} + F_{i,Buoy} + F_{i,Virt} + F_{i,Press} + F_{i,Rot} \quad i = 1, 2, 3 \\ &= \frac{1}{2} \rho A_p \left(K_0 + \frac{K_1}{Re_p} + \frac{K_2}{Re_p^2} \right) \|\vec{U} - \vec{U}_p\| (U_i - U_{i,p}) + V_p g_i (\rho_p - \rho) - C_{VM} \rho V_p \left(\frac{DU_i}{Dt} - \frac{dU_{i,p}}{dt} \right) + \\ &V_p \left(-\frac{\partial p}{\partial x_i} + \frac{\partial \tau_{ij}}{\partial x_j} \right) + m_p (-2\Omega_j U_{k,p} \varepsilon_{jki} - \Omega_j r_j \Omega_i + \Omega_j \Omega_j r_i) \quad i, j, k = 1, 2, 3 \end{aligned} \quad (\text{A.3})$$

The collisions of particles with the wall are modeled using the Grant-Tabakoff rebound model:

$$\begin{aligned} e_N &= \frac{U_{N_2}}{U_{N_1}} = 0.993 - 1.76\alpha + 1.56\alpha^2 - 0.49\alpha^3 \\ e_T &= \frac{U_{T_2}}{U_{T_1}} = 0.988 - 1.66\alpha + 2.11\alpha^2 - 0.67\alpha^3 \end{aligned} \quad (\text{A.4})$$

On the other hand, for the inter-particle collisions, the DEM collision model is adopted:

$$\begin{aligned} \vec{F}_{normal} &= K_s \delta \vec{e}_{12} = \frac{\pi \|\vec{U}_{p,2} - \vec{U}_{p,1}\|^2}{3\varepsilon_D^2} D_{parc} \rho_p \delta \vec{e}_{12} \\ F_{friction} &= \mu_{coll}(U_r) \|\vec{F}_{normal}\| \end{aligned} \quad (\text{A.5})$$

Finally, for the erosion, the Oka erosion model is used:

$$\begin{aligned} ER_v &= ER_{v,90} f(\alpha) \\ f(\alpha) &= \sin^{n_1}(\alpha) [1 + Hv(1 - \sin(\alpha))]^{n_2} \\ ER_{v,90} &= K(aHv)^{k_1 b} \left(\frac{U_p}{U^*}\right)^{k_2} \left(\frac{d_p}{d^*}\right)^{k_3} \end{aligned} \quad (\text{A.6})$$

B

Fluent Settings

In this Appendix, the settings that are used for the impeller computations are listed. From the parameters for which the Fluent default value is used, only the relevant ones are included here. Since for a erosion calculation, the first step is to converge the water flow field, these settings are listed first in table B.1. This is followed by the general settings needed for the computation of the particle flow field in table B.2. These settings are necessary for all three coupling methods.

In the tables B.3, B.4 and B.5, the specific settings settings are listed that are needed for the one-way coupled, two-way coupled and four-way coupled methods, respectively.

Tab name	Parameter	Value/setting	Unit
<i>General</i>	Gravitational Acceleration	$\langle 0, 0, -9.81 \rangle$	$[m/s^2]$
<i>Models</i>	Viscous Model	$k-\omega$ SST model	-
<i>Materials</i>	Water Density	998.2	$[kg/m^3]$
	Water Viscosity	0.001003	$[kg/ms]$
<i>Cell zone conditions</i>	Material Name	Water	-
	Frame Motion	Enabled	-
	Rotation Axis	$\langle 0, 0, 1 \rangle$	-
	Rotation Velocity	62.48	$[rad/s]$
<i>Boundary Conditions; Inlet</i>	Type	Velocity Inlet	-
	Velocity	4.301	$[m/s]$
	Turbulence Intensity	2.82	[%]
	Hydraulic Diameter	0.25	$[m]$
<i>Boundary Conditions; Outlet</i>	Type	Pressure outlet	-
	Backflow Direction Specification Method	From Neighboring Cell	-
	Turbulence Intensity	2.82	[%]
	Hydraulic Diameter	0.25	$[m]$
<i>Boundary Conditions; Impeller Walls</i>	Type	Wall	-
	Shear Condition	No Slip	-
	Wall Motion	Rotating Wall	-
	Motion	Relative to Adjacent Cell Zone	-
	Speed	0	$[rad/s]$
<i>Boundary Conditions; Pipe Wall</i>	Type	Wall	-
	Shear Condition	No Slip	-
	Wall Motion	Rotating Wall	-
	Motion	Absolute	-
	Speed	0	$[rad/s]$
<i>Mesh Interfaces</i>	Interface	Periodic matching	-
	Type	Rotational	-
	Rotation Axis	$\langle 0, 0, 1 \rangle$	-

Tab name	Parameter	Value/setting	Unit
	Angle	120	[°]
<i>Reference Values</i>	Compute From	Inlet	-
	Area	0.049	[m ²]
	Length	0.25	[m]
<i>Methods</i>	Gradient	Green-Gauss Node Based	-
	High Order Term Relaxation	Enabled	-
<i>Residual</i>	Absolute Criteria	10 ⁻⁵	-

Table B.1: Settings for solving the water flow field

Tab name	Parameter	Value/setting	Unit
<i>Discrete Phase</i>	Virtual Mass Force	Enabled	-
	Pressure Gradient Force	Enabled	-
	Erosion/Accretion	Enabled	-
	Accuracy Control	Disabled	-
	Enable Node Based Averaging	Enabled	-
	Average DPM Source Terms	Enabled	-
<i>Injections</i>	Injection Type	Surface	-
	Release From Surfaces	Inlet	-
	Inject Using Face Normal Direction	Enabled	-
	Diameter	0.619×10^{-3}	[m]
	Velocity Magnitude	4.301	[m/s]
	Total Flow Rate	18.66	[kg/s]
	Discrete Random Walk Model	Enabled	-
	Random Eddy Lifetime	Enabled	-
<i>Materials</i>	Sand Density	2650	[kg/m ³]
<i>Boundary Conditions; Walls</i>	Normal Discrete Phase Reflection Coefficients (Polynomial)	0.993 -0.0307 0.475×10^{-3} -0.261×10^{-5}	-
	Tangent Discrete Phase Reflection Coefficients (Polynomial)	0.988 -0.0290 0.643×10^{-3} -0.365×10^{-5}	-
	Oka Erosion Model; Reference Erosion Rate	6.777×10^{-4}	-
	Oka Erosion Model; Wall Material Vickers Hardness	3.844	[GPa]
	Oka Erosion Model; Model Constant, n1	0.857	-
	Oka Erosion Model; Model Constant, n2	0.677	-
	Oka Erosion Model; Velocity Exponent	2.421	-
	Oka Erosion Model; Diameter Exponent	0.190	-
	Oka Erosion Model; Reference Diameter	0.326×10^{-3}	[m]
	Oka Erosion Model; Reference Velocity	104	[m/s]

Table B.2: Settings for solving the particle flow field (valid for all coupling methods)

Tab name	Parameter	Value/setting	Unit
<i>Injection</i>	Number of Tries	50	-

Table B.3: Additional settings for solving the one-way coupled particle flow field

Tab name	Parameter	Value/setting	Unit
<i>Discrete Phase</i>	Interaction with Continuous Phase	Enabled	-
	DPM Iteration Interval	20	-
	Mean Values	Enabled	-
	RMS Values	Enabled	-
	Two-Way Turbulence Coupling	Enabled	-
<i>Injection</i>	Number of Tries	50	-
<i>Controls</i>	Discrete Phase Sources (relaxation factor)	0.25	-

Table B.4: Additional settings for solving the two-way coupled particle flow field

Tab name	Parameter	Value/setting	Unit
<i>Discrete Phase</i>	Interaction with Continuous Phase	Enabled	-
	DPM Iteration Interval	2	-
	Mean Values	Enabled	-
	RMS Values	Enabled	-
	Unsteady Particle Tracking	Enabled	-
	Particle Time Step Size	1.0×10^{-5}	[s]
	Number of Time Steps	40	-
	Two-Way Turbulence Coupling	Enabled	-
<i>Injection</i>	DEM Collision	Enabled	-
	DEM Collision Partner	dem-sand	-
	Stop Time	15	[s]
	Parcel Release Method	constant-number	-
<i>DEM Collision Settings</i>	Particle Number in Parcel	100	-
	Tangential (dem-sand - dem-sand)	friction-dshf	-

Table B.5: Additional settings for solving the four-way coupled particle flow field